

Expansion wave diffraction around sharp convex corners

Z. Shaikh

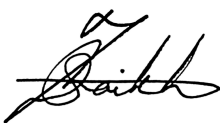
A dissertation submitted to the Faculty of Engineering and the Built Environment, University of the Witwatersrand, Johannesburg, in fulfilment of the requirements for the degree of Master of Science in Engineering.

Johannesburg, December 2017

Declaration

I declare that this dissertation is my own, unaided work, except where otherwise acknowledged. It is being submitted for the degree of Master of Science in Engineering in the University of the Witwatersrand, Johannesburg. It has not been submitted before for any degree or examination at any other university.

Signed this 6th day of December 2017

A handwritten signature in black ink, appearing to read 'Z. Shaikh', written in a cursive style.

Scanned by CamScanner

Z. Shaikh

Acknowledgements

I would like to thank the following people:

Prof. B. W. Skews, for stirring my interest in the fascinating field of compressible fluid dynamics, for proposing this topic and for the invaluable suggestions and guidance through the course this project.

To Mr. R. Paton, for his much valued insights with regards the design and assembly of the experimental facility, his suggestions with the computational work and for his assistance with gaining access to the computing resources demanded by this work.

Many thanks to the laboratory workshop staff in School of Mechanical, Industrial and Aeronautical engineering for manufacture of the experimental rig components and for the assistance and suggestions on the assembly.

To my colleagues at the Flow Research Unit for any assistance and support to this work. I would also like to acknowledge the undergraduate students who assisted with the setup and running of the experiments.

Finally, I would like to thank my parents and family for their unwavering support.

Abstract

Much work has been previously invested towards the study of shock wave phenomena. However, little or no literature can be found involving studies of expansion waves undergoing similar effects. The study of expansion wave diffraction was first considered by Mohamed and Skews [1]. The investigation focussed on studying expansion wave diffraction around a 90° corner by using both experimental and computational methods. While a good agreement between the results was found there were several features which were apparent in the experimental imaging but could not be resolved by a numerical model. This included the large-scale turbulent structures in the separation bubble, shear layer instability and vortex shedding as well as a large wake region which was noted downstream of the bubble.

In the current work, expansion wave diffraction is examined using Large Eddy Simulation in an attempt to provide a better description of the flow field. To make the analysis more feasible the Embedded LES hybrid technique was employed. Several subgrid-scale LES models were tested and the Wall Modelled LES technique showed the most promising results. The LES solution showed much improvement to the RANS solutions from the previous work. Turbulence in the separation bubble was evident and shear-layer instability and vortex shedding was observed. Due to the very low velocity fluctuations the LES model did not resolve the wake region although, in certain cases, evidence of a wake region beginning to form could be seen. Using these results a further analysis into the structure of the bubble through the depth of the flow was conducted.

As an extension of previous work the current study also examined expansion wave diffraction around other convex corners. The study involved an experimental as well as RANS and LES computational methods. The wedge angles investigated were 45° , 15° and 5° . The effects of changing the initial diaphragm pressure ratio and the diaphragm distance from the diffraction corner were analysed. The results showed a high resemblance to what was found previously for the 90° case. However, significant differences were noted in the shape of the bubble due to the inclination angle of the flow along vertical wall and the much higher velocity gradients of the flow at the diffraction corner and surrounding the bubble.

Published Work

Shaikh Z, Skews B. W. (2017). *Large Eddy Simulation of Expansion Wave Diffraction*, 31st Intertional Symposium on Shock Waves Conference, Nagoya, Japan, July 17th-20th, (Proceedings in Press).

Contents

Declaration	i
Acknowledgements	ii
Abstract	iii
Published Work	iv
Contents	v
List of Figures	ix
List of Tables	xv
1 Introduction	1
1.1 Background	1
1.2 Previous Work	2
1.3 Chapter Overviews	7
1.4 Shock Tube Theory	8
1.5 Finite Expansion Waves	10
1.5.1 Basic One Dimensional Expansion Wave Dynamics	11

1.5.2	Supersonic flow	13
1.5.3	Expansion Wave Propagation Speed	14
1.6	Turbulence	15
1.6.1	CFD and turbulence modelling	15
1.6.2	Compressible Turbulence Dynamics	16
1.7	Large-Eddy Simulation	17
1.7.1	Hybrid LES-RANS models	19
1.7.2	Subgrid-Scale Models	19
I	Analysis of expansion wave diffraction around sharp convex wedges	23
2	Experimental Method	24
2.1	Experimental facilities	24
2.2	Optical Visualisation	27
3	Computational Method	28
3.1	The Computational Domains	28
3.2	Grid Development	30
3.3	Solver Setup	31
3.4	CFD Validation	32
4	Expansion wave diffraction around sharp convex corners	34
4.1	Introduction	34
4.2	Comparison of major flow features	35
4.2.1	Reflected compression wave	35

4.3	The separation bubble and near corner flow structure	37
4.3.1	The separation bubble growth	37
4.3.2	Near corner velocity gradients and viscous vortices	43
4.3.3	Oblique shock and supersonic region	48
4.3.3.1	Evolution of the supersonic region	48
4.3.3.2	Behaviour of the Oblique shock	49
4.3.4	Recompression shock	50
4.4	Trailing sonic and supersonic flow	56
4.4.1	Comparison between flow features for $P41 < 10.4$ and $P41 > 10.4$. .	56
4.4.1.1	The Oblique Shock	56
4.4.1.2	The Supersonic Region	58
4.4.1.3	The Reflected Compression Wave	58
II	Large Eddy Simulation of expansion wave diffraction	62
5	LES Computational Method	63
5.1	The Computational Model	63
5.2	Mesh Development	64
5.3	Subgrid Scale Modelling	67
6	Discussion	70
6.1	The separation bubble	70
6.2	Viscous vortices	75
6.3	The Oblique Shock and Supersonic Region	80

6.4	LES Results for $\theta = 15^\circ$, $P41 = 3$	82
7	Conclusions	85
8	Recommendations	87
A	Engineering Drawings	89
B	Additional ELES Results for 15° , $d = 10$ mm	104
C	Digital Appendix	109
C.1	109
C.2	109

List of Figures

1.1	Post-diaphragm burst shock tube events	2
1.2	Previous experimental rig for 90° analysis	3
1.3	Shadowgraph images indicating the main flow features following expansion wave diffraction	4
1.4	Expansion wave diffraction	5
1.5	Qualitative comparison between Menter’s SST $\kappa - \omega$ turbulence model and high-speed shadowgraph images	6
1.6	Initial shocktube conditions	9
1.7	Shock tube conditions after diaphragm burst	9
1.8	Post diaphragm burst shock tube events - Vector notation	10
1.9	Shock tube wave diagram	10
1.10	Finite Expansion Wave Diagram	11
1.11	Expansion Wave Behaviour [4]	12
1.12	Variation of expansion wave width with P41	15
1.13	Comparison between resolved scales of motion for RANS, LES and DNS	18
1.14	Embedded LES Domain	20
2.1	Schematic of the experimental set up	24

2.2	CAD image of the experimental rig	25
2.3	Test Pieces	26
2.4	Optical Visualisation Setup	27
3.1	Schematic of the Experimental Computational Domain	29
3.2	Schematic of the Extended Computational Domain	29
3.3	Grid topology for 45° corner	30
3.4	Poor grid structure at 15° corner	31
3.5	Grid topology for 15° corner	31
3.6	Comparison between density contour plots and schlieren imaging $P41 = 4$, $d = 35$ mm, $t = 411 \mu s$. (a), (b) 15° (c), (d) 45°	33
3.7	Comparison between density contour plots and schlieren imaging $P41 = 4$, $d = 55$ mm, $t = 612 \mu s$. (a), (b) 15° (c), (d) 45°	33
4.1	Pressure contour plot for $\theta = 45^\circ$, $PR = 6$ and $d = 40$ mm at a time delay of $t = 250 \mu s$	35
4.2	Pressure contours for $\theta = 45^\circ$ and $\theta = 15^\circ$ at $PR = 6$ and $D = 10$ mm (a,b) = $50 \mu s$ (c,d) = $200 \mu s$ (e,f) = $350 \mu s$	36
4.3	Pressure contours for $\theta=15^\circ$ at $PR = 6$ and $D = 70$ mm (a) = $150 \mu s$ (b) = $200 \mu s$ (c) = $350 \mu s$	37
4.4	Variation of the stagnation point distance from the corner x_{stag} with non dimensional time for $d = 10$ at $P41 = 3, 6$ and 9	38
4.5	Variation of the stagnation point distance from the corner x_{stag} with non dimensional time for $d = 40$ at $P41 = 3, 6$ and 9	38
4.6	Variation of the stagnation point distance from the corner x_{stag} with non dimensional time at $\theta = 5^\circ, 15^\circ$ and 45°	39
4.7	Density contour plots for $\theta=15^\circ$ and $P41 = 3$ at $t = 200\mu s$	39

4.8	Density contour plots for $\theta=15^\circ$ and $P41 = 9$ at $t = 200\mu s$	40
4.9	Density contour plots for $d = 10$ mm and $P41 = 3$ at $t = 200\mu s$	41
4.10	Density contour plots for $d = 10$ mm and $P41 = 9$ at $t=200\mu s$	41
4.11	Density contour plots for $d = 70$ mm and $P41 = 3$ at $t=200\mu s$	42
4.12	Density contour plots for $d = 70$ mm and $P41=9$ at $t=200\mu s$	42
4.13	Vector velocity plot indicating primary and secondary vortices	43
4.14	Schlieren (horizontal knife-edge) and velocity magnitude vector plot comparison. $\theta = 45^\circ$, $d = 55$ mm. (a, b) $405 \mu s$, (a, b) $740 \mu s$	44
4.15	Velocity magnitude vector plots. $P41 = 3$, $d = 40$ mm and $t=200 \mu s$	45
4.16	Velocity magnitude vector plots. $\theta = 5^\circ$, $P41 = 3$, $d = 40$ mm and $t = 600 \mu s$. Images illustrating the near-corner region are provided in figures (c) and (d) .	45
4.17	Velocity magnitude vector plots at $\theta = 15^\circ$, $P41 = 3$ and 9 at $d = 10$ mm (a, b) $50 \mu s$ (c, d) $600 \mu s$ (a, b and c, d not to the same scale)	46
4.18	Velocity magnitude vector plots. $P41 = 6$, $d = 70$ mm and $t = 300 \mu s$ (a) = 45° (b) = 15° (c) = 5°	46
4.19	Velocity magnitude vector plots for $P41 = 6$ and $d = 70$ mm (a, b) $\theta = 45^\circ$ (c, d) $\theta = 15^\circ$ (e, f) $\theta = 5^\circ$	47
4.20	Mach number contour plots for $\theta = 5^\circ$ and $P41 = 3$ at (a, b) $t = 200 \mu s$ (c, d) $t = 350 \mu s$	49
4.21	Mach number contour plots for $\theta = 5^\circ$ and $P41 = 3$ at (a, b) $t = 450 \mu s$ (c, d) $t = 600 \mu s$	50
4.22	Mach number contour plots for $\theta = 45^\circ$ and $P41 = 3$ at (a, b) $t = 200 \mu s$ (c, d) $t = 350 \mu s$	51
4.23	Mach number contour plots for $\theta = 15^\circ$ and $P41 = 6$ at $t = 600 \mu s$	52
4.24	Mach number contour plots for $\theta = 15^\circ$ and $P41 = 9$ at $t = 600 \mu s$	52
4.25	Mach number contour plots for $\theta = 45^\circ$ and $P41 = 9$ at $t = 600 \mu s$	53

4.26	Density contour plot illustrating the compression shock, boundary layer separation and secondary shear layer. $\theta = 5^\circ$, $P41 = 3$, $d = 40$ mm and $t = 600$ μs	53
4.27	Mach number contour plots. $P41 = 3$, $d = 40$ mm $t = 600$ μs (a) $\theta = 45^\circ$ (b) $\theta = 5^\circ$	54
4.28	Mach number contour plots. $\theta = 5^\circ$, $P41 = 3$ and $t = 600$ μs (a) $d = 10$ mm (b) $d = 40$ mm	54
4.29	Mach number contour plots. $\theta = 5^\circ$, $P41 = 6$ and $t = 600$ μs (a) $d = 10$ mm (b) $d = 40$ mm	55
4.30	Mach number contour on the post diffraction field for $P41 > 10.4$ at $d = 10$ mm, $P41 = 15$ and $t = 400$ μs . Mach 1 trace in red.	57
4.31	Mach number contour plot illustrating the separation bubble for subsonic and supersonic trailing flow at $d = 10$ mm and $t = 450$ μs (a) $P41 = 9$ (b) $P41 = 15$	57
4.32	Mach number contour plot illustrating the separation bubble for subsonic and supersonic trailing flow with variation in d for $\theta = 15^\circ$ at $t = 350$ μs	58
4.33	Mach number contour plot illustrating the separation bubble for subsonic and supersonic trailing flow with variation in d for $\theta = 15^\circ$ at $t = 600$ μs	59
4.34	Mach number contour plot illustrating the separation bubble for subsonic and supersonic trailing flow with variation in θ for $d = 10$ mm at $t = 300$ μs	60
4.35	Mach number contour plot illustrating the separation bubble for subsonic and supersonic trailing flow with variation in θ for $d = 10$ mm at $t = 300$ μs	61
5.1	ELES Computational Domain	63
5.2	Mesh blocking in the LES region	64
5.3	Illustration of Mesh 3 sizing	65
5.4	Illustration of Mesh 2 sizing	66
5.5	Illustration of Mesh 3 sizing	67
5.6	Near corner flow structure using the WALE SGS model	68

5.7	Near corner flow structure using the WMLES SGS model	69
5.8	Near corner flow structure using the WMLES-SO SGS model	69
6.1	Comparison between shadowgraph imagery and LES density contour plots. (a), (b) P41 = 3.2 (c), (d) P41 = 7.7. $t = 400 \mu s$	71
6.2	Density contour plots at P41 = 3.2 and P41 = 7.7 at $z = 10$ mm (a,b) = 200 μs (c,d) = 400 μs (e,f) = 600 μs	72
6.3	Density contour plots at PR = 3.2 and PR = 7.7 at $z = 5$ mm (a,b) = 200 μs (c,d) = 400 μs (e,f) = 600 μs	73
6.4	Density contour plots at P41 = 3.2 and P41 = 7.7 at $z = 15$ mm (a,b) = 200 μs (c,d) = 400 μs (e,f) = 600 μs	74
6.5	Velocity magnitude vector plots of the separation bubble and near corner re- gion. (a, b) P41 = 3.2 (c, d) P41 = 7.7. $t = 200 \mu s$	75
6.6	Velocity magnitude vector plots at PR = 3.2 and PR = 7.7 at $z = 10$ mm (a, b) = 200 μs (c, d) = 400 μs (e, f) = 600 μs	76
6.7	Velocity magnitude vector plots at PR = 3.2 and PR = 7.7 at $z = 10$ mm (a, b) = 200 μs (c, d) = 400 μs (e, f) = 600 μs	77
6.8	Velocity magnitude vector plots at PR = 3.2 and PR = 7.7 at $z = 15$ mm (a,b) = 200 μs (c,d) = 400 μs (e,f) = 600 μs	78
6.9	Vortex Core Steamtrace P41=3.2, $t = 600 \mu s$	79
6.10	Vortex Core Steamtrace P41=7.7, $t = 600 \mu s$	79
6.11	Mean velocity distribution through the separation bubble (a) RANS (b) LES	80
6.12	Mach number contour plot with sonic line trace (red). P41 = 7.7, $t = 400 \mu s$	81
6.13	Mach number contour plot with sonic line trace (red). P41 = 7.7, $t = 600 \mu s$	81
6.14	Comparison between schlieren image, RANS and LES results $\theta = 15^\circ$, P41 = 3	82
6.15	Horizontal knife-edge schlieren images emphasizing the shear layer and later shear layer instability	82

6.16 LES Density contour plots for $\theta = 15^\circ$, $P41 = 3$. (a, b) = 200 μs , (c, d) = 400 μs , (e, f) 600 μs	83
6.17 LES Velocity vector plots for $\theta = 15^\circ$, $P41 = 3$	84
A.1 Driver Back Plate	90
A.2 Driver Bottom Plate	91
A.3 Driver Top Plate	92
A.4 Driver Side Plate (Right). Identical dimensions for left side	93
A.5 Driver Window Frame	94
A.6 Driver Window	95
A.7 Driver Section Assembly	96
A.8 Driver Section Exploded Assembly	97
A.9 Driven Back Plate	98
A.10 Shock Tube Assembly	99
A.11 Test Piece: 15° , $d = 35$ mm	100
A.12 Test Piece: 15° , $d = 55$ mm	101
A.13 Test Piece: 45° , $d = 35$ mm	102
A.14 Test Piece: 45° , $d = 55$ mm	103
B.1 LES Density contour plots for $\theta = 15^\circ$, $P41 = 3$ at $z = 5$ mm	105
B.2 LES Density contour plots for $\theta = 15^\circ$, $P41 = 3$ at $z = 15$	106
B.3 LES Velocity vector plots for $\theta = 15^\circ$, $P41 = 3$ at $z = 5$	107
B.4 LES Velocity vector plots for $\theta = 15^\circ$, $P41 = 3$ at $z = 15$	108

List of Tables

1.1	Relationship between trailing edge direction and Mach number (Left running expansion wave)	14
2.1	Driver Pressures with multiple diaphragms	26
3.1	Experimental Domain Completing Dimensions	29
3.2	Extended Domain Completing Dimensions	30
3.3	Experimental Domain Completing Dimensions	32
5.1	Mesh 1 Summary	65
5.2	Mesh 2 Summary	66
5.3	Mesh 3 Summary	66

Chapter 1 Introduction

1.1 Background

Acoustic waves are responsible for the transport of information through a compressible fluid. Waves transmitting through a fluid induce a response from the fluid in the form of a density change. The fluid would experience an increase in density after a compression wave and a decrease for the case of an expansion wave. A shock wave would form when the trailing end of a compression wave approaches the leading edge due to the acceleration imposed by the compression creating an infinite pressure gradient.

While much attention has been directed to the study of shock wave phenomena, literature on expansion waves is highly limited. Numerous studies have been done to analyse the behaviour of a diffracting shock wave. Experimental analysis has been done by Skews [2] to investigate shock wave diffraction around sharp two-dimensional corners. Flow structures following shock wave diffraction have been studied by Mathews and Howard [3].

A linear wave system, such as the one shown in 1.1 can be generated using a shock tube to facilitate experimental investigations. A shock tube comprises of two sections, one pressurised and the other kept at a lower pressure or left open to the atmosphere. The sections are separated by an airtight diaphragm designed to fail under certain conditions. In a shock-tube generated one-dimensional, linear wave system, post diaphragm burst events include a shock wave, which propagates into the driven section, and an expansion wave which travels upstream into the driver section. Analysis on shock wave diffraction can be performed by placing a backward facing step in the driven section of the shock tube. Alternately, to study expansion wave phenomena, the test section is situated in the driver section of the tube.

Research has been done by Skews and Mohamed [1] investigating diffraction of a two-dimensional expansion wave around a 90° corner. The study included both experimental and computational analyses of the diffraction process. Several interesting flow features were observed in the vicinity of the corner. These included a shear layer, a separation bubble

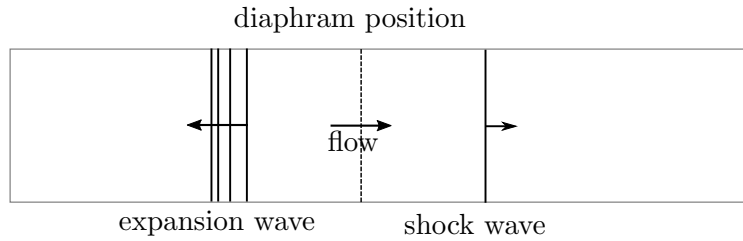


Figure 1.1: Post-diaphragm burst shock tube events

which remained attached to the wall and a reflected compression wave. Experimental results had also indicated the presence of large-scale turbulent structures within the separation bubble and wake region as well as shear layer instability and vortex shedding. Computational analysis using a Reynold’s Averaged Navier Stokes (RANS) solver confirmed the presence of the separation bubble but was unable to resolve any of the turbulent features, wake region and vortex shedding. One of the aims in the current work is to try and model these features by employing the Large Eddy Simulation (LES) CFD solver.

Another aspect of interest which was not explored previously is expansion wave diffraction around sharp convex corners. As a continuation of the work on the 90 degree cases the current study will also explore expansion wave diffraction around sharp wedges.

1.2 Previous Work

The experimental set up used by Skews and Mohamed [2014] for the 90° corner analysis involved a backward facing step in the driver section of a shock tube. An illustration of the experimental rig used is shown in Figure 1.2.

As mentioned in the previous section, the major flow features identified included a shear layer due to separation at the apex, a separation bubble which remained attached to the wall and a reflected compression wave. Additionally, a large wake region had developed downstream of the bubble and, under certain conditions, an oblique shock was noted to the rear of the separation bubble. Experimental results also showed tiny shocklets which emanated from the separation bubble. Shadowgraph and schlieren imaging have indicated large-scale turbulent structures within the separation bubble and shear layer as well as shear layer instability and vortex shedding. A shadowgraph image illustrating the experimental findings is shown in Figure 1.3.

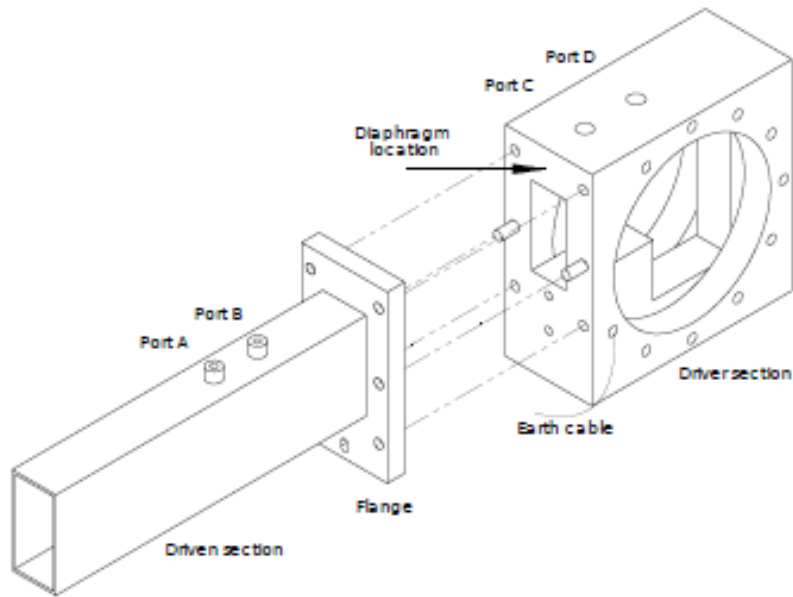


Figure 1.2: Previous experimental rig for 90° analysis

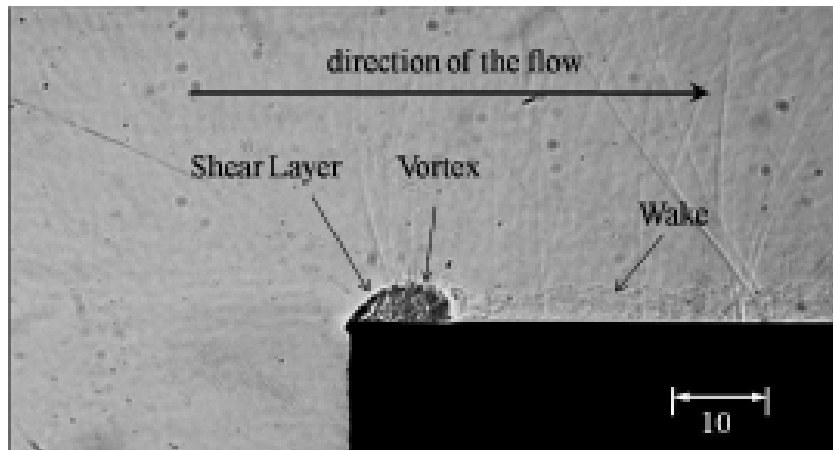
Diffraction around the 90° corner was then analysed using computational methods. A RANS solver with the $\kappa - \omega$ turbulence model was used to model the flow. The contour plot in Figure 1.4 shows the features identified from the simulation results.

Figure 1.5 shows a comparison between the high-speed shadowgraph images and the Menter's SST $\kappa - \omega$ model. The CFD contours show that the aforementioned experimental observations (turbulence within the separation bubble, wake region and vortex shedding) could not be resolved by the 2D RANS CFD solver.

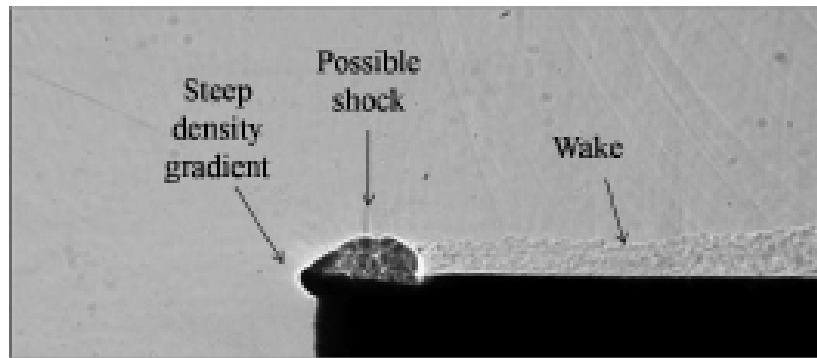
The study analysed the effects of varying two parameters, the distance of the 90° corner from the wall, d , and the initial pressure ratio across the diaphragm, P_{41} , on the major flow features. As the current research is a continuation of this study, it would be valuable to provide a brief summary of the findings. The following results consider $P_{41} < 10.4$, where the flow following the expansion wave is subsonic.

Reflected and Diffracted Waves

The diffraction of each element in the expansion wave was seen to generate a perturbation signal which propagated radially outward into the steady flow behind the expansion wave. The perturbation was identified as a reflected compression wave. The reflected compression waves would propagate outwards and modify the trailing characteristic of the incident expansion wave.



(a)



(b)

Figure 1.3: Shadowgraph images indicating the main flow features following expansion wave diffraction

A significantly broader expansion wave was generated for large values of d and P41. In these cases the reflected compression waves would take longer to propagate into the downstream flow. However, for the cases of d between 0 and 10 mm a rapid coalescence of reflected compression waves would occur and steepen into a cylindrical shock wave.

The Separation Bubble

The separation bubble was contained within a shear layer which formed at the diffraction corner and reattached to the horizontal wall downstream of the bubble. The bubble consisted of a circulatory region which formed the primary viscous vortex. A secondary vortex was identified within the primary bubble near the diffraction corner.

The growth rate of the separation bubble was measured by considering the distance of the stagnation point from the corner. The bubble showed a linear increase in size as the pressure

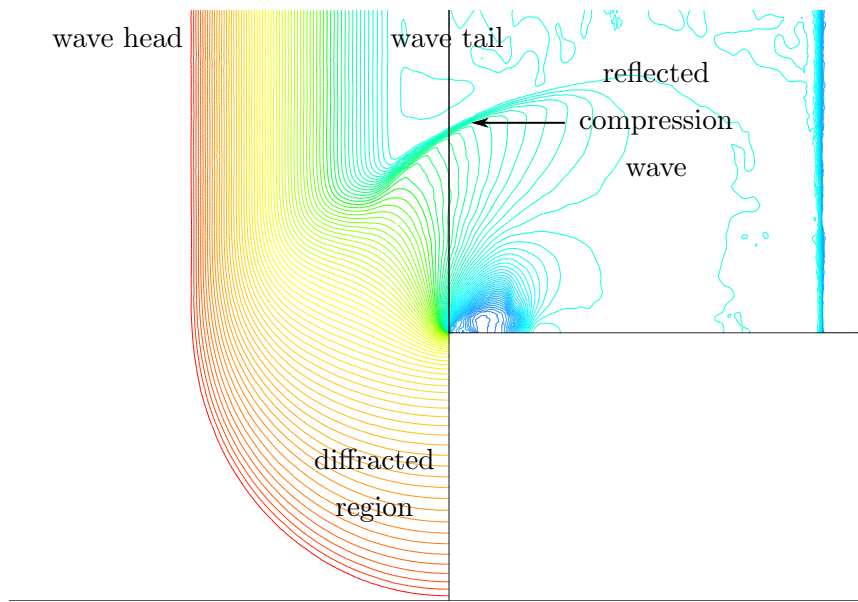


Figure 1.4: Expansion wave diffraction

ratio was increased. It was noted that as d was increased the size of the bubble would become less dependant on P41.

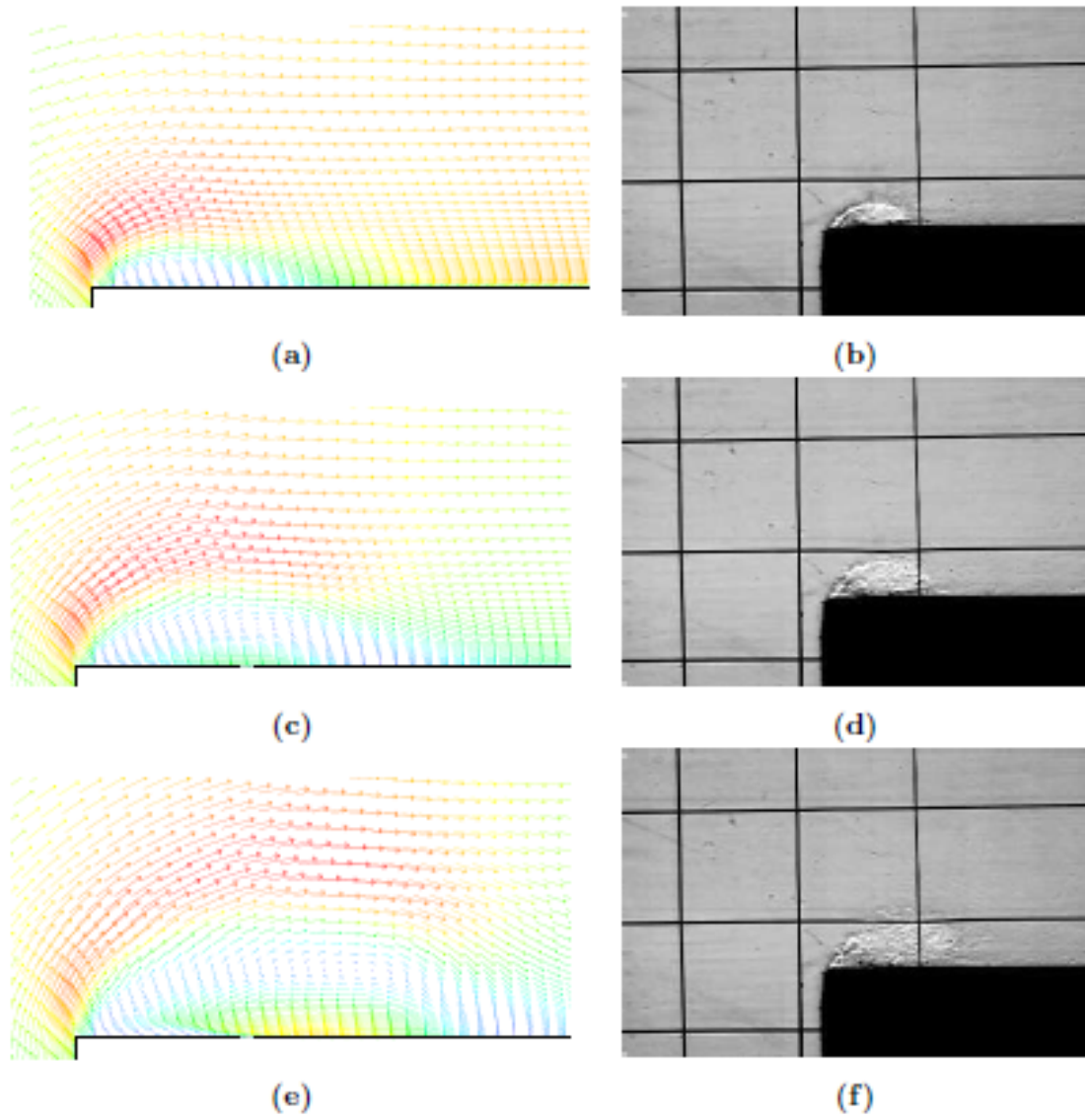


Figure 1.5: Qualitative comparison between Menter's SST $\kappa - \omega$ turbulence model and high-speed shadowgraph images

1.3 Chapter Overviews

This section gives an overview of the layout of this report and a brief introduction to the contents of the chapters. The introductory part of the report includes the following chapters.

- Chapter 2 presents the theory regarding shock tubes, expansion wave dynamics, turbulence modelling and Large Eddy Simulation.
- Chapter 3 introduces the main objectives of the current research. These were divided into two broad sections: (1) expansion wave diffraction around wedges and (2) the Large Eddy Simulation analysis. This separation led to remainder of the report being split into two parts as described below.

Part I

This part of the work involved an extension of the work described in the previous section. An analysis into expansion wave diffraction around wedges of angles 45° , 15° and 5° was conducted. The analysis included both experimental and computational methods. Techniques used in this section were kept very similar to what was done for the 90° corner to allow for comparison between the cases. Only the RANS computational code was used for this analysis. The following chapters were included in Part 1:

- Chapter 4 describes the experimental method. A description of the rig facilities, the test pieces and the visualisation technique is provided.
- Chapter 5 describes the computational method used for the RANS analysis. An overview of the preprocessing and solver set up is given.
- Chapter 6 discusses the results from the experimental and computational methods of the wedge analysis. Constant comparison to what was found previously for the 90° case is given.

Part II

In this part of the work the Large Eddy Simulation solver is employed. Much of the work involved grid development and the solver technique. Due to computational demands and time constraints not many cases were run with the final set up. However, as the main aim was to get a better resolution of the turbulent structures and other flow features found experimentally,

these were sufficient. The analysis mainly focussed on the 90° corner and was followed by a brief discussion of the 15° wedge case. The following sections were included in this part:

- Chapter 7 described the LES computational method including the hybrid RANS/LES domain, grid development, subgrid-scale modelling and solver set up.
- Chapter 8 discusses the results of the LES analysis with comparison to experimental images.
- Chapter 9 lists the conclusions from the discussions in both Part I and Part II.
- Chapter 10 gives recommendations for future work.

Chapter 2 Literature Survey

2.1 Shock Tube Theory

A representation of a constant cross section shock tube is shown in Figure 1.8. The chamber to the left of diaphragm, the driver section, is pressurized and the driven section, shown to the right of the diaphragm, is kept at a lower pressure or left open to the atmosphere. Conventionally, a test section is placed within the driven section of the tube to allow for study of shock wave interactions with objects and high temperature flows. To study expansion wave diffraction, as in the current research, the test section would have to be situated in the driver section of the tube.

The initial shock tube conditions and events generated following rupture of the diaphragm are shown in Figures 1.6 and 1.7. At the time of rupture, an expansion wave propagates into the driver section. Concurrently, a compression wave is generated, which rapidly coalesces into a shock wave and propagates into the driven section. High pressure flow moves from the driver to the driven section. Due to a mismatch in the temperatures of the flow following the expansion and compression respectively, a contact surface forms. The speed and pressure across the contact surface is the constant. For the purpose of analysis the flow through the shock tube is divided into four sections: (1) the flow ahead of the shock wave, (2) the flow following the shock wave until the contact surface, (3) flow between the contact surface and the expansion wave tail and (4) the flow behind the expansion wave head. The shock tube wave diagram in Figure 1.9 illustrates these regions and the position of the waves with time.

The expansion wave head travels at the local speed of sound in region 3 (a_3) and the tail at the speed of sound in region 4 (a_4). Due to the differing temperatures, the leading edge moves faster than the trailing edge and the expansion wave broadens with time. The flow properties within the expansion wave are isentropic and continuous.

The resulting flow field, neglecting wave interaction, is governed by one-dimensional compressible flow equations. Real flow effects including viscosity, heat transfer and surface roughness

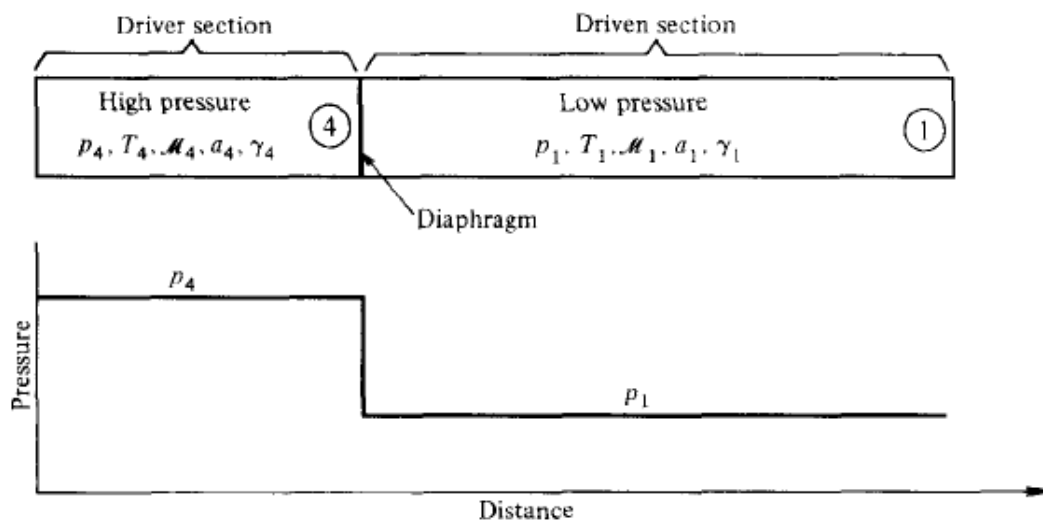


Figure 2.1: Initial shocktube conditions

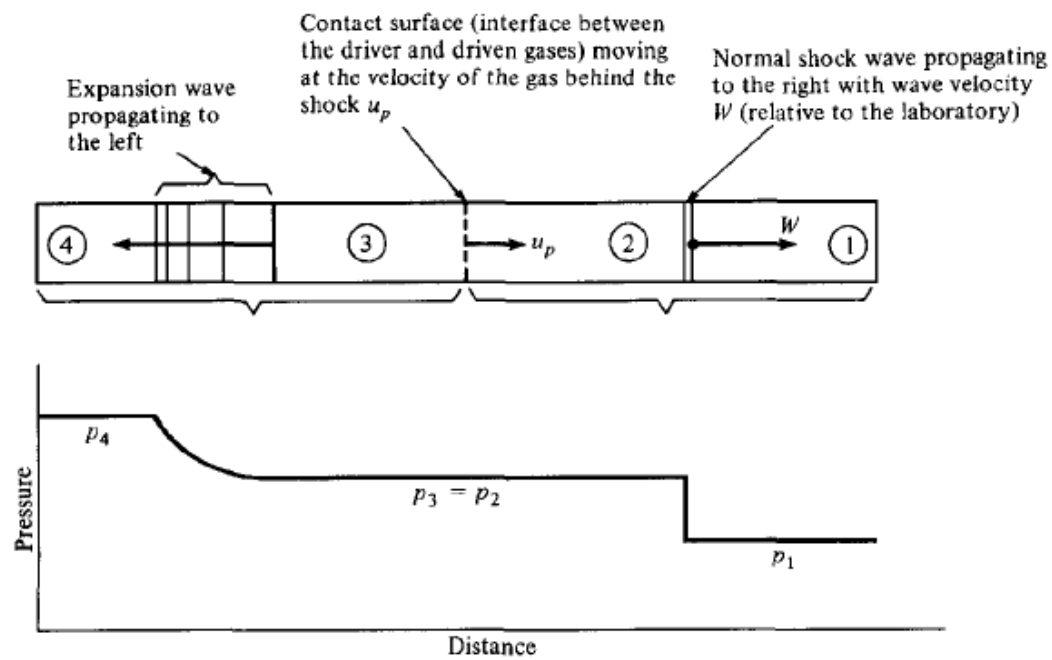


Figure 2.2: Shock tube conditions after diaphragm burst

effects are overlooked in these equations. It should be kept in mind, however, that these would be present in the an experimental set up.

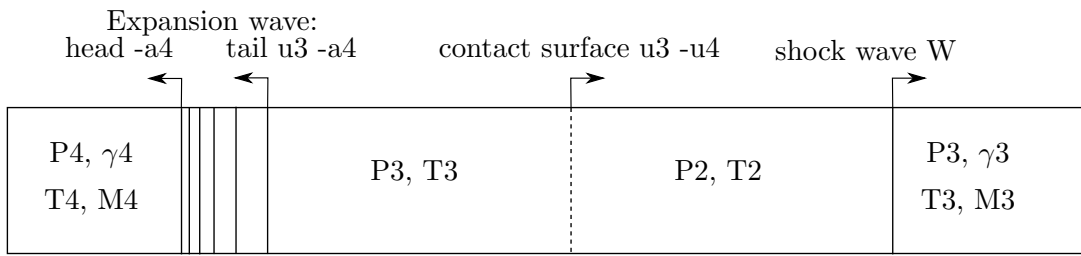


Figure 2.3: Post diaphragm burst shock tube events - Vector notation

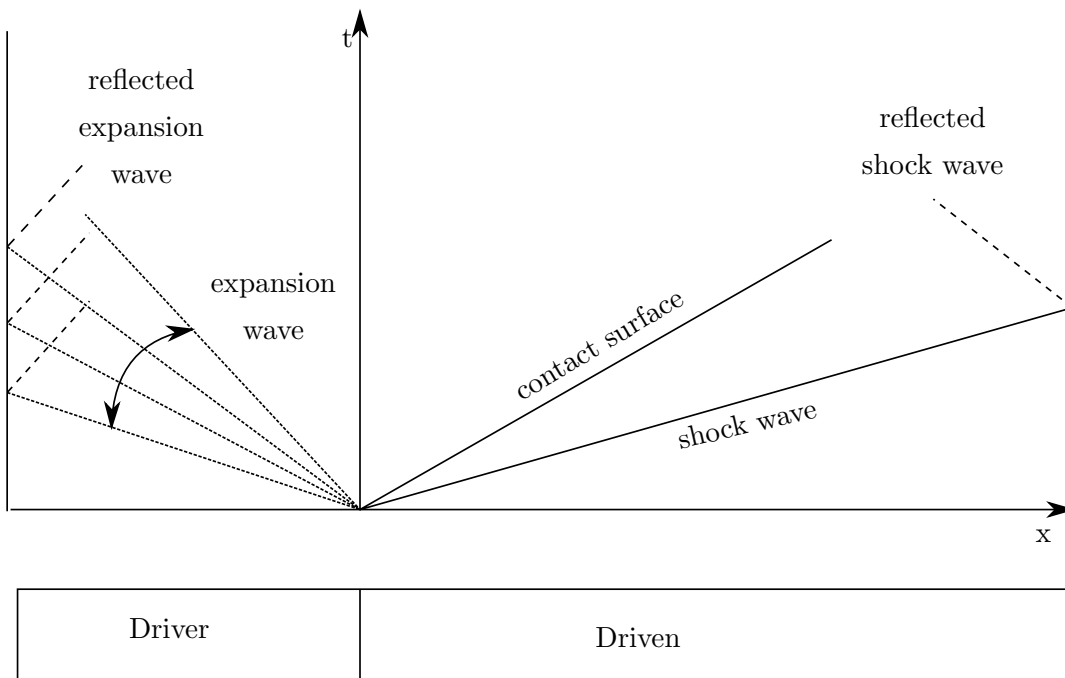


Figure 2.4: Shock tube wave diagram

2.2 Finite Expansion Waves

A finite expansion wave (Figure 1.10) is represented by an infinite number of wave elements between the leading and trailing characteristics. The velocity of each element in the expansion wave is equivalent to the vector sum of the local sound speed within the wave and the induced gas motion. Figure 1.9 shows the velocity vectors associated with the post diaphragm-burst shock tube events.

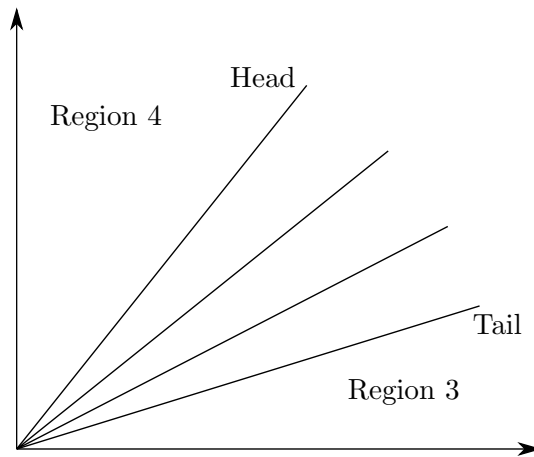
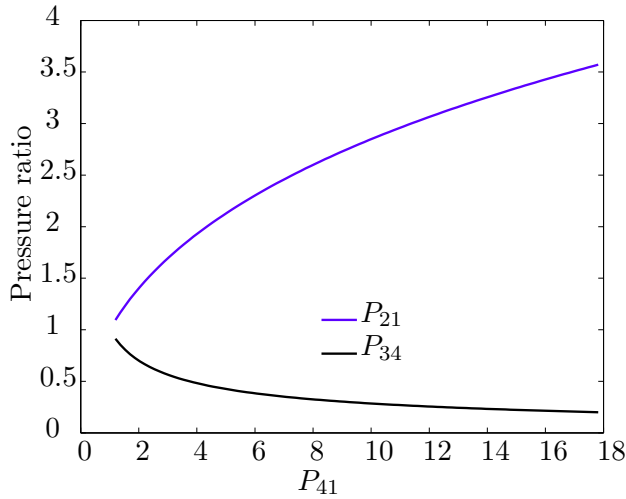


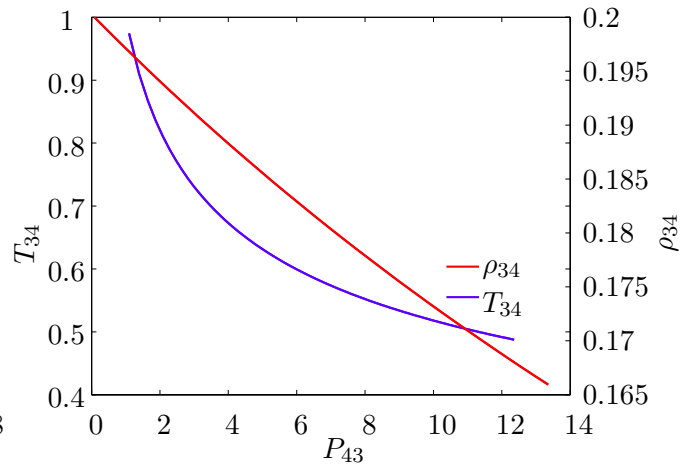
Figure 2.5: Finite Expansion Wave Diagram

2.2.1 Basic One Dimensional Expansion Wave Dynamics

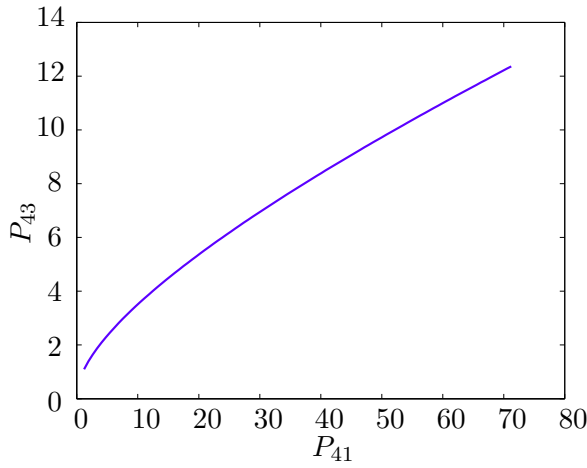
The pressure, density and temperature plots shown in Figures 1.11 describe the predicted behaviour of a one-dimensional expansion wave. Figure 1.11a shows the variation of the shock wave and expansion wave strengths with the initial pressure ratio, P_{41} . Increasing P_{41} shows a steady increase in the shock strength. The expansion wave strength decreases, tending towards zero, as the diaphragm pressure ratio is decreased.



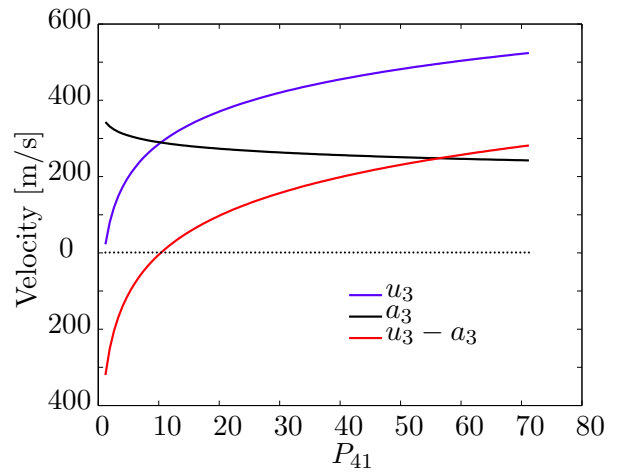
(a) P_{21}, P_{34} versus P_{41}



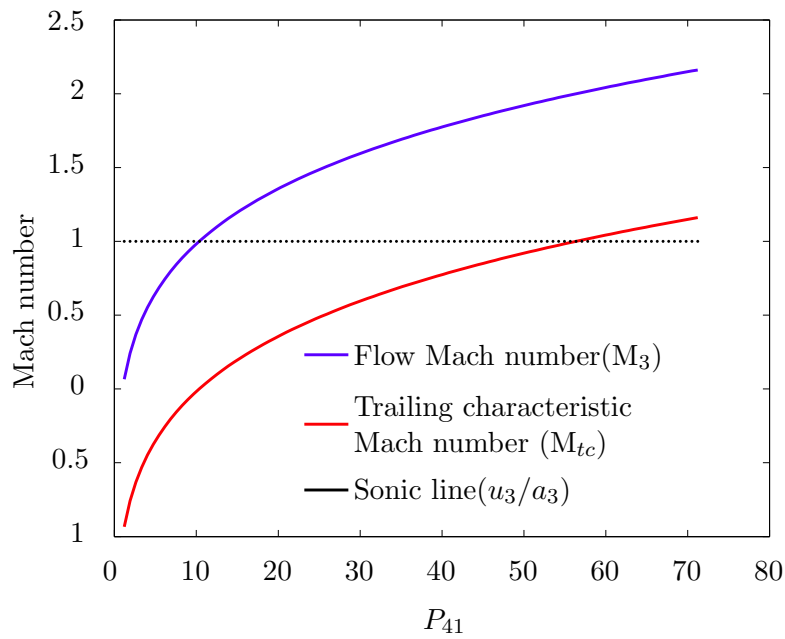
(b) ρ_{34}, T_{34} versus P_{43}



(c) P_{43} versus P_{41}



(d) u_3, a_3 and $u_3 - a_3$ versus P_{41}



(e) M versus P_{41}

Figure 2.6: Expansion Wave Behaviour [4]

The variation of the density and temperature through the expansion wave is shown in [1.11b](#). P_{41} was non-dimensionalised by the static pressure in the driven section. Non-dimensionalising the temperature, T_{34} and density, ρ_{34} was achieved using values from region 4.

Figure [1.11c](#) shows the variation of P43 with P41. The value of P34 for a specific diaphragm ratio can be determined from the graph by calculating the reciprocal $1/P43$. P43 can be used to extract the density and temperature from the plots in Figure [1.11b](#) without the need to calculate the shock strength P21.

The flow velocity in region 3 of the tube is indicated by the blue line in Figure [1.11d](#). The red curve shows the propagation of the trailing characteristic. The trailing edge velocity is seen to adopt negative values for $P41 < 10.4$. At $P41 = 10.4$ an intersection of the flow velocity and local sound speed occurs indicating that at this pressure ratio the trailing edge flow velocity is equivalent to the local sound speed.

The range $u_3 - a_3 < 0$ (where the red plot in Figure [1.11d](#) lies below the x-axis) indicates subsonic flow through the expansion wave. In this case both the leading and trailing characteristics propagate to the left. For $u_3 - a_3 > 0$, the leading and trailing edges would travel in opposite directions.

It would be useful to note that a wave speed of Mach 1 with supersonic flow in region 3 occurs at a pressure ratio of $P41 = 56$. This was determined from the plots in [1.11e](#).

2.2.2 Supersonic flow

Flow through an expansion wave will undergo smooth acceleration until it reaches the trailing edge. This is accompanied by a reduction in temperature and consequent increase in Mach number through the wave. This gives rise to the possibility of sonic and supersonic flow within the wave. The direction of propagation of the expansion wave's trailing characteristic is affected by the Mach number as described in [Table 1.1](#).

Previous analysis [\[4\]](#) has determined that the minimum pressure ratio for supersonic flow through the expansion wave can be expressed as

$$\frac{P_4}{P_1} = k_1 \frac{P_4}{P_1} \left\{ 1 - \frac{(\gamma_4 - 1) \left(\frac{a_1}{a_4}\right) \left(k_1 \frac{P_4}{P_1} - 1\right)}{\sqrt{2\gamma_1 [2\gamma_1 + (\gamma_1 + 1) \left(k_1 \frac{P_4}{P_1} - 1\right)]}} \right\}^{\frac{-\gamma_4}{\gamma_4 - 1}} \quad (2.1)$$

Table 2.1: Relationship between trailing edge direction and Mach number (Left running expansion wave)

Mach number	Trailing Characteristic Direction
< 1	\leftarrow
1	0
> 1	\rightarrow

where,

$$k_1 = \left(\frac{2}{\gamma + 1} \right)^{\frac{2\gamma}{\gamma - 1}} \quad (2.2)$$

Consider the finite width expansion wave depicted in Figure 1.9 with subsonic ($M_f < 1$) flow through the wave. The leading characteristic travels at the sound speed, a_4 and the trailing end velocity is given by $u_3 - a_3$. Assuming the velocities remain constant with time, the distances covered by the leading and trailing characteristics are $s_L = a_4 t_1$ and $s_T = (u_3 - a_3)t_1$. The expansion wave width is determined by subtraction of the two values.

For $M_f \geq 1$ the trailing characteristic travels to the *right* and $s_T < 0$. The expansion wave width then becomes the sum of s_L and s_T . For $M_f = 1$, $s_t = 0$ and the trailing edge remains stationary. In this case the expansion wave width is determined only from the position of the leading edge relative to the wave origin.

For constant initial shock tube conditions the expansion wave width is solely a function of the initial diaphragm pressure ratio. Figure 1.12 indicates the relationship of the expansion width with time for different pressure ratios. The wave's width increases linearly with time with the gradient increasing as $P41$ is increased. The gradient steepening decreased as $P41$ increased.

2.2.3 Expansion Wave Propagation Speed

For a left running expansion wave, the leading and trailing characteristic velocities are $-a_4$ and $u_3 - a_3$ respectively. Increasing the propagation speed of the wave can be achieved by maximising the magnitude of a_4 and minimising the difference between the velocities u_3 and a_3 . The values a_4 , u_3 and a_3 , can be shown to depend directly on the parameters M_1, γ_1, P_1, T_1 and M_4, γ_4, P_3, T_4 .

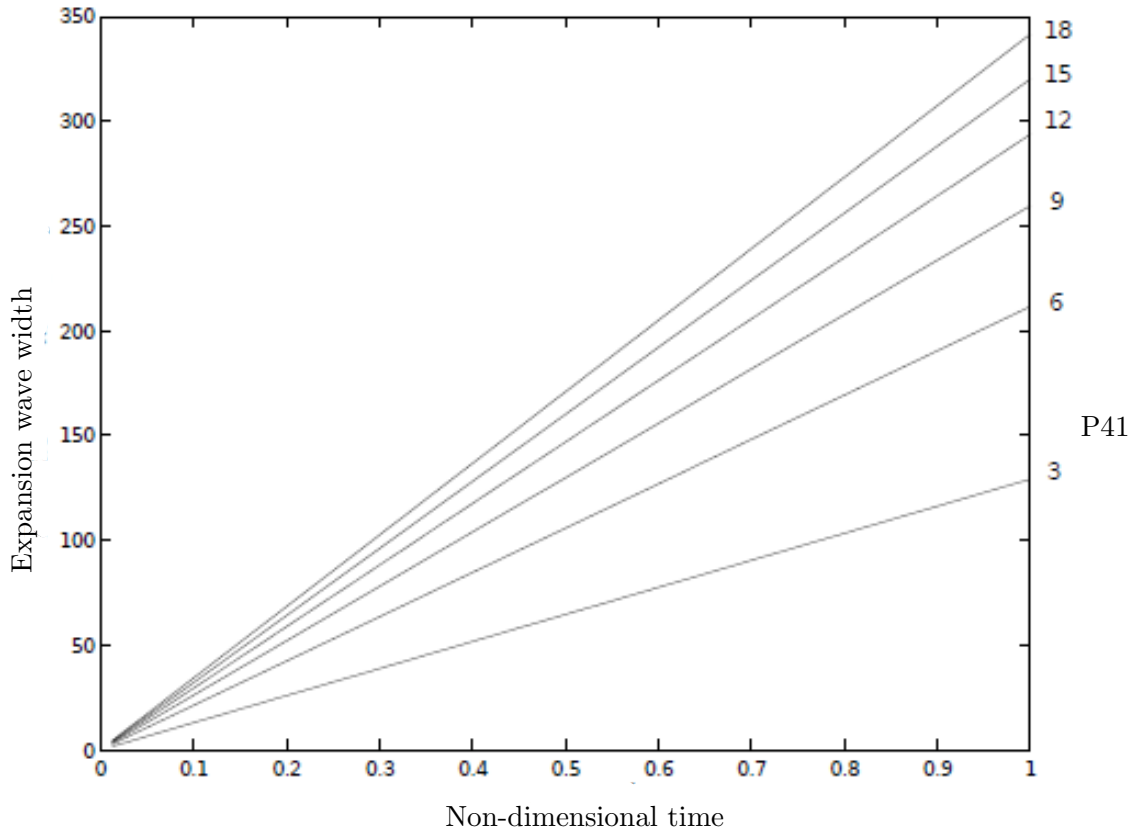


Figure 2.7: Variation of expansion wave width with P41

2.3 Turbulence

This section gives a brief introduction to compressible turbulence dynamics and turbulence modelling in CFD. This discussion would be necessary as turbulence dynamics plays an important role in the theory behind the current subgrid-scale turbulence models which are employed in the LES part of this work. Subgrid scale models are discussed further in Section [1.7.2](#).

2.3.1 CFD and turbulence modelling

In a Computational Fluid Dynamics (CFD) simulation the Navier Stokes equations (governed by mass, momentum and energy conservation) are solved through the entire flow field. For inviscid flow, the Navier Stokes equations are reduced to the Euler's equations by setting the fluid viscosity to zero. For viscous flow, however, the equations represent the full range of velocity fluctuations within the field and are able to accurately predict a large number of flows.

Turbulence is a three-dimensional (3D) and unsteady phenomena occurring over a wide range of scales. Large eddies (with scales on the order of flow passages) contain most of the turbulent kinetic energy. This energy cascades into the smaller eddies and is then dissipated. Thus CFD solvers need to resolve a large number of scales to accurately model turbulent structures in a flow. The domain resolution needs to be at least an order of magnitude larger than the turbulent velocity energy scales and fine enough to resolve the smallest dynamically-significant length scales (the Kolmogorov micro-scale). Direct numerical simulation (DNS) solves the full Navier-Stokes equations using a highly refined mesh to resolve all the turbulent scales from the smallest to the largest eddies. This implies extreme computational costs and consequently may only be used for a very limited number of flows.

Significantly reducing the computing requirements, the Navier Stokes equations are decomposed into the Reynold's Averaged Navier Stokes (RANS) equations to provide feasible solutions to complex engineering flows. The RANS equations result from applying Reynold's decomposition to the Navier Stokes equations. This involves separating the unsteady, turbulent velocity fluctuations from the mean flow velocity. A turbulence model is then required to solve the unknown Reynold's stresses resulting from the decomposition process.

Currently, the industry standard used in CFD turbulence modelling is RANS. However, RANS models are calibrated to provide reasonable predictions for flows in which some degree of universal behaviour is displayed. Conversely, for models where the geometry has a significant effect on the turbulence dynamics of the flow, RANS models generally do not accurately capture the flow field [5]. RANS solvers fail when it comes to complex, unsteady turbulent flows without clear scale separation [6]. Spalart [7] has noted two primary challenges in turbulence modelling, (1) the ability to predict the growth and separation of the boundary layer and (2) the prediction of the momentum heat and mass transfer in separated flow. RANS models generally handle the first but prove ineffective with regards to the second.

2.3.2 Compressible Turbulence Dynamics

For shear compressible flow without shocks a simple, variable-density extension can be added to the subgrid models developed for incompressible flow. The addition would directly account for the compressibility effects on the larger eddies which are responsible for the kinetic energy production and anisotropy production.

When concerned with compressible flow involving shocks one needs to consider that shock phenomena occur at lengthscales much smaller than the scales of motion. With such flow, two additional lengthscales need to be considered, the shock thickness and a characteristic

shock corrugation length. These scales are significantly shorter than the turbulence integral and lengthscale and even the Taylor microscale. The shock thickness, δ , is estimated as [[8]],

$$\frac{\eta}{\delta} \approx 0.13 \frac{M_1 - 1}{M_t} \sqrt{Re_\lambda} \quad (2.3)$$

where, M_1 is the upstream Mach number, M_t the turbulent Mach number, η the Kolmogorov lengthscale and Re_λ the Taylor-micro-scale Reynold's number. The last case to consider is flow without shocks or turbulence production. In this case the effects of compressibility on scale interactions need to be analysed as the main dynamic mechanism is the nonlinear transfer of kinetic energy between scales of motion. Kovazsnay's decomposition represents the additional mechanisms that arise due to compressibility by the acoustic mode and entropy mode [8].

Compressible flow is defined by significant density fluctuations as a result of pressure perturbations in the field. The density variations are associated with local velocity diversions. Turbulence can be broken down into three modes of fluctuations - vorticity, acoustic and entropy. At higher orders of analysis mode coupling occurs and "any two modes can interact through non-linearities and generate all three modes". Additionally, turbulent velocity can be described by a superposition of a solenoid component and an irrotational component (from Helmholtz decomposition). As opposed to incompressible flow, compressible flow concerns the dilational rather than the solenoid field. In the solenoidal field the energy cascade results from the interaction of the vortices of the field with the viscous forces and non-linearities. In the dilational field, kinetic energy and energy contained in thermodynamic fluctuations are exchanged. The dilational field is propagative and undulatory. For incompressible flow the turbulent production and solenoid dissipation account for most of the energy. However, dilational dissipation and the pressure dilation correlation due to the dissipation of compressible turbulence results in additional energy transfer in compressible flows. As a result, for compressible flow, subgrid scale models do not only have to account for interscale energy transfer but also need to consider intermodal energy transfer. At the current time there exists no accurate subgrid scale compressible flow extension [8].

2.4 Large-Eddy Simulation

Large Eddy Simulation (LES) is a CFD solver which was proposed in the 1960s but remained infeasible to simulate complex engineering flows due to its relatively high computing requirements. In LES large eddies are solved directly and only smaller scale motion is modelled. It is thus expected that the turbulent flow structures within the separation bubble (as well as the other flow features) may be well resolved using LES. One of the main focuses of this

study is to investigate the use of LES in studying the flow field generated by expansion wave diffraction.

RANS solvers solve for averaged values in the Navier-Stokes equations and a turbulence model is used to model all instantaneous turbulent motion scales. In certain flows involving anisotropic turbulent, vortical structures (like wake regions), mean values result in RANS models producing unsatisfactory results.

A third solution, called large-eddy simulation (LES) lies between DNS and RANS in terms of both cost and accuracy. The model numerically resolves all large scale motions and models smaller (subgrid) scales. Since most of the turbulent energy is contained within the large eddies and they are responsible for most of the turbulent mixing and momentum transfer, the accuracy obtained from LES is significantly higher than with RANS solvers. A comparison between the DNS and LES scales is depicted in Figure 1.13.

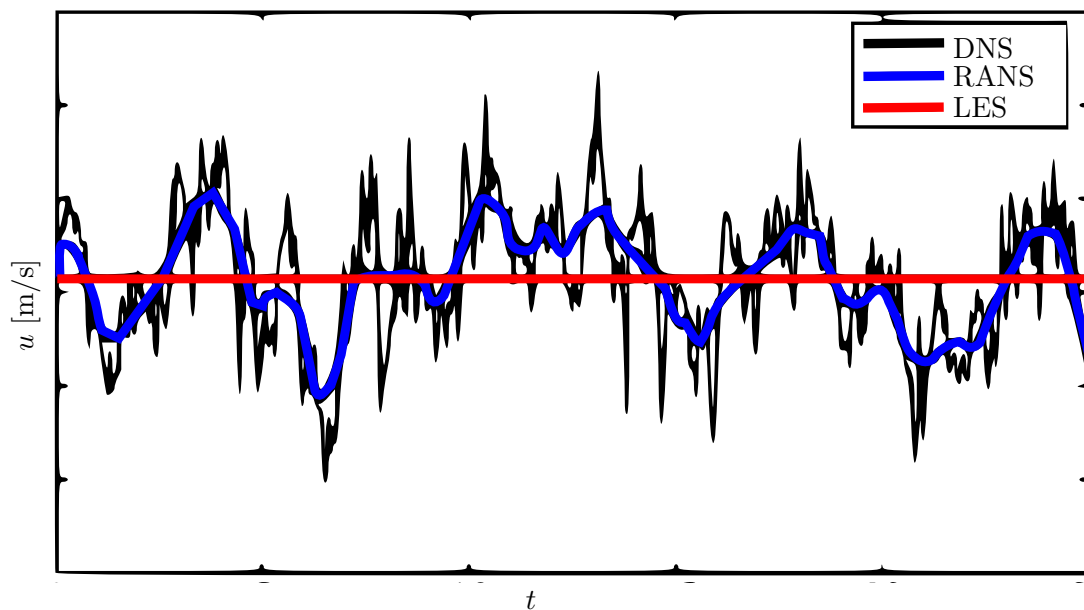


Figure 2.8: Comparison between resolved scales of motion for RANS, LES and DNS

The motivation behind LES is derived from the following arguments [9]:

- Most of the turbulent momentum, energy and mass transfer occur due to the larger eddies.
- Large eddies are highly dependent on the model geometry and flow boundary-conditions.
- Smaller eddies are universal, isotropic and less dependent on the problem geometry.

- Universal turbulence models stand a much better chance of modelling smaller scale motions.

The Large Eddy Simulation equations are derived by applying a low-pass spatial filtering scheme to the Navier-Stokes conservation equations to remove the smaller universal scales. This differentiates between the universal, smaller and the larger, geometry dependant scales.

2.4.1 Hybrid LES-RANS models

Due to the substantially reduced turbulent length scales near the wall in relation to the boundary layer thickness (especially at high Reynold's numbers), there are serious limitations for LES as the computational effort drastically increases. To counter this issue several hybrid (RANS-LES) models are available in which large eddies away from the wall are solved using LES and wall boundary layers are covered by RANS. These models include Detached-Eddy simulation (DES) and Scale-Adaptive-Simulation (SAS). The DES model switches between RANS and LES depending on the grid resolution thus free shear flows are covered by LES and boundary layers by RANS.

An additional hybrid model, Wall-Modelled LES (WMLES), has been developed to model flow in the innermost part of the boundary layer using a RANS model while the main part of the boundary layer is solved with LES. WMLES thus reduces the grid resolution requirements and its dependence on the Reynold's number. As the distance from the wall increases there is a linear increase in the near-wall turbulence length scales. In the viscous sublayer, molecular viscosity dampens out the effects of these eddies. However, as the Reynold's number is increased, eddies reduce in size due to the thinning of the viscous sublayer. These small eddy's are resolved by RANS to eliminate the associated excessive computational times.

In addition to the above global hybrid schemes a further solution, optimised for large domains, involves splitting the domain and modelling majority of the flow with a RANS model and covering (smaller) areas of interest with LES. This technique is called Zonal or Embedded LES (ELES). When setting up ELES the user would specify regions where LES is required ahead of time. An illustration of an ELES zone is shown in [Figure 1.14](#).

2.4.2 Subgrid-Scale Models

Filtering the Navier-Stokes equations result in unknown subgrid-scale stresses which are modelled using subgrid-scale (SGS) models. Modelling the SGS stresses is based on the hypothesis that the energy transfer between the subgrid and modelled scales is sufficient to describing

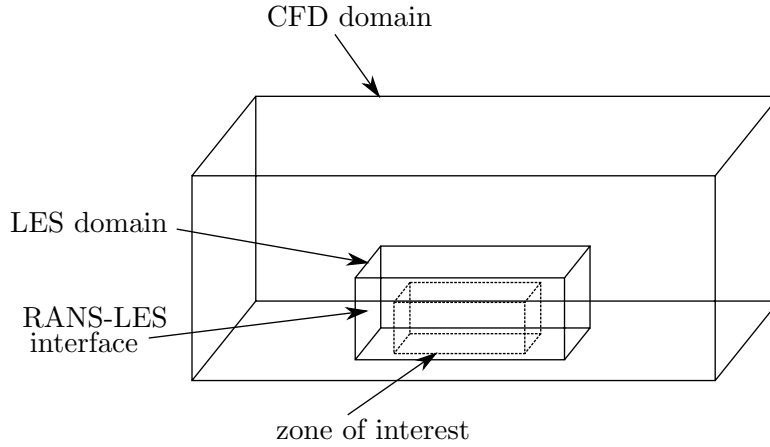


Figure 2.9: Embedded LES Domain

the subgrid scales [8]. The energy transfer is either a forward transfer, towards the subgrid scales or backwards, towards the resolved scales. The latter, known as backscatter, occurs at a much lower intensity.

The Boussinesq Hypothesis is used to model the subgrid turbulent stresses. The hypothesis is derived from the analogous relation between the energy transfer caused by molecular viscosity in a gas and the energy transfer from the modelled to the subgrid scales. Accordingly, the mathematical structure of the turbulent energy cascade would be similar to that of molecular diffusion. The subgrid-scale turbulent stresses are computed from

$$\tau_{ij} - \frac{1}{3}\tau_{kk}\delta_{ij} = -2\mu_t\bar{S}_{ij} \quad (2.4)$$

where μ_t is the subgrid-scale turbulent viscosity. Introducing Favre filtering for compressible flows, the subgrid model is derived as

$$\tau_{ij} - \frac{1}{3}\delta_{ij}\tau_{kk} = -2\mu_t(S_{ij} - \frac{1}{3}S_{kk}\delta_{ij}) \quad (2.5)$$

The following four models for μ_t are offered in ANSYS Fluent [9].

Smargorinsky-Lilly Model

The Smargorinsky-Lilly model models the eddy viscosity by

$$\mu_t = \rho L_s |\bar{S}| \quad (2.6)$$

where L_s is the mixing length for SGS and $|\bar{S}| \equiv \sqrt{2\bar{S}_{ij}\bar{S}_{ij}}$. The mixing length is determined as the minimum of κd and $C_s \Delta$ where κ is the von Karman constant, d is the distance to the closest wall, C_s is the Smargorinsky constant and Δ is grid spacing.

The Smargorinsky constant represents the relationship between the non-resolved scale mixing length and the filter cut-off length. The value of C_s typically ranges between 0.1 and 0.2 where 0.1 has been found suitable for a wide range of flows. However, setting C_s as a universal constant is inaccurate as the SGS viscosity expression is localised in space and time [8] and has to be reduced drastically in certain parts of the flow (reducing the eddy viscosity by one or more orders of magnitude [10]). The model is thus inaccurate for high Reynold's number and complex flows.

Dynamic Smargorinsky-Lilly Model

The Dynamic Smargorinsky-Lilly Model calculates the value of C_s from the resolved scales. This is achieved by applying a second filter, twice the size of the original filter. The difference between the resolved fields from the two filters represents the contribution of the small scales and is used to determine C_s [9].

Wall-Adapting Local Eddy-Viscosity (WALE) Model

The WALE model calculates the eddy viscosity based on the square of the velocity tensor to improve near wall behaviour.

Algebraic Wall-Modelled LES (WMLES) Model

The excessive resolution and time step size required by LES within wall boundary layers make simulating high Reynold's number flow highly infeasible. WMLES is a solution which allows a switch to a RANS model in the near wall portion of the boundary layer (inner logarithmic layer) and the rest of is covered with a modified LES formulation.

The eddy viscosity model combines the mixing length model with the modified Smargorinsky model and the Piomelli damping function.

The following list defines the research objectives intended for the current study as introduced in Section 1. The study is divided into two sections:

1. To investigate expansion wave diffraction around sharp convex corners
 - To analyse, experimentally and computationally, expansion wave diffraction around sharp, convex corners and the effect on the surrounding flow field including the near corner flow structure.
 - Investigate the effects of initial pressure ratio, wedge angle and diaphragm distance from the diffraction corner.
2. To analyse expansion wave diffraction using the Large Eddy Simulation CFD model
 - To attempt to resolve the experimentally determined turbulent structures in the separation bubble and wake region.
 - To further investigate the nature and structure of the separation bubble

Part I

Analysis of expansion wave diffraction around sharp convex wedges

Chapter 3 Experimental Method

3.1 Experimental facilities

For the purpose of the experimental work a shock tube had to be specifically designed to allow for visualization of expansion wave phenomenon. Upon diaphragm rupture the expansion wave propagates upstream into the driver section. Consequently, the current rig design comprises of a test section with viewing windows placed in the driver section rather than the driven as per convention. The driver and driven sections are separated by a gas-tight diaphragm. The end of the driven section was left open to the atmosphere. A schematic illustrating experimental set up and rig dimensions given in Figure 2.1.

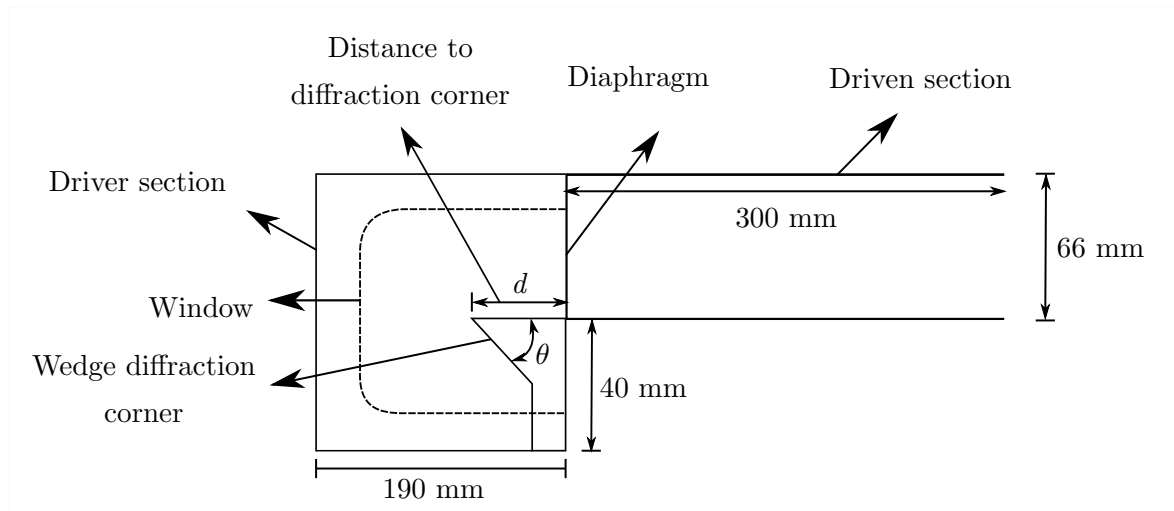


Figure 3.1: Schematic of the experimental set up

Figure 2.2 shows a CAD image of the shock tube design. The test pieces are bolted to the bottom plate of the driven section. The rig was assembled on a guide rail system to allow the driven section to be slid away for the test pieces to be changed and the diaphragm placed. O-ring grooves were situated on the top, bottom and back plates of the driver section to prevent leakage.

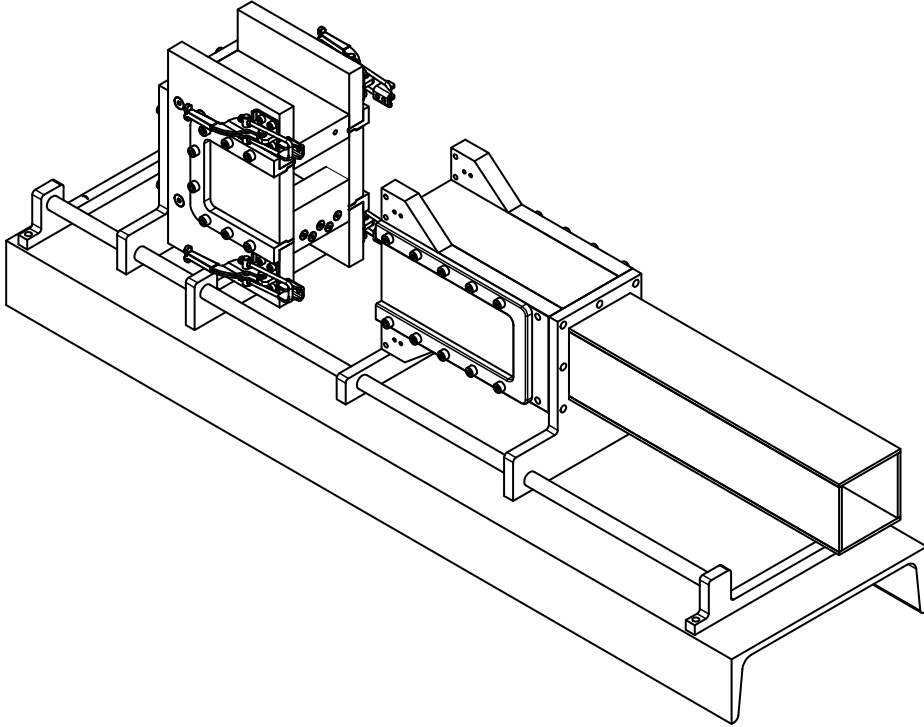
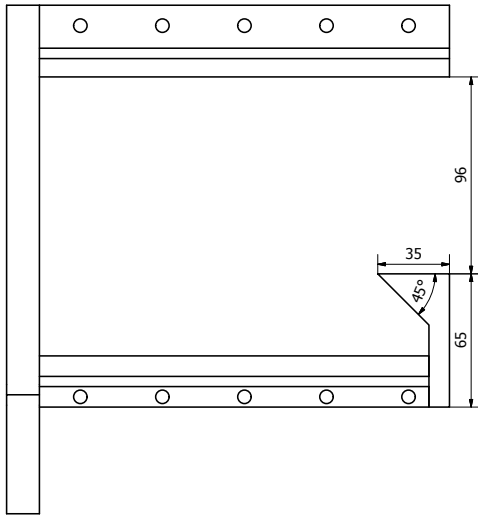


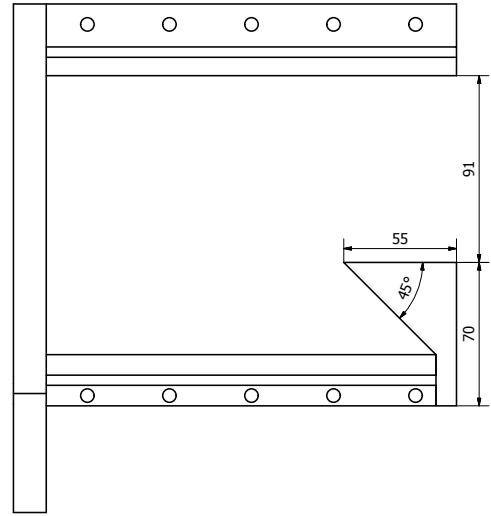
Figure 3.2: CAD image of the experimental rig

Four different test pieces were used with combinations of the two wedge angles, $\theta = 45^\circ$ and 15° , and diaphragm distances, $d = 35$ mm and 55 mm. The dimensions of the test pieces were constrained by the general assembly of the rig. Figures 2.3 show schematics of the assembly and dimensions of each test piece.

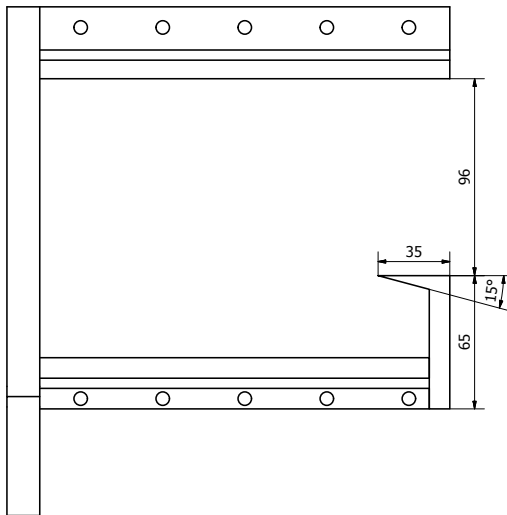
An aluminium shim stock diaphragm material used with a thickness of $75 \mu\text{m}$. The diaphragm burst naturally at an approximate pressure of 1 bar. Due to the unavailability of thicker diaphragm material, to achieve higher pressures multiple diaphragms had to be layered. Grease was smeared onto the diaphragms before they were coupled in order to hold them together. Table 2.1 shows the driver pressures achieved as the number of diaphragms were increased. Use of grease between the diaphragm material had the disadvantage of messing the test section windows after it burst which made the optical images very messy. The diaphragm was scored in an 'X' pattern which would result in two of the petals opening up against the windows of the driven part of the test section. Unfortunately, this blocked out the wake region completely and at later times part of the separation bubble.



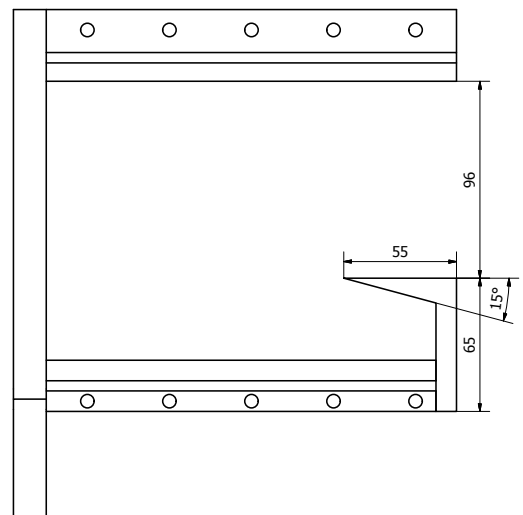
(a) 45° , $d = 35$ mm



(b) 45° , $d = 55$ mm



(c) 15° , $d = 35$ mm



(d) 15° , $d = 55$ mm

Figure 3.3: Test Pieces

Table 3.1: Driver Pressures with multiple diaphragms

Number of diaphragms	Driver pressure [bar]
1	1
25	1.8
35	3.6

3.2 Optical Visualisation

Flow visualisation was achieved using a schlieren imaging system. A basic Z-configuration set up, shown in Figure 2.4, was used. Two guide rails were placed at approximately 15° to the horizontal. The optical equipment used used comprised of:

- A light source. A continuous light source [Megaray MR-LL17] was used for high-speed imaging.
- A condensing lens
- Two pairs of adjustable knife edges were used; one on the light source side and the other on the camera side.
- A cylindrical lens to correct astigmatism
- Two parabolic mirrors
- A focusing lens
- A Photron FASTCAM SA5 camera was used for high speed imaging at 60 000 fps.

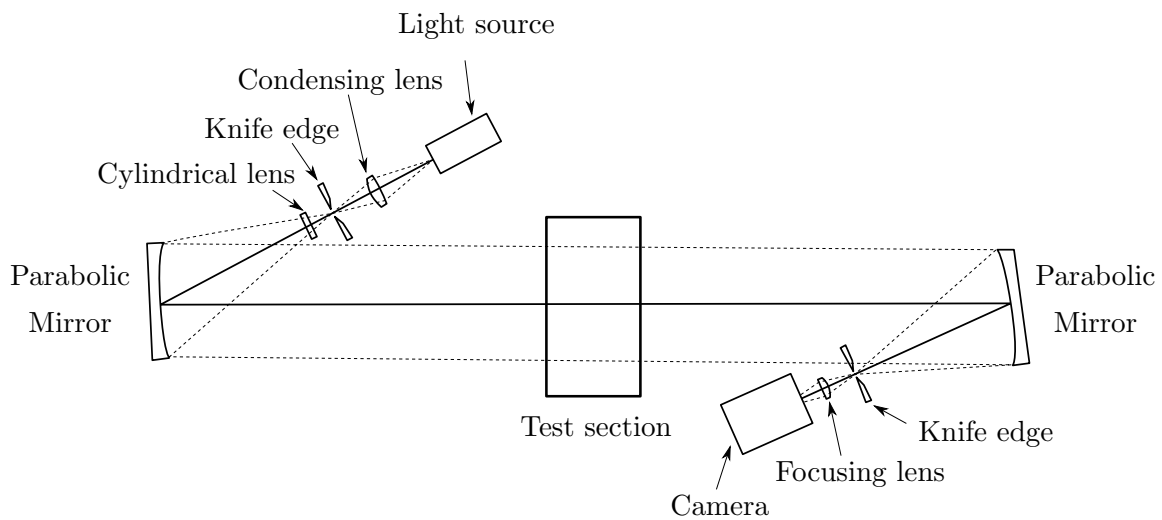


Figure 3.4: Optical Visualisation Setup

Chapter 4 Computational Method

The computational method described in this section served as the principal investigative tool for the current study. The accompanying experimental investigation was used to validate the computational code as spatial constraints limited the number of cases that could be tested. As a result, for the computational analysis, an initial *experimental domain* was constructed to the dimensions of the shock tube allowing for comparison between the computational and experimental results. A second, *extended domain*, with larger dimensions was used for majority of the analysis to allow for longer simulation times before the reflected expansion waves from the walls would affect regions of interest.

The grids developed and solution techniques used for the computational method were based on the study by Mohamed [4] for the case of a 90° corner. The methods were retained for the current study to allow for comparison between the 90° case and the wedges studied in this analysis. The reader is referred to the referenced manuscript for discussions on the grid independence and turbulence modelling studies.

4.1 The Computational Domains

The Experimental Domain

The schematic of the experimental domain is shown in Figure 3.1. The variable d represents the distance of the diffraction corner from the diaphragm. The experimental analysis considered $d = 35$ mm and 55 mm and $\theta = 45^\circ$ and 15° . The value of b on the diagram would evidently change between the different cases and is tabulated in Table 3.1.

The Extended Domain

The larger extended domain is shown in Figure 3.2. As the values of d and θ were varied, the lengths of a and b had to be changed accordingly and thus differ though the cases.

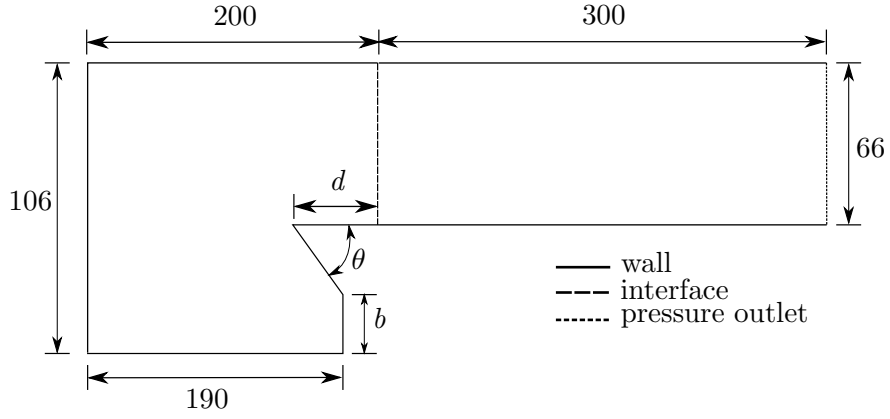


Figure 4.1: Schematic of the Experimental Computational Domain

Table 4.1: Experimental Domain Completing Dimensions

θ	d [mm]	b [mm]
45	35	10
45	55	0
15	35	33.3
15	55	27.9

Table 3.2 lists the completing dimensions for the extended domain. The values of d in the computational analysis were 10 mm, 40 mm and 70 mm. Wedge angles of $\theta = 45^\circ$, 15° and 5° were tested.

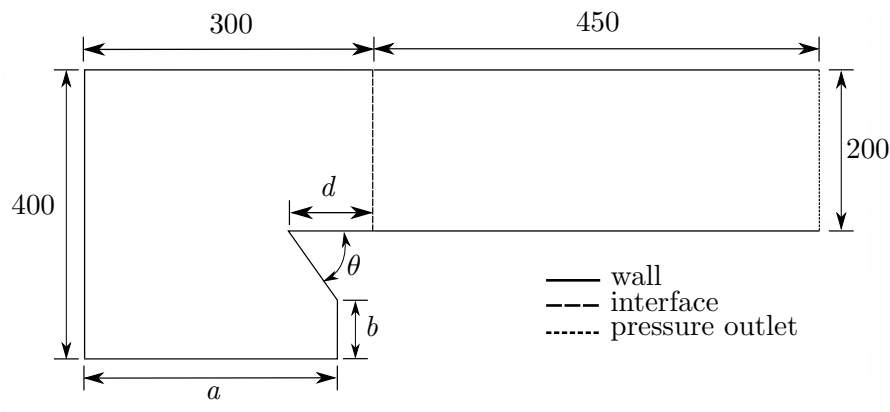


Figure 4.2: Schematic of the Extended Computational Domain

Table 4.2: Extended Domain Completing Dimensions

θ	d [mm]	a [mm]	b [mm]
45	10	410	80
45	40	380	80
45	70	350	80
15	10	410	168
15	40	410	160
15	70	410	151.8

4.2 Grid Development

The grids consisted of $0.6 \text{ mm} \times 0.6 \text{ mm}$ cells across the domain. An inflation layer with a first cell height of 0.015 mm was used on the bottom walls of the driver and driven sections which placed the y^+ in the required range of $5 \leq y^+ \leq 30$. A close up image of the mesh at the diffraction corner for a 45° case is shown in Figure 3.3.

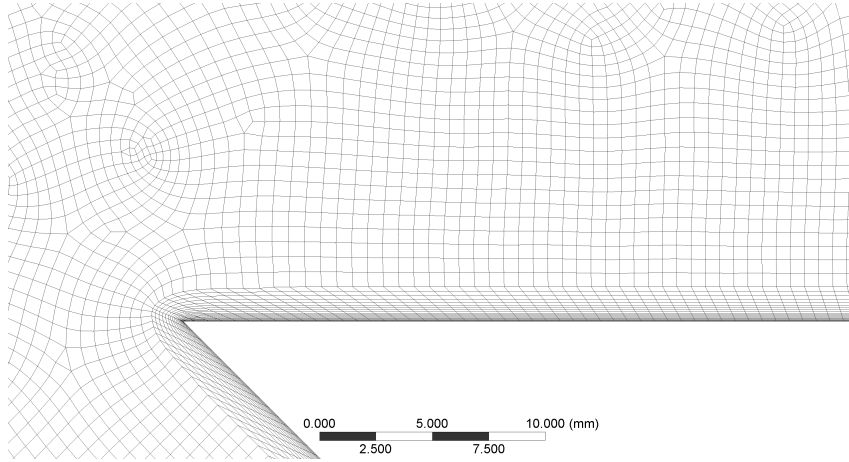


Figure 4.3: Grid topology for 45° corner

In the 15° case the inflation layer resulted in a poor mesh structure at the corner (shown in Figure 3.4). This was solved by dividing the driver section into two blocks horizontally at the corner. A second inflation layer, with a first layer height of 0.1 mm was added along a horizontal line from the corner into the driver section. This allowed a smoother transition of the grid sizing at the diffraction corner. The final grid for the 15° degree case is shown in Figure 3.5.

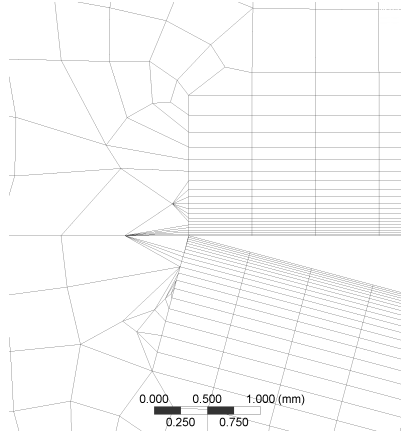


Figure 4.4: Poor grid structure at 15° corner

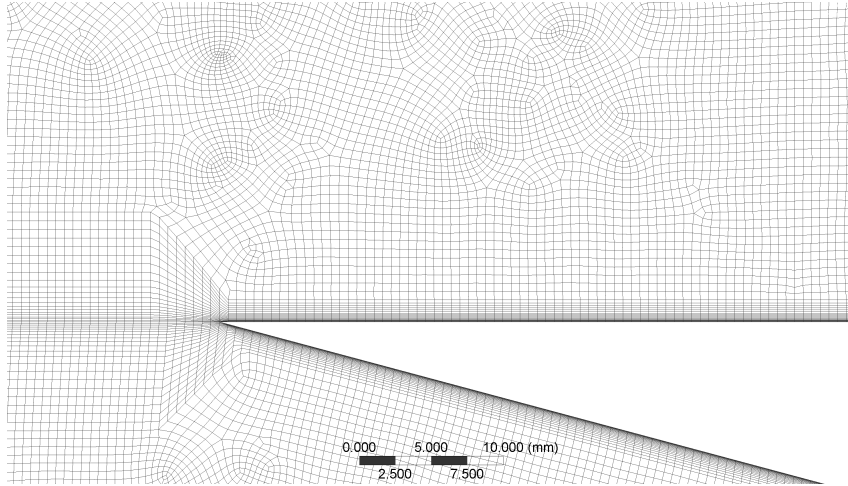


Figure 4.5: Grid topology for 15° corner

4.3 Solver Setup

The computational domain consisted of two sections representing the driver and driven sections. The diaphragm in the shock tube was modelled using an *interface* boundary condition. A pressure outlet, set at the atmospheric pressure was used to represent atmospheric conditions at the end of the driven section. The domain was initialised to atmospheric conditions, $P_{atm} = 83400$ kPa and $T_{atm} = 288$ K. To create the required pressure difference across the diaphragm the driver section was *patched* to the required pressure. The boundary conditions are specified on the domain schematics in Figures 3.1 and 3.2. The initial driver section pressure values used for the extended domain analysis are given in Table 3.3. Initial driver pressures used for the experimental validation conform to those discussed in the experimental setup.

Table 4.3: Experimental Domain Completing Dimensions

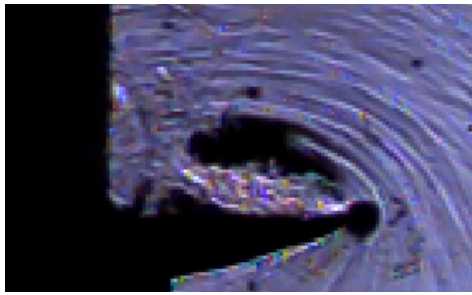
Absolute diaphragm pressure ratio	Absolute driver pressure [kPa]
3	250200
6	500400
9	750600
15	1251000

A density based, implicit solver was used with a fixed time step. This differed from the explicit scheme used for the 90° case. The implicit scheme, using a very small time step (1×10^{-8}) showed much better convergence than the explicit scheme and a comparison of results did not indicate compromise in accuracy. The AUSM+ flux discretization scheme was used and provided better shock resolution than the ROE-FDS scheme. The *least squared cell-based* was used to compute gradients for the spatial discretization. Dynamic mesh adaption was based on the gradient approach.

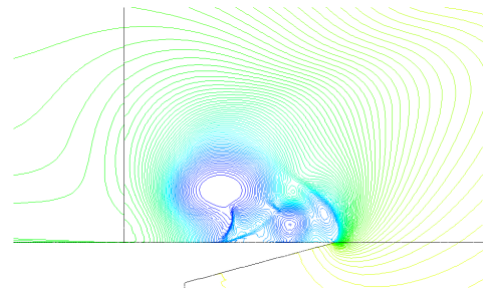
Turbulence modelling was achieved using Menter’s Shear Stress Transport (SST) $k-\omega$ model as the model achieved the closest agreement with experimental analysis in the 90° case [4].

4.4 CFD Validation

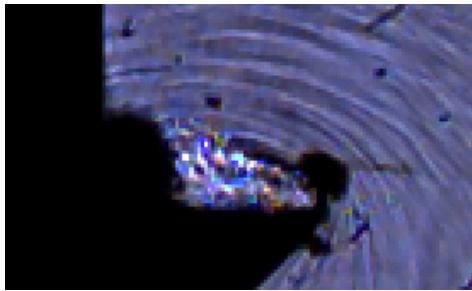
In this section the experimental results are compared with the CFD results to validate the CFD model. Figures 3.6 and 3.7 show a comparison between the schlieren images and the density contour plots for the 45° and 15° corners with $d = 35$ mm and 55 mm. A good agreement is seen with regards to the shape and size of the bubble. In most of the experimental images the reattachment of the shear layer was obscured and a data comparison between the stagnation point from the experimental and computational results could not be done. However, rough approximations show a relatively good correlation between the reattachment points.



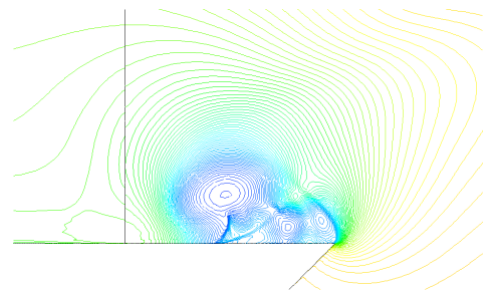
(a)



(b)

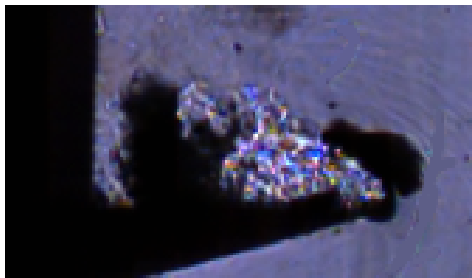


(c)

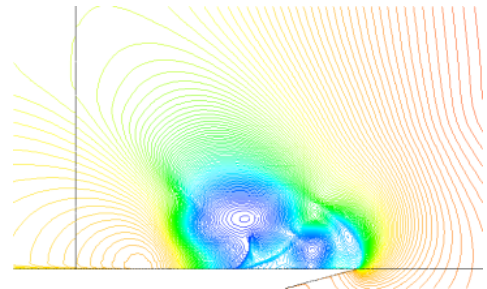


(d)

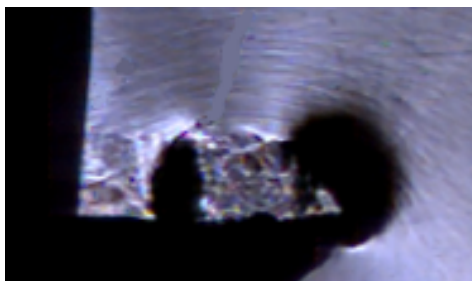
Figure 4.6: Comparison between density contour plots and schlieren imaging $P41 = 4$, $d = 35$ mm, $t = 411 \mu\text{s}$. (a), (b) 15° (c), (d) 45° .



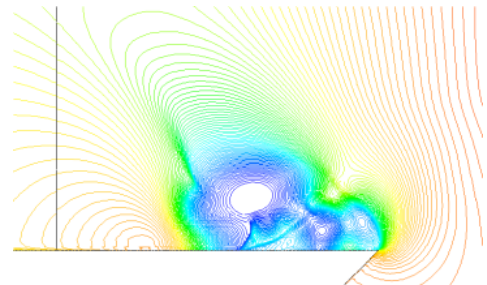
(a)



(b)



(c)



(d)

Figure 4.7: Comparison between density contour plots and schlieren imaging $P41 = 4$, $d = 55$ mm, $t = 612 \mu\text{s}$. (a), (b) 15° (c), (d) 45° .

Chapter 5 Expansion wave diffraction around sharp convex corners

5.1 Introduction

This chapter focusses on analysing the flow field resulting from a planar expansion wave diffracting around sharp convex corners. Initially, a broad overview of the major flow features will be given including a qualitative comparison between the schlieren images and the RANS numerical solutions. This will be followed by more detailed discussions on aspects of interest, in particular, the near corner flow structure.

The discussions will consider the effects of varying the corner angle (θ), the distance between the diaphragm location and the diffraction corner (d) and the initial pressure ratio across the diaphragm ($P41$).

Initially, the chapter will be concerned with diffraction of the expansion wave where the flow behind the trailing characteristic is subsonic. The analysis will extend to consider the flow structure in cases where the flow is sonic or supersonic (for $P41 > 10.4$).

The following analysis will make constant reference to the write up of the previous work on the 90° case [4]. Many of the discussion points below are drawn from there while the results are also used as a comparison case for the other wedge angles considered in the current research.

5.2 Comparison of major flow features

5.2.1 Reflected compression wave

The diffraction of individual elements of the incident expansion wave was found to generate perturbations originating at the diffraction corner. These perturbations would then propagate radially outwards to form a reflected compression wave. The signals propagate into the region behind the incident expansion wave modifying its trailing characteristic. This process was illustrated in Figure 1.4, Section 1 for the 90° case and is reproduced below for $\theta = 45^\circ$ in Figure 4.1.

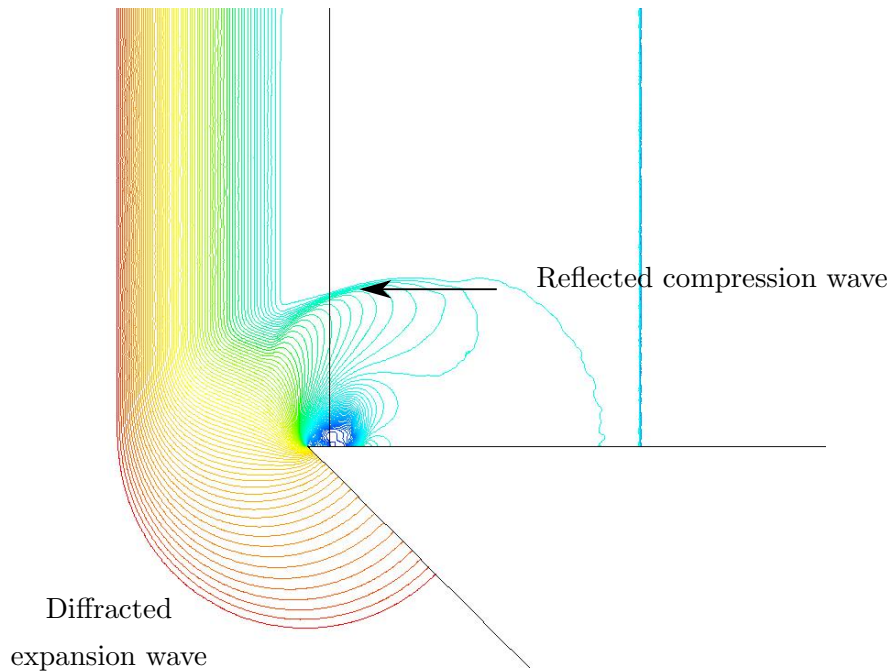


Figure 5.1: Pressure contour plot for $\theta = 45^\circ$, $PR = 6$ and $d = 40\text{mm}$ at a time delay of $t = 250 \mu\text{s}$

The development of the reflected compression wave with time is shown in Figure 4.2 for the corner angles $\theta = 15^\circ$ and 45° at $d = 10\text{mm}$. There were no notable differences in the development and propagation of the compression wave and cylindrical shock between the 90° and the wedge cases.

The compression wave signals for the expansion wave diffraction case would propagate into steady or unsteady flow depending on the width of the incident expansion wave. The width at constant P41 is governed only by the propagation time prior to diffraction which is controlled by the diaphragm distance to the corner. From the investigation on the 90° corner it was found that at low corner distances, $d = 0 \text{ mm}$ and $d = 10 \text{ mm}$, the reflected compression wave would quickly coalesce into a weak cylindrical shock wave which can be seen in Figures

4.2e and 4.2f. For larger d values, the broader incident expansion wave would take longer to propagate into the downstream flow. Figure 4.3 shows the propagation of the reflected compression wave for $d = 70\text{mm}$.

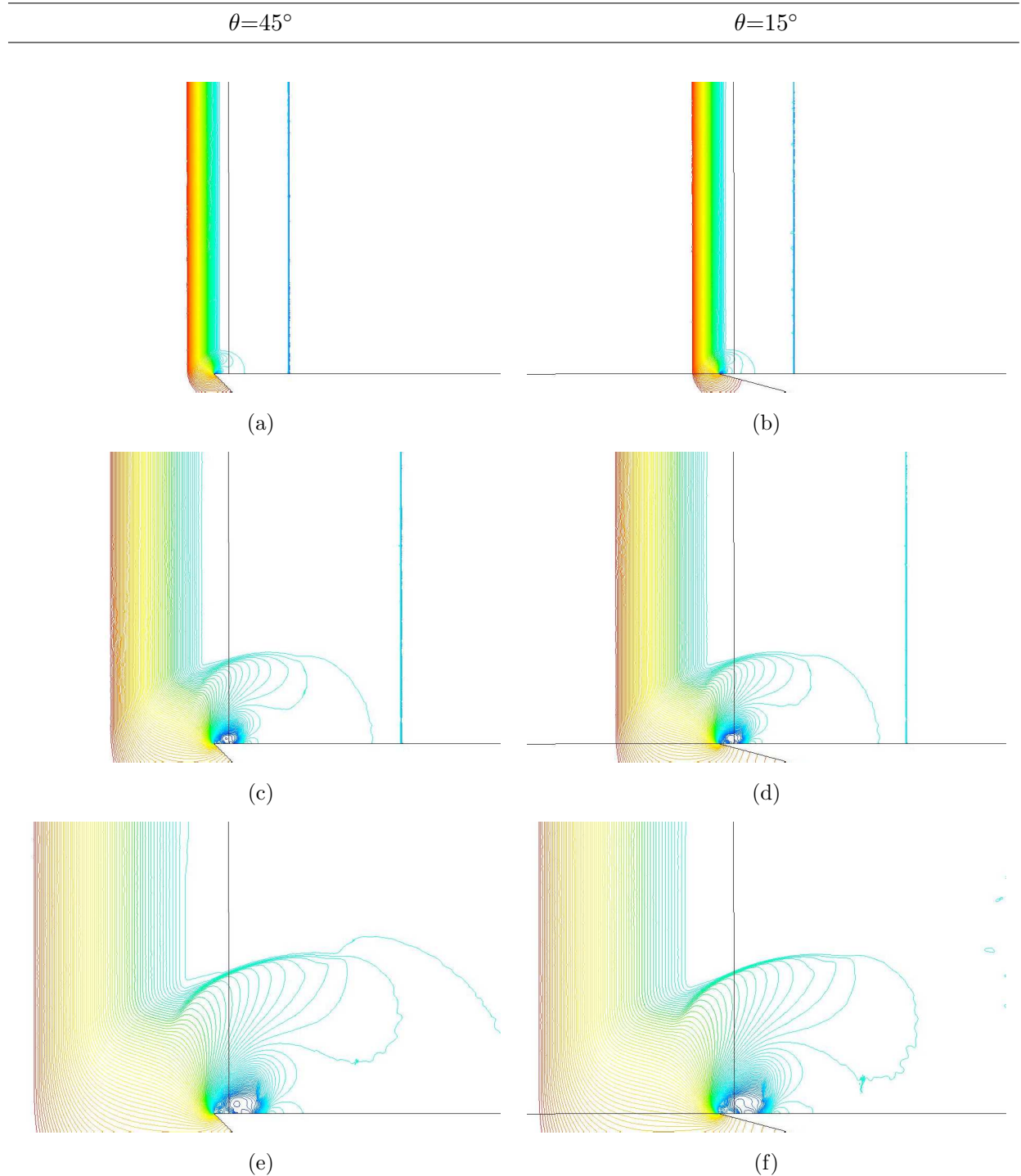


Figure 5.2: Pressure contours for $\theta = 45^\circ$ and $\theta = 15^\circ$ at $PR = 6$ and $D = 10\text{mm}$ (a,b) = $50 \mu\text{s}$ (c,d) = $200 \mu\text{s}$ (e,f) = $350 \mu\text{s}$

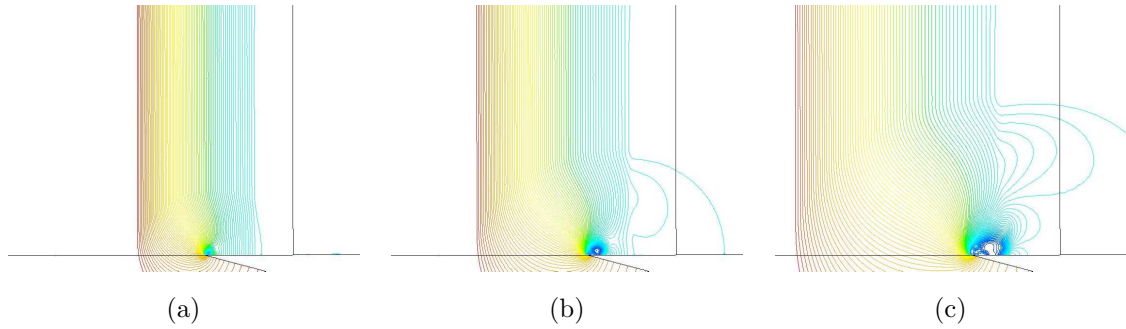


Figure 5.3: Pressure contours for $\theta=15^\circ$ at $PR = 6$ and $D = 70\text{mm}$ (a) = $150 \mu\text{s}$ (b) = $200 \mu\text{s}$ (c) = $350 \mu\text{s}$

5.3 The separation bubble and near corner flow structure

5.3.1 The separation bubble growth

The outer profile of the separation bubble is defined by the shear layer, which develops upon flow separation on the horizontal wall, and its reattachment point downstream of the corner. The profile of the bubble in the previous study of the 90° corner was examined by considering the effects of varying the values of d and P41. It was found that these parameters have a substantial influence on the growth and overall shape of the bubble.

As in previous work, the location of the stagnation point from the corner, henceforth referred to as x_{stag} , was selected as a convenient method to characterise the growth and development of the separation bubble. Figures 4.4 and 4.5 show the progression of the stagnation point with time for $d = 10 \text{ mm}$ and 40 mm at $P41 = 3, 6$ and 9 . The time was non-dimensionalised by the maximum propagation time, taken as $800 \mu\text{s}$. The plots show that the growth of the separation bubble is somewhat linear with time. The density plots in Figures 4.7 and 4.8 show the large reduction in the size of the bubble as d is increased. Also, in agreement with the observations for the 90° corner, the effect of increasing d was to reduce the dependence of x_{stag} and the bubble size on P41.

The effect of varying the corner angle on x_{stag} was then considered in Figure 4.6. The plot shows that for $\theta = 5^\circ$ to 45° the size of the bubble is largely independent of the diffraction corner angle.

The density plots in Figures 4.7 and 4.8 show the results for $P41 = 3$ and 9 at a 15° corner angle. For $P41 = 3$, the separation bubble has a rounder shape for all values of d and was seen to retain this shape throughout the diffraction process. However, at higher values of P41 the bubble is seen to develop a more elliptic shape as time progresses. The bubble's shape

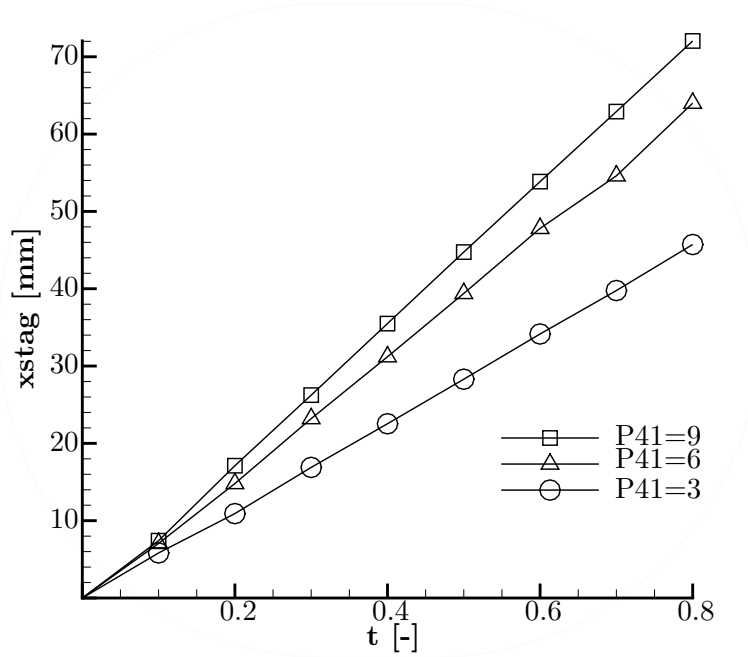


Figure 5.4: Variation of the stagnation point distance from the corner x_{stag} with non dimensional time for $d = 10$ at $P41 = 3, 6$ and 9

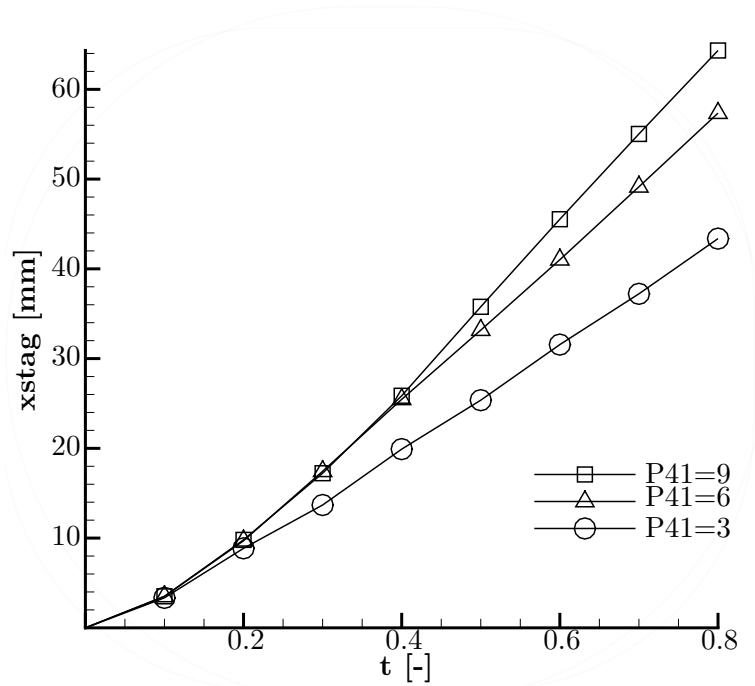


Figure 5.5: Variation of the stagnation point distance from the corner x_{stag} with non dimensional time for $d = 40$ at $P41 = 3, 6$ and 9

elongates at much earlier times for lower values of d . Still, for both $PR = 3$ and 9 the bubble size is significantly reduced as d is increased. As concluded in the analysis of the 90° case,

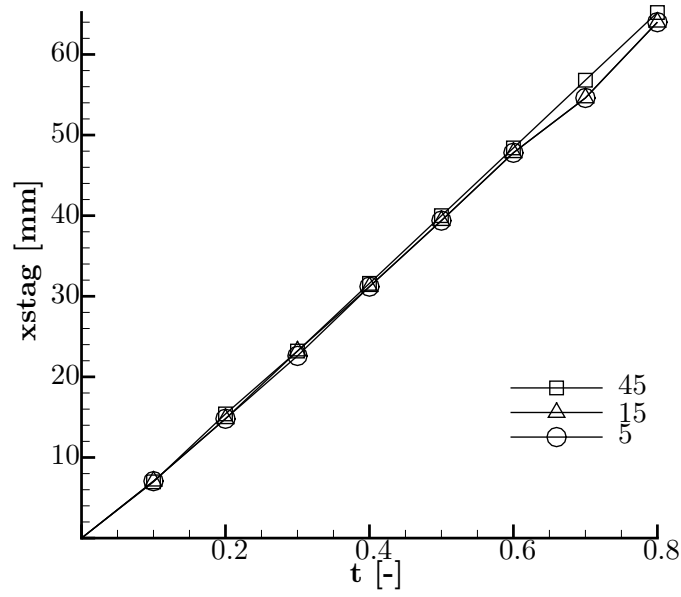


Figure 5.6: Variation of the stagnation point distance from the corner x_{stag} with non dimensional time at $\theta = 5^\circ, 15^\circ$ and 45°

this indicates that the strength of the incident expansion wave has a large effect on the size of the separation bubble.

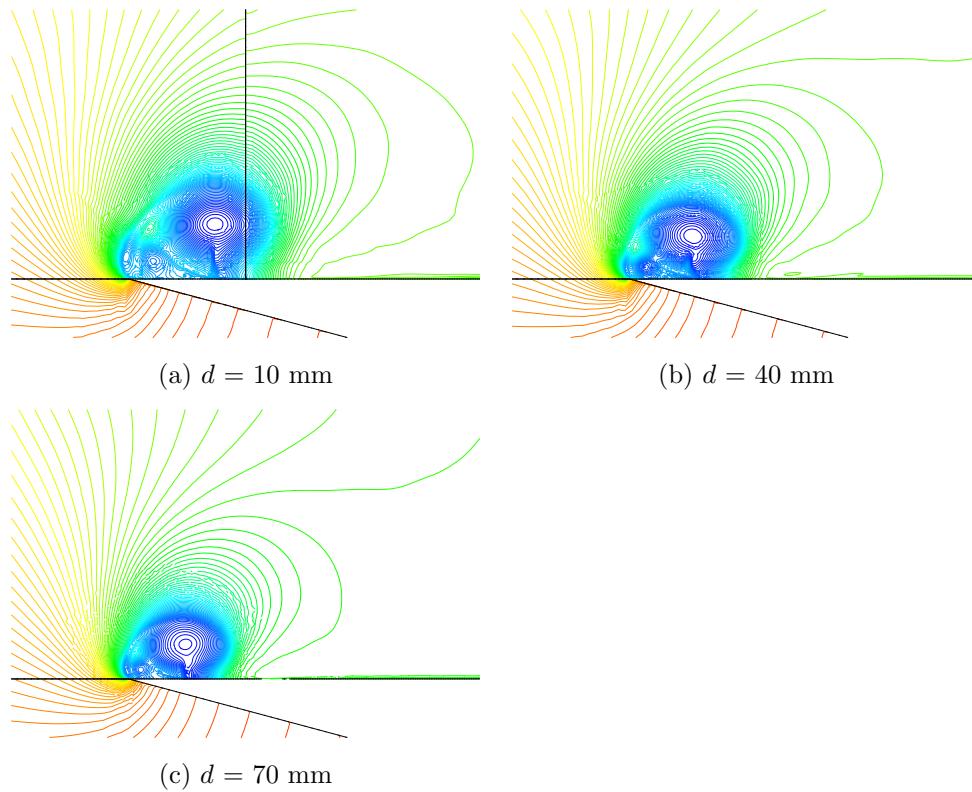


Figure 5.7: Density contour plots for $\theta=15^\circ$ and $P41 = 3$ at $t = 200\mu s$

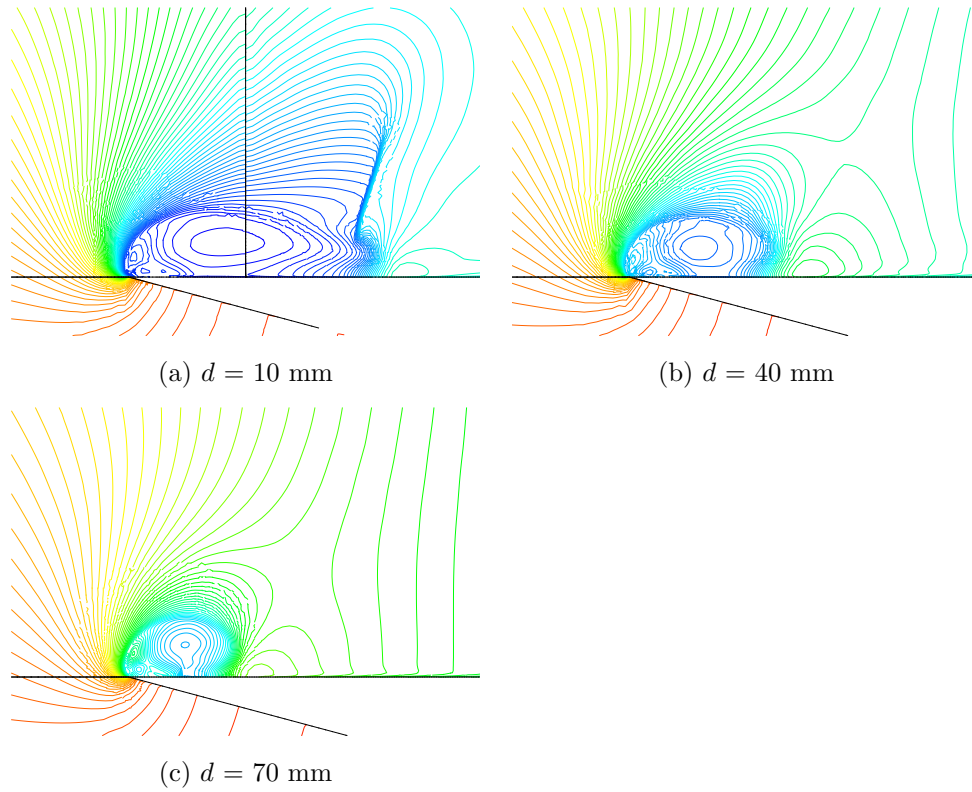


Figure 5.8: Density contour plots for $\theta=15^\circ$ and $P41 = 9$ at $t = 200\mu s$

A comparison considering the variation in θ for $d = 10$ mm is shown in Figures 4.7 and 4.8. Changing the wedge angle between 5° and 45° has only a slight effect on the density distribution within the bubble. However, between the wedge cases and the 90° corner the bubble differs vastly in both size and shape. In the wedge cases the direction that the angled wall imposes on the flow moving around the corner results in a more heightened bubble and, as such, a rounder profile. This effect is seen for both $P41 = 3$ and 9 and at higher d values, illustrated in Figures 4.11 and 4.12 for $d = 70$ mm.

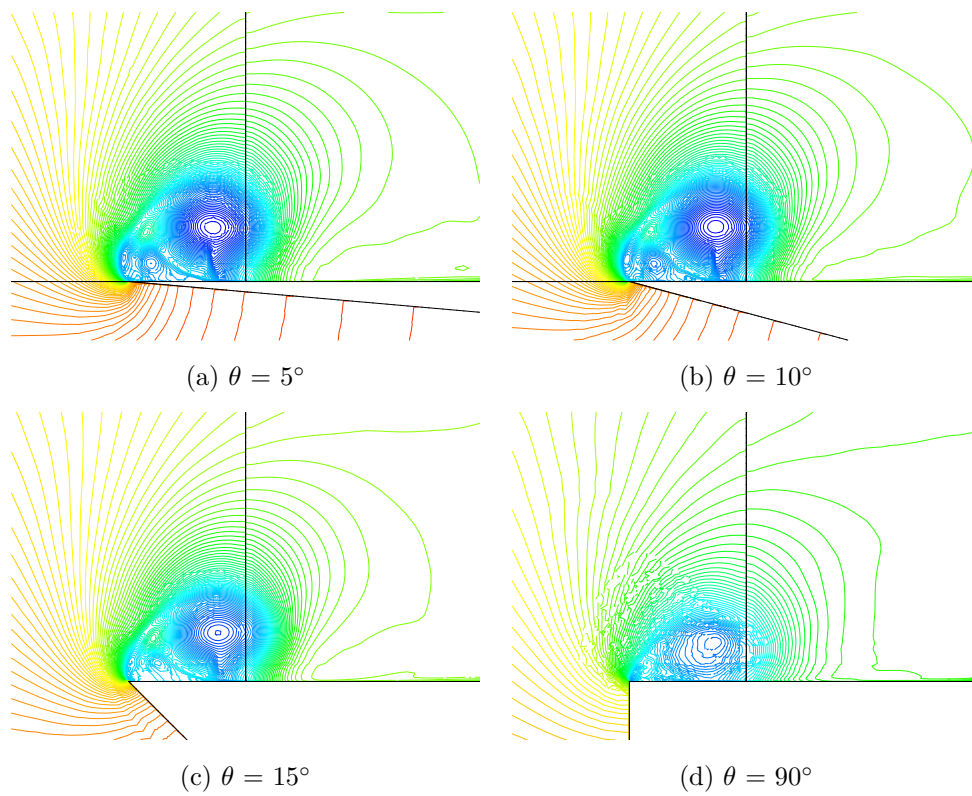


Figure 5.9: Density contour plots for $d = 10$ mm and $P41 = 3$ at $t = 200\mu s$

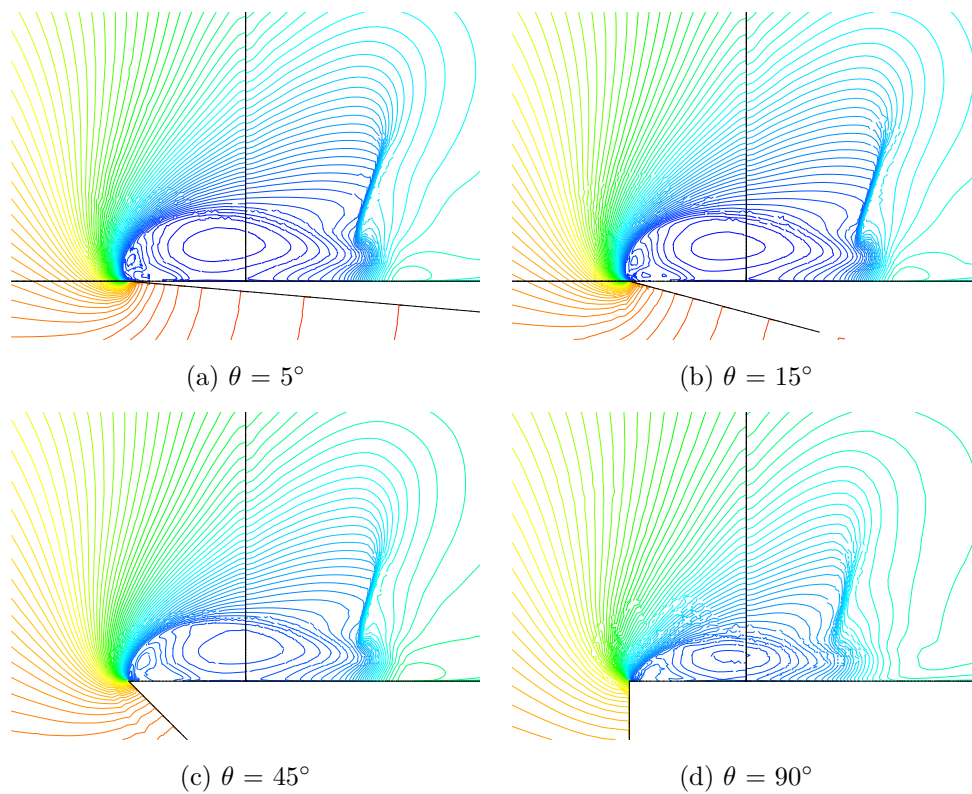


Figure 5.10: Density contour plots for $d = 10$ mm and $P41 = 9$ at $t=200\mu s$

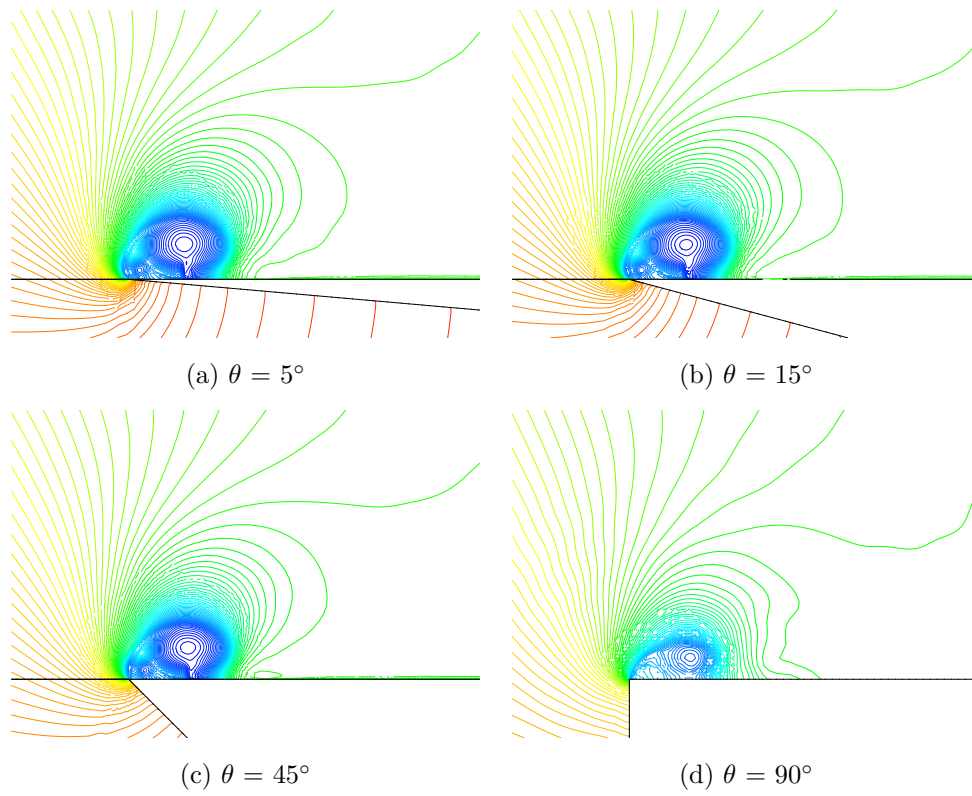


Figure 5.11: Density contour plots for $d = 70$ mm and $P41 = 3$ at $t = 200 \mu s$

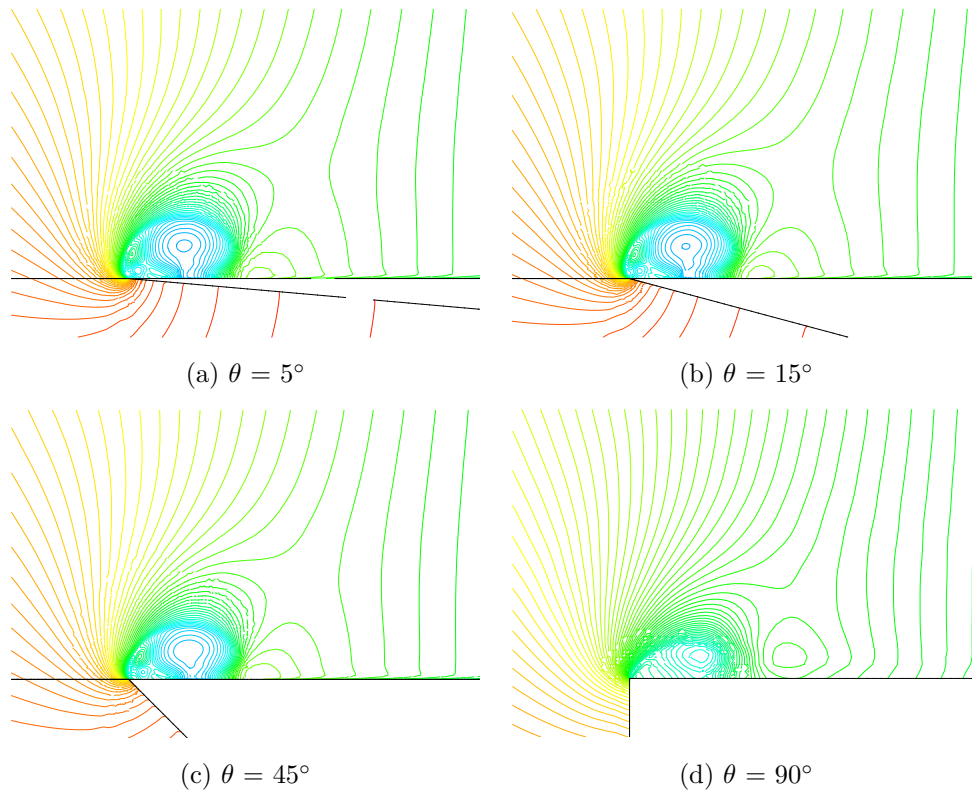


Figure 5.12: Density contour plots for $d = 70$ mm and $P41 = 9$ at $t = 200 \mu s$

5.3.2 Near corner velocity gradients and viscous vortices

In the study on the 90° corner it was observed that the boundary layer would separate at the apex of the corner. For shock diffraction it is known that upon separation the boundary rolls up into a viscous vortex. However, for expansion wave diffraction the shear layer was seen to reattach at some distance along the horizontal wall forming a separation bubble (the *primary separation bubble*). This bubble was observed to contain a large viscous vortex with a turbulent vortex core.

A second separation was observed to occur along the horizontal wall, within the primary separation bubble. The second separation initiated a second smaller separation bubble near the diffraction corner which was contained within the primary bubble. A secondary viscous vortex is found within the smaller bubble. Figure 4.13 illustrates the circulatory fluid within the separation bubble at $\theta = 45^\circ$. A number of mini vortices were observed in the separation bubble near the diffraction corner for both the 90° and the wedge corners. In certain cases a shock was seen to develop along the wall preceding the second separation point. This was called the re-compression shock and is discussed further in Section 4.3.4.

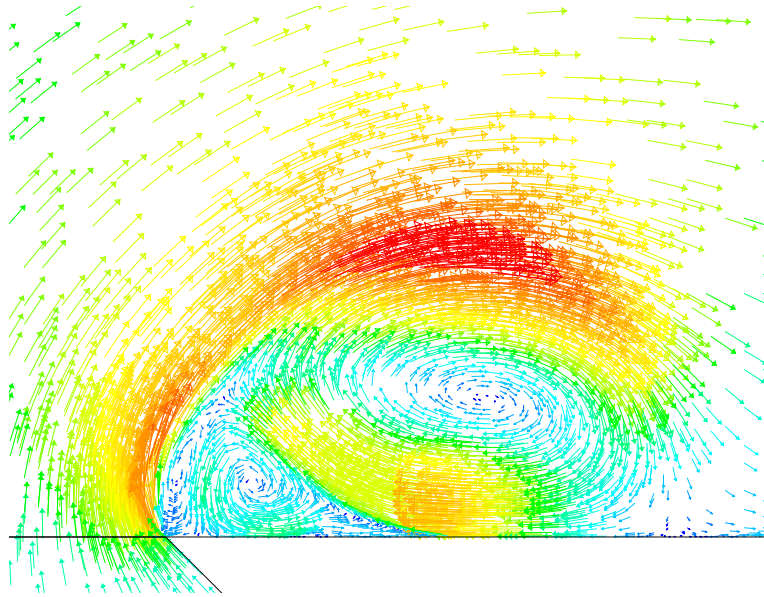


Figure 5.13: Vector velocity plot indicating primary and secondary vortices

A comparison between the experimental schlieren images and the velocity magnitude vector plots at $\theta = 45^\circ$ and $d = 55$ mm are given in Figure 4.14. The vector plots illustrate very steep velocity gradient at the diffraction corner. This gradient is found to be significantly higher than was observed with the 90° corner. A comparison in the flow velocity for the 90° corner and wedge case for $\theta = 5^\circ$ is shown in 4.15. Using a horizontal knife-edge for the

schlieren setup the sharp gradient off the diffraction corner could be visualised experimentally as shown in the images. In both the

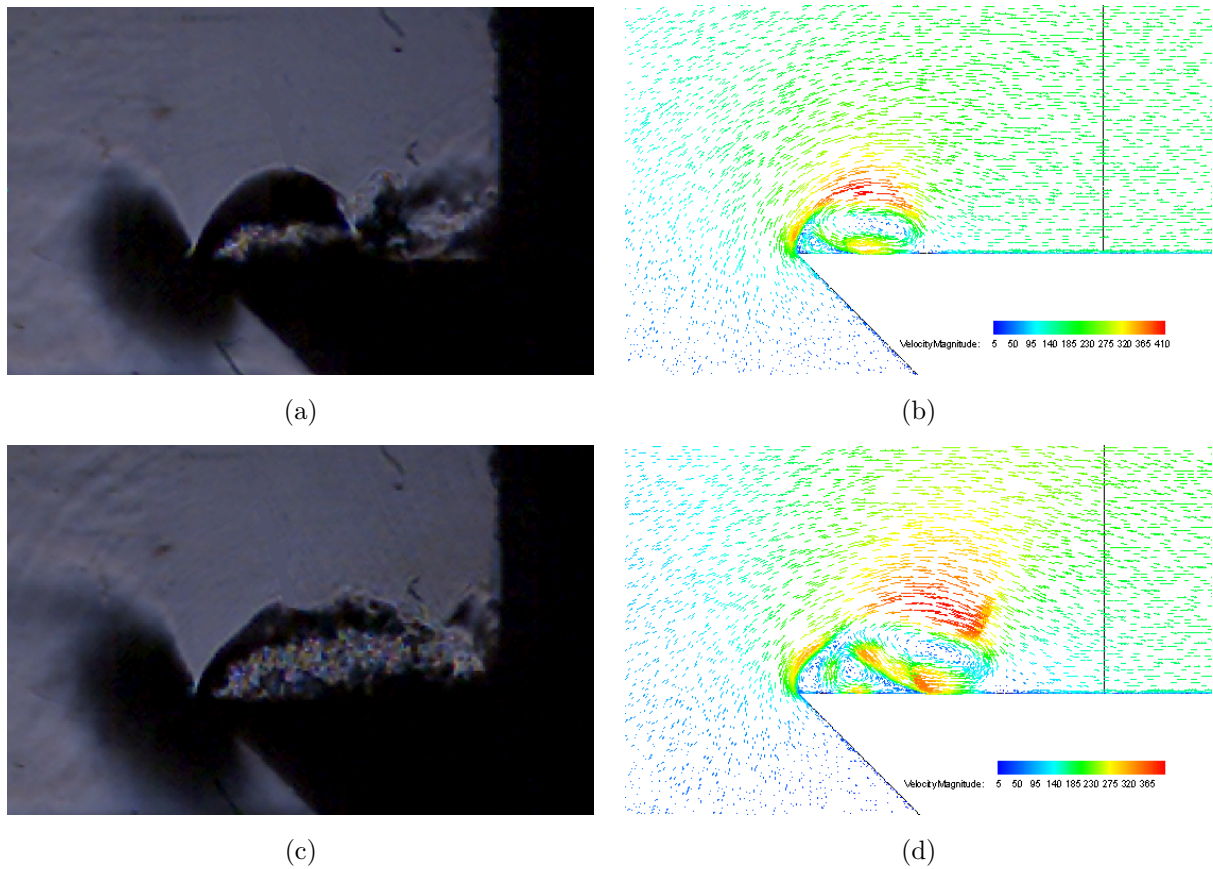


Figure 5.14: Schlieren (horizontal knife-edge) and velocity magnitude vector plot comparison. $\theta = 45^\circ$, $d = 55$ mm. (a, b) $405 \mu\text{s}$, (c, d) $740 \mu\text{s}$

Ignoring the large difference in the structure of the bubble (which was looked at in the previous section) for the 5° and 90° corners in Figure 4.15, at this early time delay of $200 \mu\text{s}$ both the primary and secondary vortices are fully formed for $\theta = 5^\circ$. For the 90° case the secondary vortex has not yet formed. The flow has only just separated and the inception of the shear layer is seen. The vector plots in Figure 4.16 show the near corner flow structure at a later time of $600 \mu\text{s}$. At this stage we see the development of two equally sized counter rotating vortices in the secondary separation bubble for the 90° corner. This is substantially different to the 5° corner where one large secondary vortex is present. In this case the second counter-rotating vortex forms in an oblong shape between the first secondary vortex and the shear layer forming the bubble. The circulatory flow follows a path governed by the profile at the front end of the bubble.

The plots in Figure 4.19 illustrate the viscous vortices in the separation bubble for $\theta = 45^\circ$, 15° and 5° . Hardly any difference can be noted in the vortex formation as the corner angle is altered. Upon closer inspection, however, it is noted that the secondary vortex follows

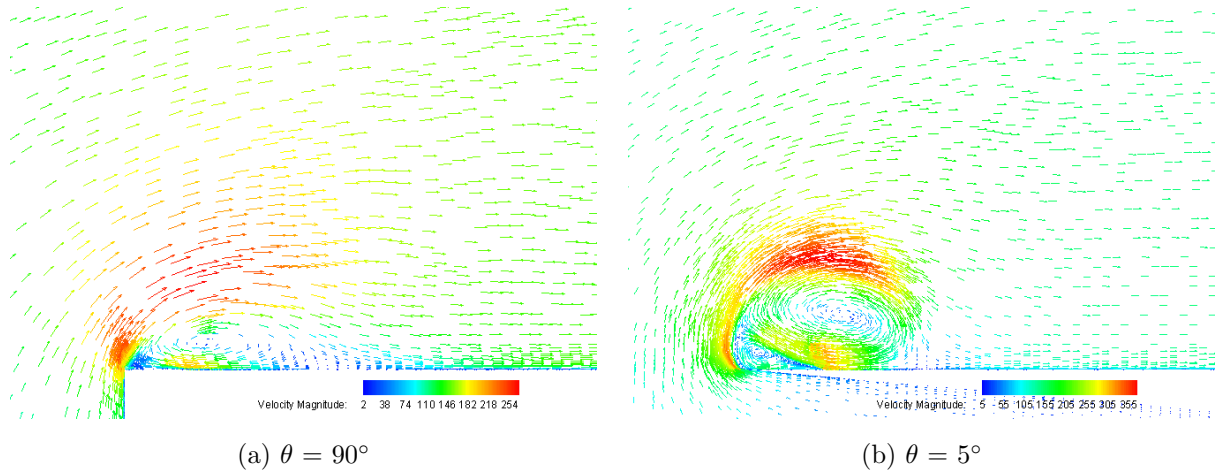


Figure 5.15: Velocity magnitude vector plots. $P41 = 3$, $d = 40$ mm and $t = 200 \mu s$

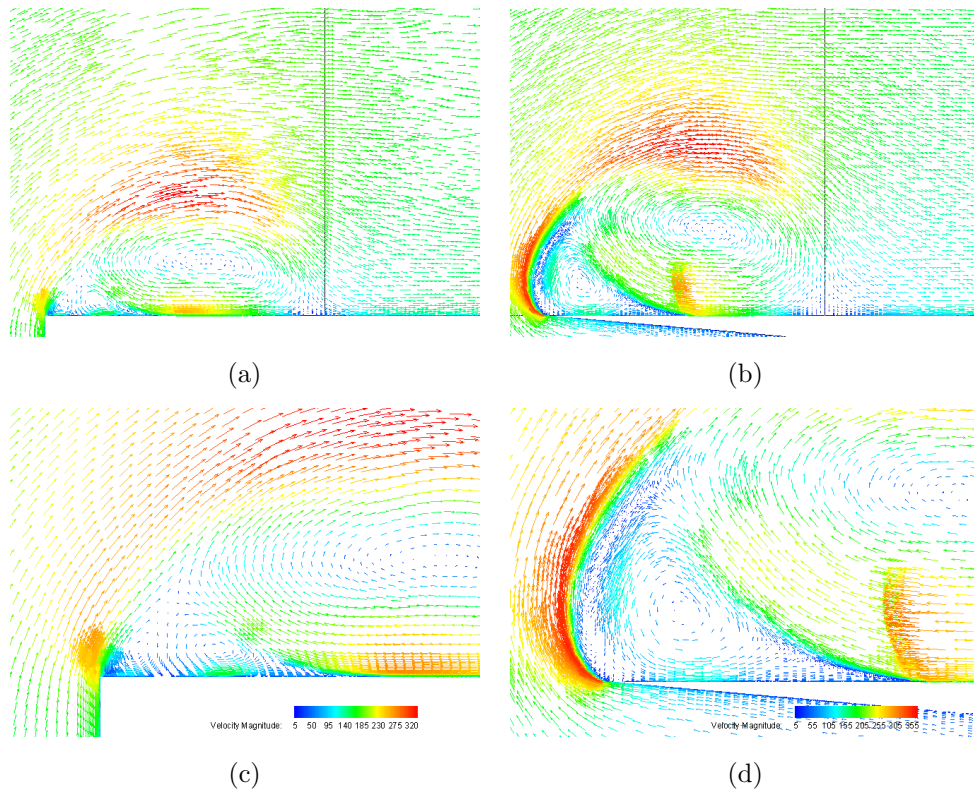


Figure 5.16: Velocity magnitude vector plots. $\theta = 5^\circ$, $P41 = 3$, $d = 40$ mm and $t = 600 \mu s$. Images illustrating the near-corner region are provided in figures (c) and (d)

a more 'triangular' profile as the angle is reduced due to the impression of the secondary vortex. This is shown more closely in Figure 4.18

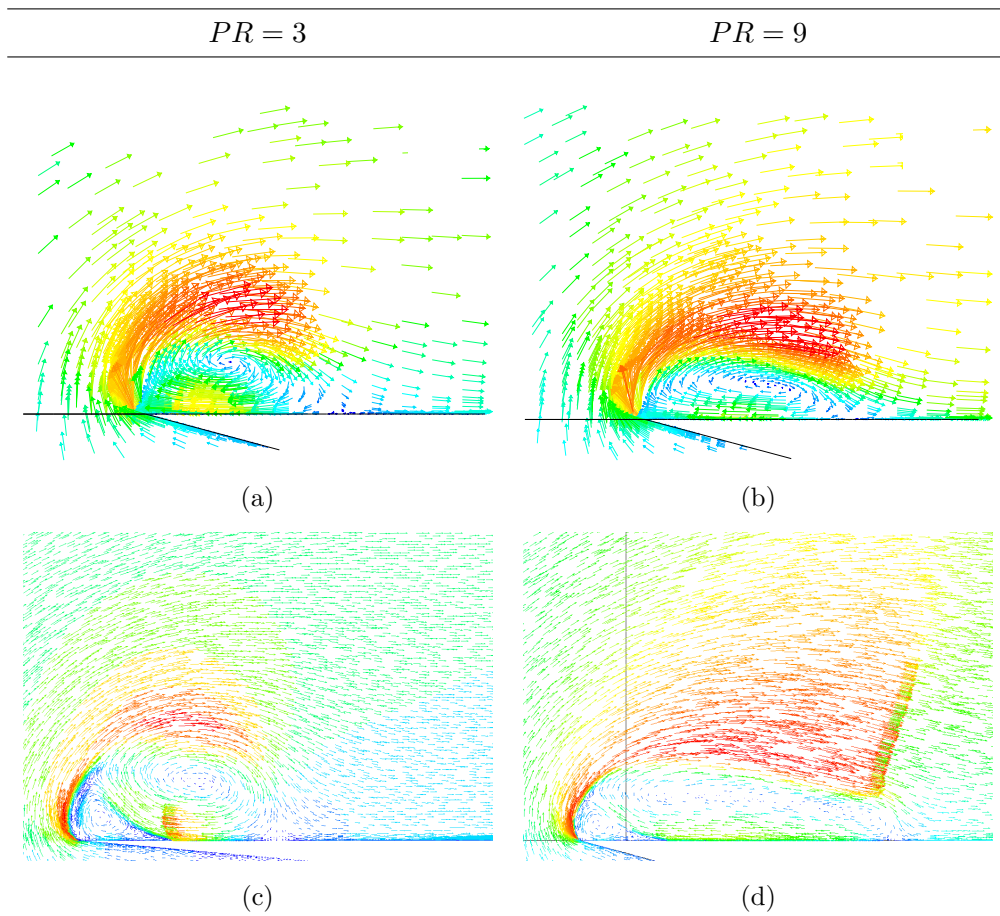


Figure 5.17: Velocity magnitude vector plots at $\theta = 15^\circ$, $P41 = 3$ and 9 at $d = 10$ mm (a, b) $50 \mu s$ (c, d) $600 \mu s$ (a, b and c, d not to the same scale)

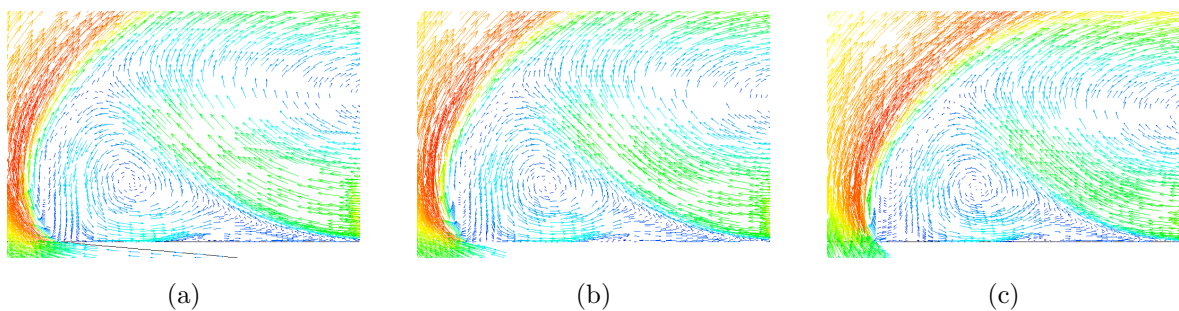


Figure 5.18: Velocity magnitude vector plots. $P41 = 6$, $d = 70$ mm and $t = 300 \mu s$ (a) $= 45^\circ$ (b) $= 15^\circ$ (c) $= 5^\circ$

$t = 200 \mu s$

$t = 500 \mu s$

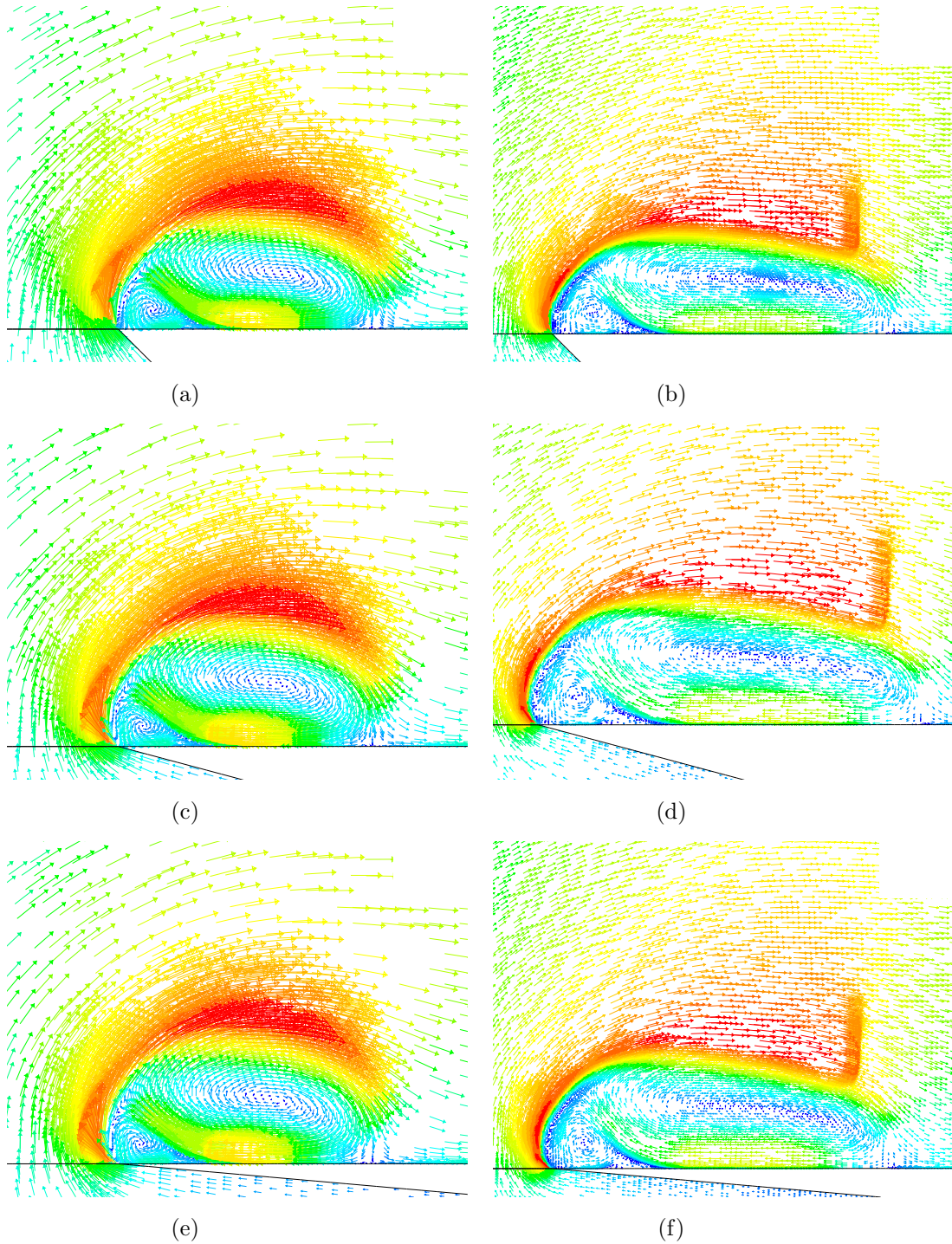


Figure 5.19: Velocity magnitude vector plots for $P41 = 6$ and $d = 70$ mm (a, b) $\theta = 45^\circ$ (c, d) $\theta = 15^\circ$ (e, f) $\theta = 5^\circ$

5.3.3 Oblique shock and supersonic region

The profile of the separation bubble was found to have a significant impact on the nearby flow field. The bubble's curvature had resulted in flow acceleration around the bubble and a consequent reduction in pressure towards the top of the bubble. In order for the flow to then meet downstream conditions an oblique shock, which was briefly discussed in Section 1.2, had developed to the rear end on the bubble. In the 90° analysis the shock was identified as an oblique type firstly due to the post-shock flow not being subsonic. The shock was found to be contained within an enclosed region of supersonic flow (termed the supersonic region). Secondly, the post-shock flow was at a finite angle to the shock while the incoming flow was close to normal. The supersonic region, which enclosed the oblique shock and compression fan, would develop at different flow times depending on the flow conditions.

5.3.3.1 Evolution of the supersonic region

In the 90° analysis the following observations were made for the results at $P41 = 3$:

- The supersonic region would develop early for lower values of d (around $t = 300 \mu s$ for $d = 10$ mm) and later on for $d = 40$ mm or 70 mm.
- At later simulation times the supersonic region and the bubble seemed similar in shape and size for all values of d .
- At later times a second supersonic region was seen to develop within the separation bubble.

These observations differed somewhat in what was found for the wedge cases. Figure 4.20 and 4.22 show the results for $\theta = 15^\circ$ and $\theta = 45^\circ$ at $t = 200 \mu s$ and $350 \mu s$. The supersonic region is evident for both values of d at an early time of $200 \mu s$. For $d = 10$ mm the supersonic region was seen to develop as early as $50 \mu s$. In all the cases the second supersonic region within the bubble is noticeable.

In the 90° case it was found that for $P41 = 6$ and 9 the supersonic region developed much earlier than at $P41 = 3$. The region had developed at $t = 100 \mu s$ for $d = 10$ mm for both $P41 = 6$ and 9 and at $t = 200 \mu s$ for $P41 = 40$ mm. For the wedge cases the supersonic region was found to develop as early as $115 \mu s$ for $d = 40$ mm.

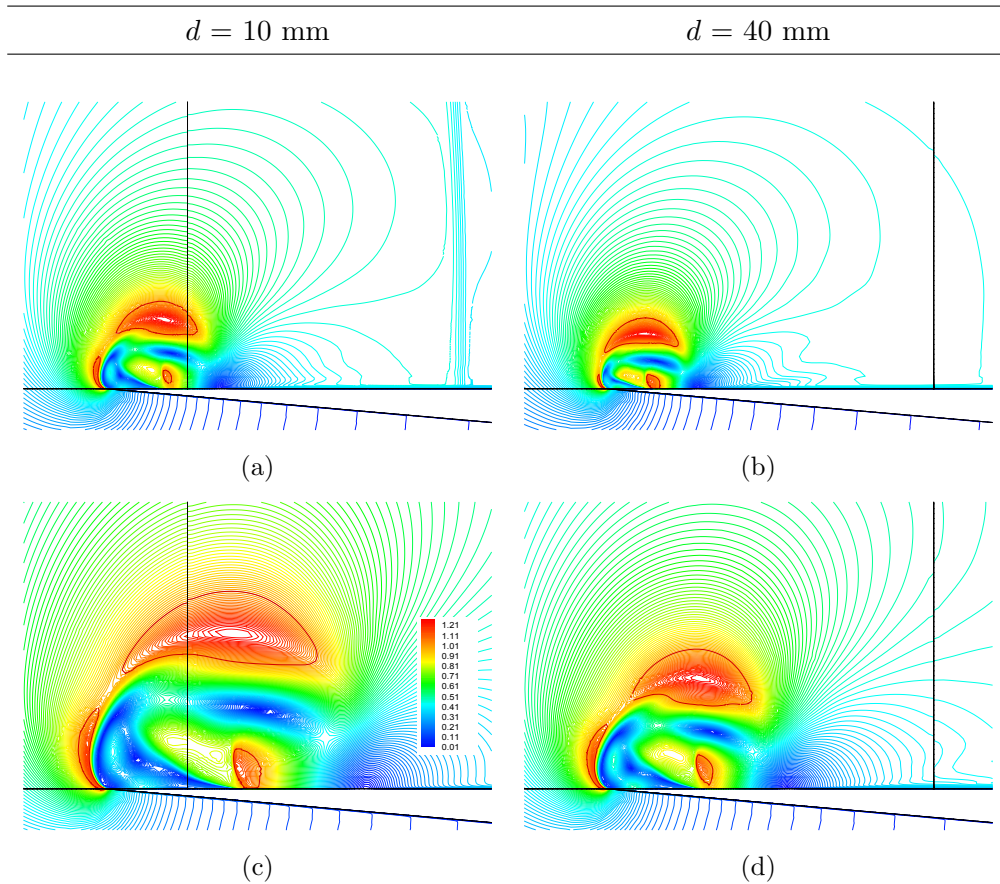


Figure 5.20: Mach number contour plots for $\theta = 5^\circ$ and $P41 = 3$ at (a, b) $t = 200 \mu\text{s}$ (c, d) $t = 350 \mu\text{s}$

5.3.3.2 Behaviour of the Oblique shock

The behaviour of the oblique shock with respect to the parameters θ , d and $P41$ are now considered. The contours in Figures 4.23 and 4.24 display the results at $P41 = 6$ and 9 and $\theta = 15^\circ$ at $t = 600 \mu\text{s}$. The results differed in comparison with the 90° case where for $P41 = 6$ the oblique shock had not yet developed at $600 \mu\text{s}$ for $d = 10 \text{ mm}$ and 40 mm and was only noted for $d = 70 \text{ mm}$ at this time. In the wedge cases however, the shock was evident for all values of d at $t = 600 \mu\text{s}$. The shock's early development in the wedge scenarios could most probably be attributed to the increased bubble curvature discussed previously in Section 4.3.3.

Figures 4.24 and 4.25 show a comparison between the results for $\theta = 15^\circ$ and $\theta = 45^\circ$ at $P41 = 9$ and $t = 600 \mu\text{s}$. The results show a large independence on θ with regards to the shock structure and development of the supersonic region. A difference exists in the profile of the supersonic region where it turns in much closer to the oblique shock especially at lower d . The region seems to approach the shock as the corner angle is reduced.

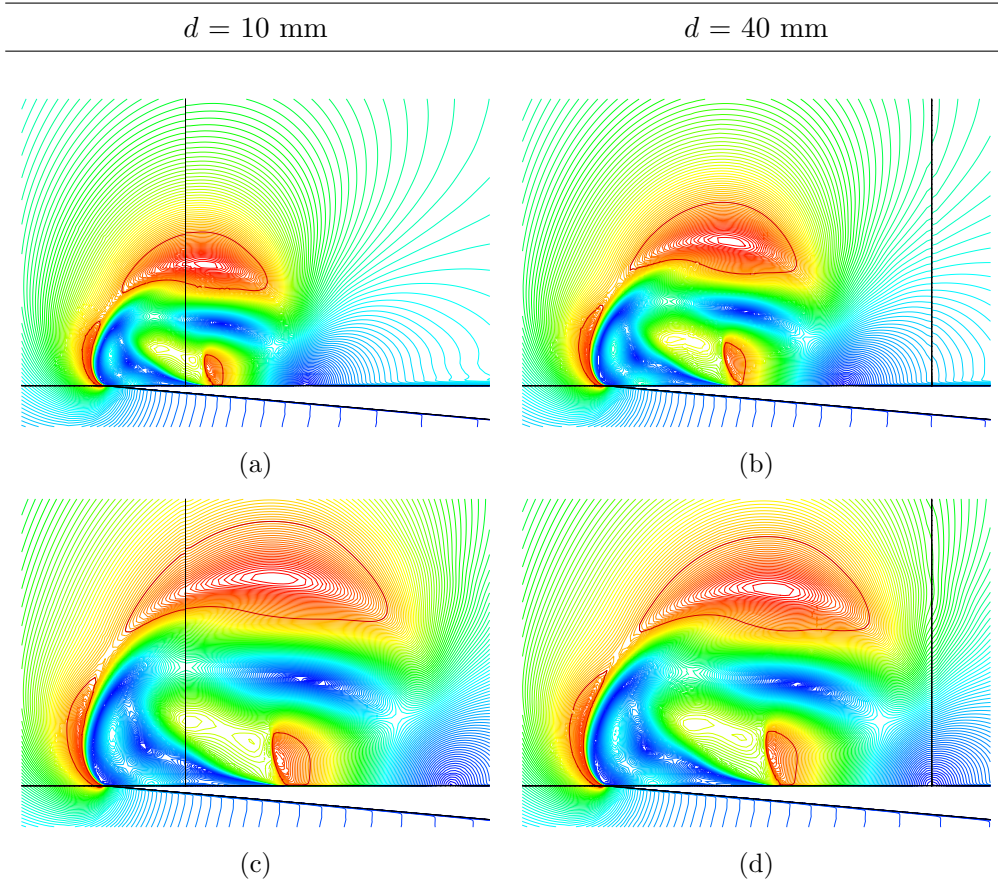


Figure 5.21: Mach number contour plots for $\theta = 5^\circ$ and $P41 = 3$ at (a, b) $t = 450 \mu\text{s}$ (c, d) $t = 600 \mu\text{s}$

5.3.4 Recompression shock

In the results for $P41 = 3$ a second supersonic region was noted within the separation bubble along the horizontal wall. A similar observation was made for the 90° case where it was noted that the region would terminate in a shock, which was termed the re-compression shock, similar to that observed in the case of shock diffraction. For the 90° corner the re-compression shock was only found for the case of $d = 0 \text{ mm}$ and $P41 = 3$. In the current study of the wedge cases it was found that the presence of the shock was not limited to $d = 0$ but was found at all values of d , clearly visible in Figure 4.20.

A second separation point was noted within the separation bubble. The primary vortex within the separation bubble induced a separation of the supersonic flow along the horizontal wall. For the 90° corner the flow was seen to separate within the bubble for $d = 0, 10$ and 40 mm but not for $d = 70 \text{ mm}$. For the angled wall cases flow separation was observed for all values of d . The re-compression shock would serve the purpose of transitioning the flow to subsonic speeds to allow separation to occur.

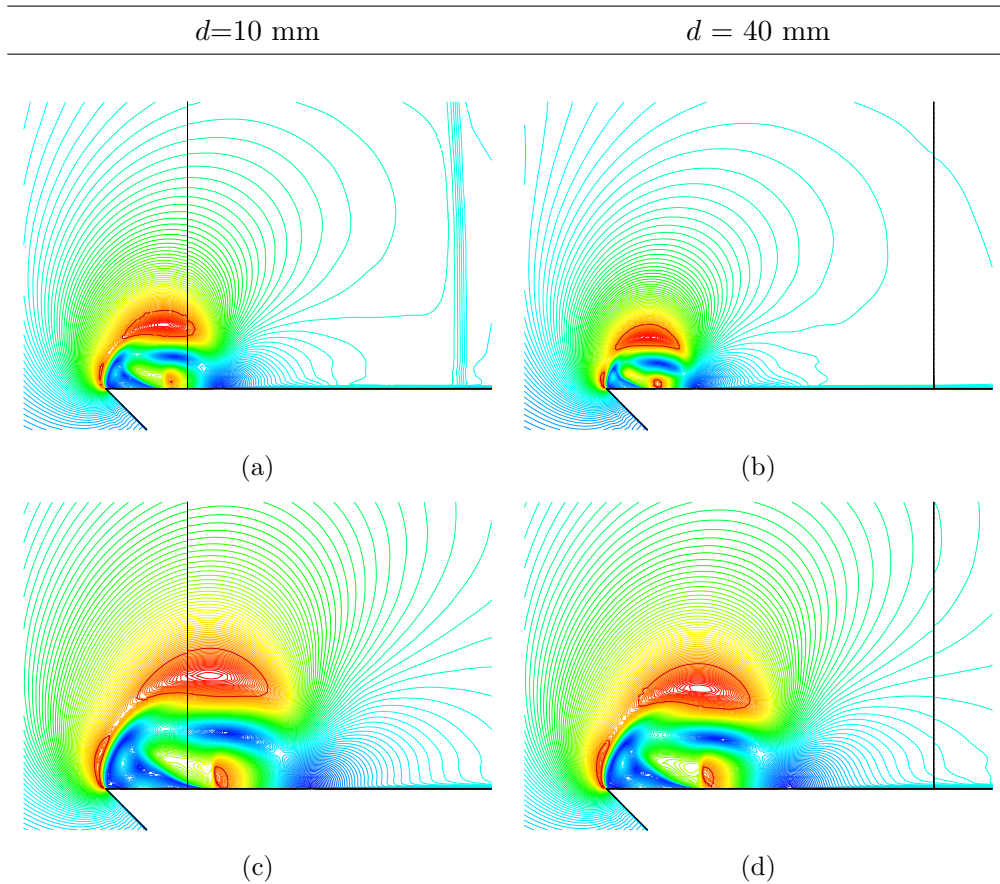


Figure 5.22: Mach number contour plots for $\theta = 45^\circ$ and $P41 = 3$ at (a, b) $t = 200 \mu\text{s}$ (c, d) $t = 350 \mu\text{s}$

The re-compression shock for the wedge cases appeared to be of higher strength and extended higher into the separation bubble than what was observed for the 90° corner. The strength and size of the shock is seen to increase as the wedge angle is reduced. A comparison between the shock structure for $\theta = 45^\circ$ and $\theta = 5^\circ$ is given in Figure 4.27. The vector velocity plots illustrating the supersonic region and separation within the bubble for $d = 10$ mm and 70 mm at $\theta = 5^\circ$ are given in Figure 4.28. Due to the non-slip condition prevalent at the wall, supersonic flow along the horizontal wall would imply extremely high wall-normal velocity gradients [4] where the supersonic region is located. As with the 90° corner, a secondary shear layer had developed at the second separation point which does not reattach along the wall but feeds into the smaller vortices at the diffraction corner. The density plot in Figure 4.26 shows a close-up illustration of the boundary layer separation and secondary shear layer formation.

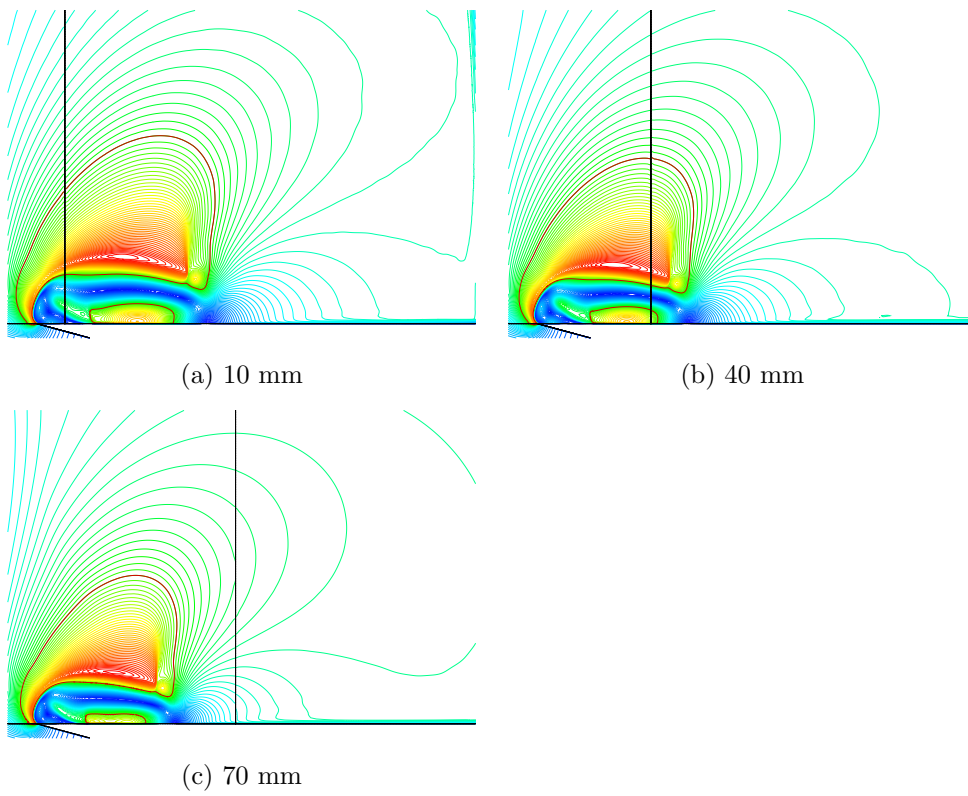


Figure 5.23: Mach number contour plots for $\theta = 15^\circ$ and $P41 = 6$ at $t = 600 \mu s$

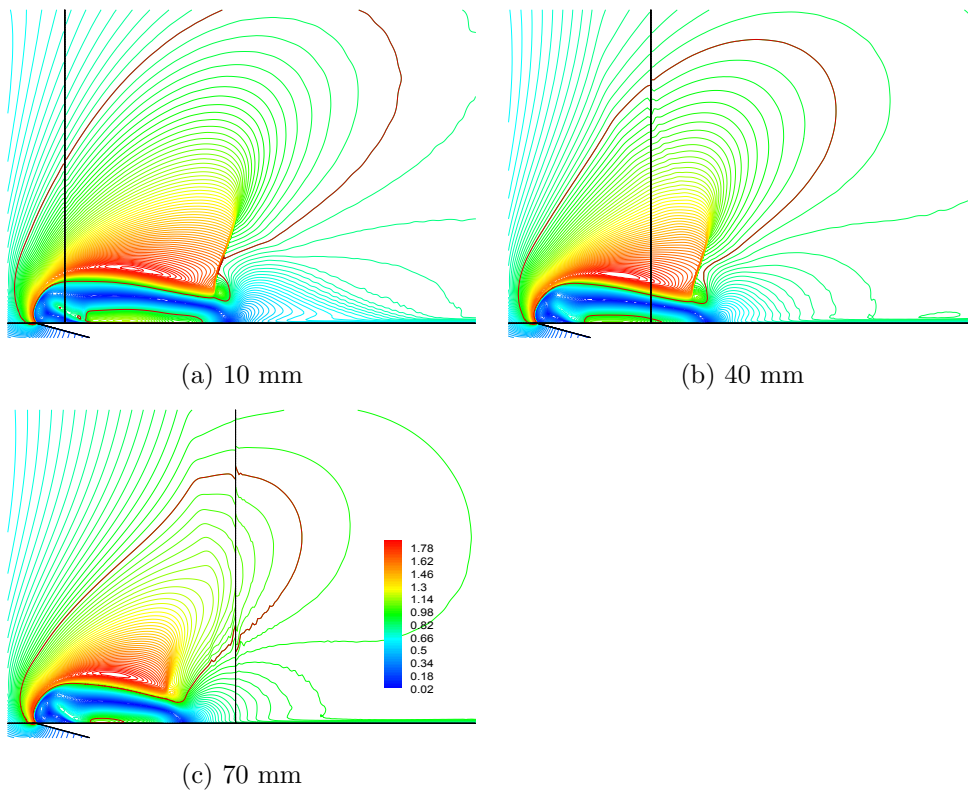


Figure 5.24: Mach number contour plots for $\theta = 15^\circ$ and $P41 = 9$ at $t = 600 \mu s$

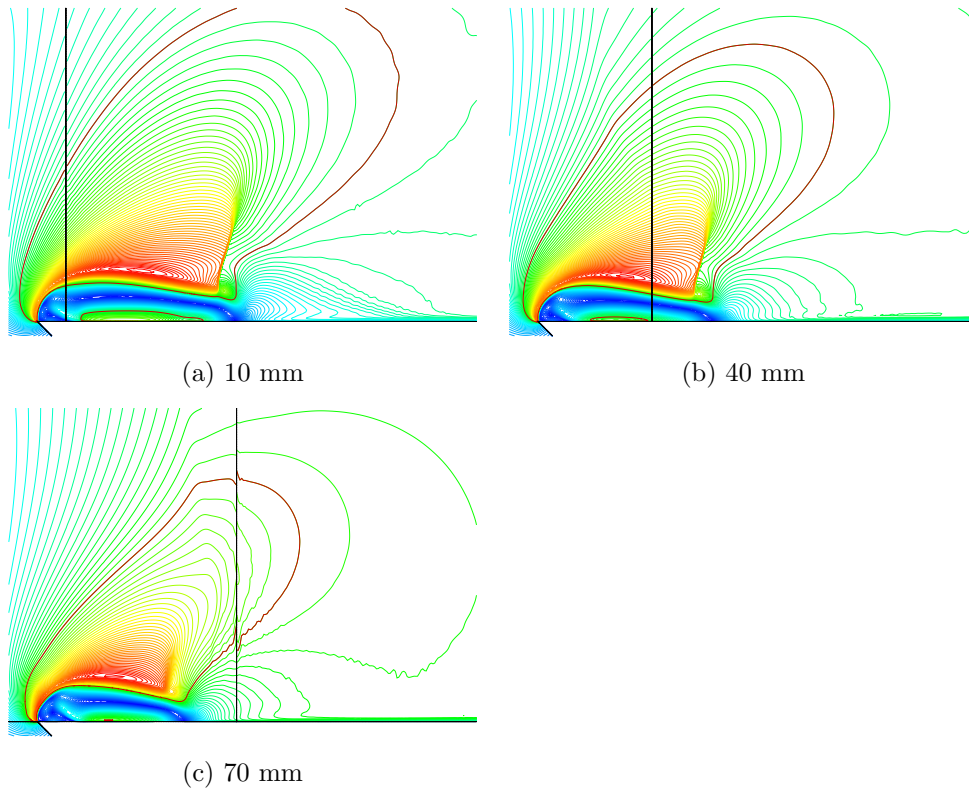


Figure 5.25: Mach number contour plots for $\theta = 45^\circ$ and $P41 = 9$ at $t = 600 \mu s$

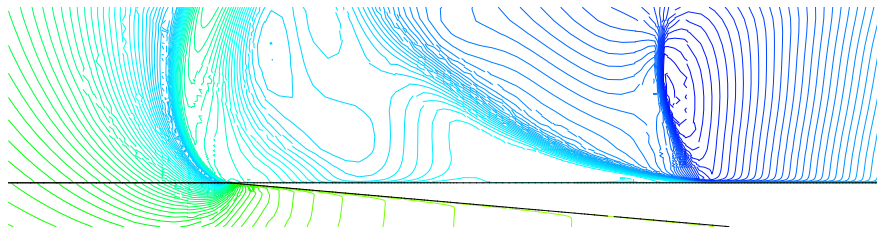
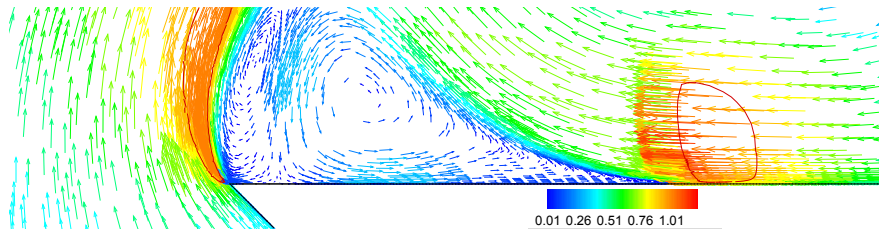
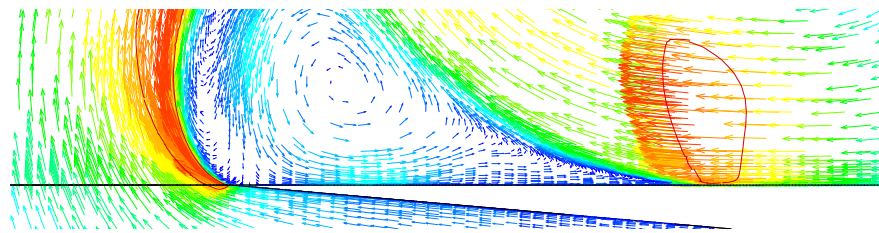


Figure 5.26: Density contour plot illustrating the compression shock, boundary layer separation and secondary shear layer. $\theta = 5^\circ$, $P41 = 3$, $d = 40 \text{ mm}$ and $t = 600 \mu s$

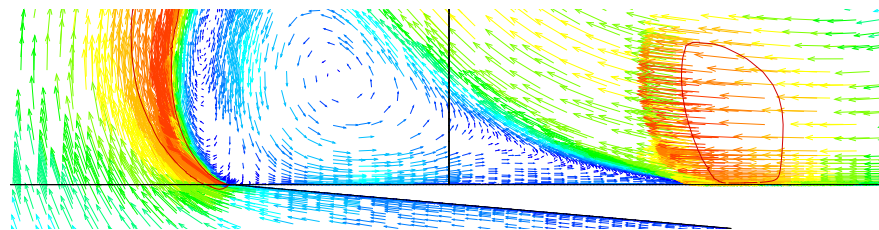


(a)

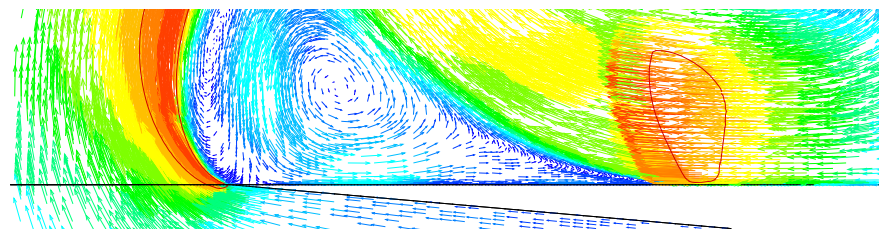


(b)

Figure 5.27: Mach number contour plots. $P41 = 3$, $d = 40$ mm $t = 600 \mu\text{s}$ (a) $\theta = 45^\circ$ (b) $\theta = 5^\circ$

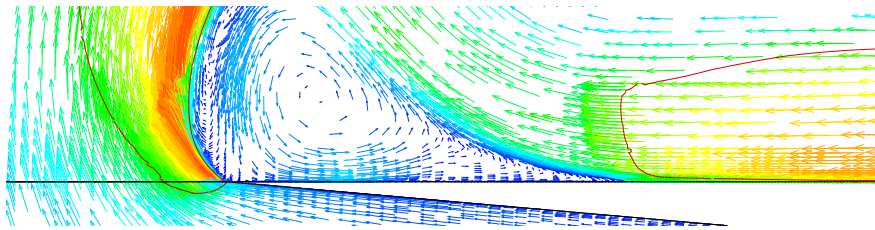


(a)

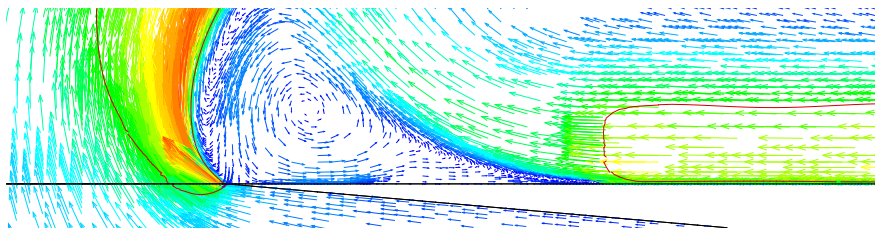


(b)

Figure 5.28: Mach number contour plots. $\theta = 5^\circ$, $P41 = 3$ and $t = 600 \mu\text{s}$ (a) $d = 10$ mm (b) $d = 40$ mm



(a)



(b)

Figure 5.29: Mach number contour plots. $\theta = 5^\circ$, $P41 = 6$ and $t = 600 \mu\text{s}$ (a) $d = 10$ mm
(b) $d = 40$ mm

5.4 Trailing sonic and supersonic flow

The analysis now considers the case where the flow following the expansion wave is not subsonic ($M_f \geq 1$). From previous discussions (1.5.1), as the flow is able to accelerate to sonic conditions at an initial diaphragm pressure ratio of 10.4, supersonic trailing flow would occur for values of $P_{41} > 10.4$. Reported results consider $P_{41} = 15$.

Earlier discussions showed that the main effect of increasing P_{41} above 10.4 is the movement of the incident expansion wave's trailing characteristic. It was shown that the trailing characteristic would propagate downstream until $P_{41} = 10.4$ where it would remain stationary. Beyond this the trailing characteristic would start running right. In the plot in Figure 4.30, the solid red line (indicating sonic conditions) show that the diaphragm forms a partial boundary for the supersonic region. Between the sonic and trailing characteristics the wave would run downstream.

5.4.1 Comparison between flow features for $P_{41} < 10.4$ and $P_{41} > 10.4$

For the 90° case it was found that the major flow features remained largely consistent for subsonic and supersonic trailing flow conditions. As with the subsonic trailing flow, the features observed were a reflected compression wave, the oblique shock and supersonic region. Figure 4.31 indicates the separation bubble features for both the subsonic and supersonic trailing cases.

The cases with $P_{41} > 10.4$ however, showed a significant difference in the shock structure. A triple-point was seen to develop in the area of the separation bubble. The oblique shock was also noted to have a much higher curvature than for $P_{41} < 10.4$.

The wedge cases ($\theta < 90^\circ$) showed a similar progression of events to what was observed for the 90° corner. Figures 4.32 and 4.35 depict the flow field at time delay values of $t = 350 \mu s$ and $t = 600 \mu s$ at a corner angle of $\theta = 15^\circ$ with variation in the diaphragm distance. The effect of supersonic trailing flow on the oblique shock, the supersonic region and the reflected compression wave were discussed in the 90° analysis. The primary observations are briefly outlined in this discussion.

5.4.1.1 The Oblique Shock

In contrast to what was observed for $P_{41} < 10.4$ a triple point is seen to develop to the rear of the separation bubble. The oblique shock that developed with supersonic trailing flow had

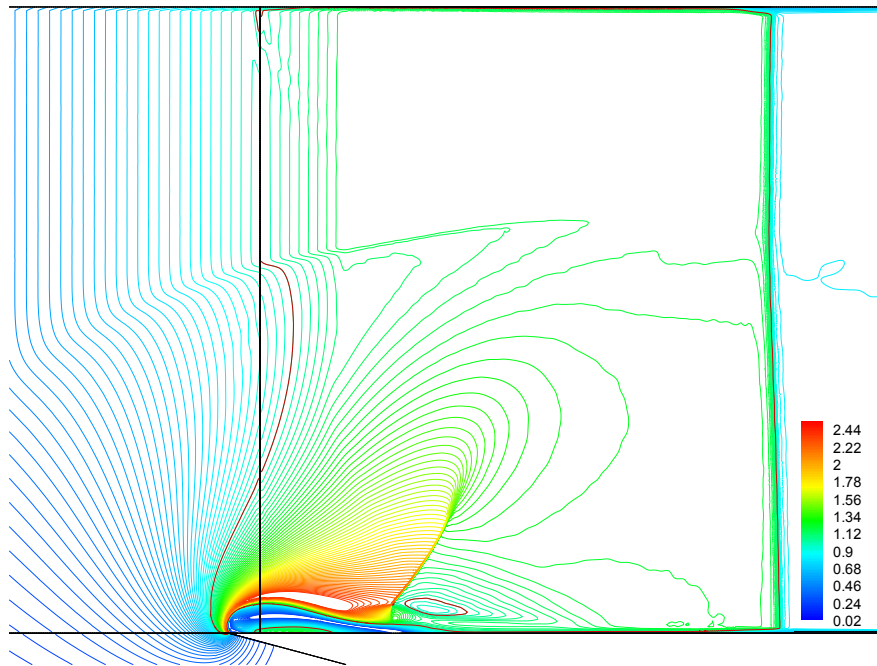


Figure 5.30: Mach number contour on the post diffraction field for $P41 > 10.4$ at $d = 10$ mm, $P41 = 15$ and $t = 400 \mu s$. Mach 1 trace in red.

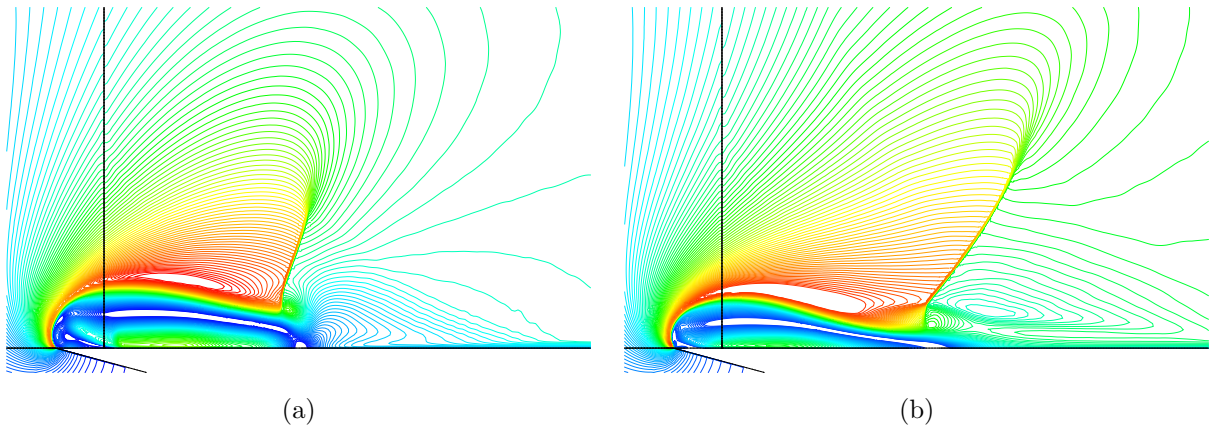


Figure 5.31: Mach number contour plot illustrating the separation bubble for subsonic and supersonic trailing flow at $d = 10$ mm and $t = 450 \mu s$ (a) $P41 = 9$ (b) $P41 = 15$

a much higher curvature than what was observed earlier. With increasing, d , the formation of the oblique shock and the triple point was delayed. Figure 4.35 shows that at $600 \mu s$ the triple point had not yet been developed for $d = 70$ mm. As with the $P41 < 10.4$ cases the delayed shock formation is believed to result due to the bubble having a rounder profile.

5.4.1.2 The Supersonic Region

As highlighted in Figure 4.32, the sonic characteristic remains stationary at the incident expansion waves origin (the diaphragm location). The supersonic region lies between this and the contact surface. For smaller values of d , the separation bubble, oblique shock and cylindrical shock develop within the supersonic region.

5.4.1.3 The Reflected Compression Wave

In a similar manner to what was observed for $P41 < 10.4$ the reflected compression waves converged into a cylindrical shock wave at early times for lower d . For the supersonic case, however, the reflected compression would not propagate radially outward as it did for $P41 < 10.4$ as signals from the reflected wave cannot propagate downstream.

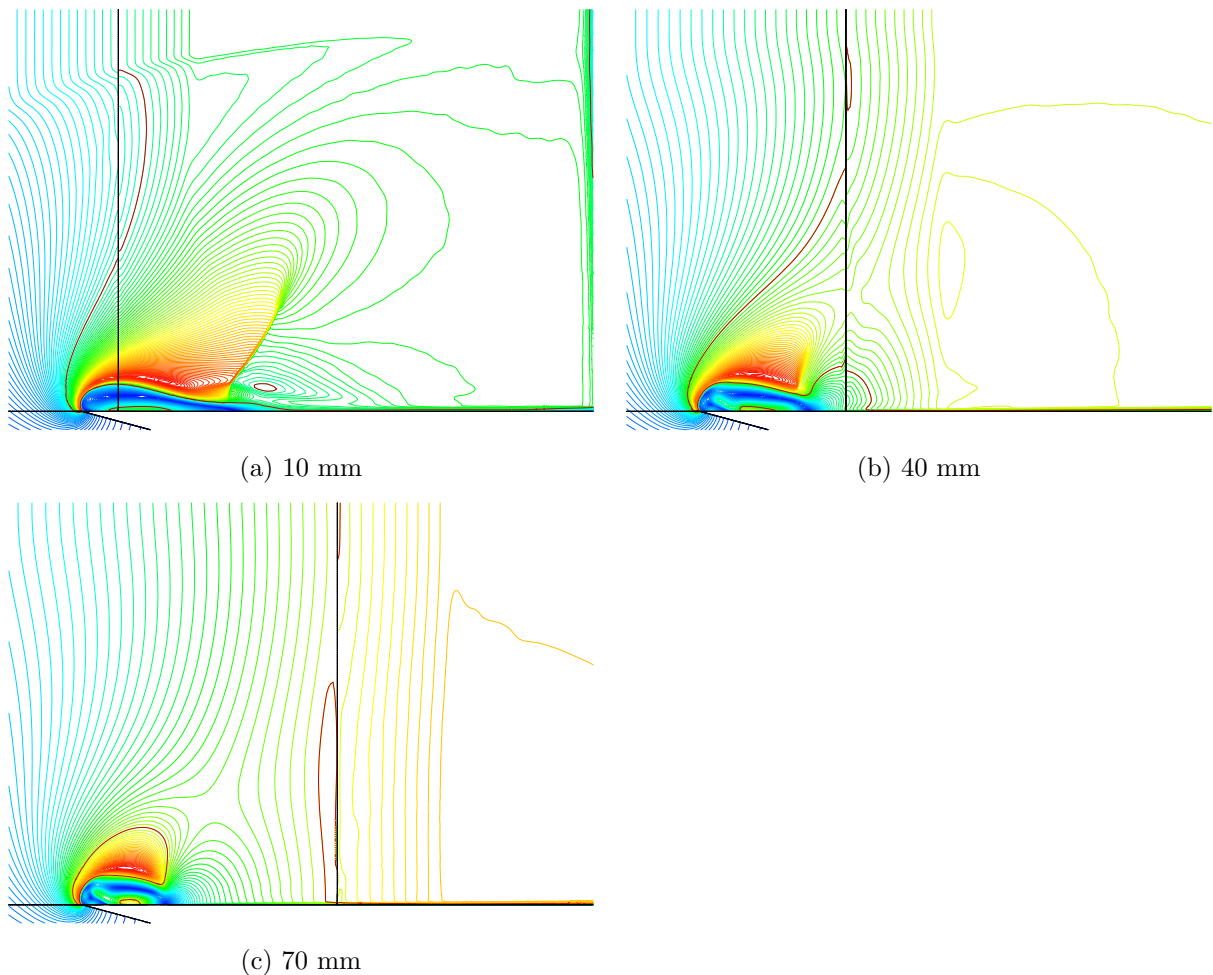


Figure 5.32: Mach number contour plot illustrating the separation bubble for subsonic and supersonic trailing flow with variation in d for $\theta = 15^\circ$ at $t = 350 \mu\text{s}$

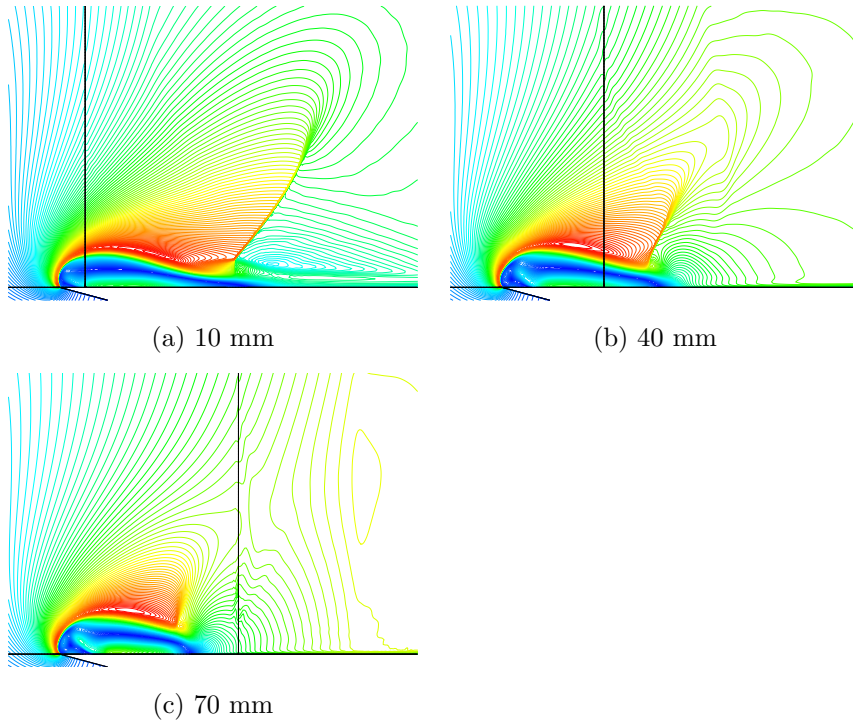


Figure 5.33: Mach number contour plot illustrating the separation bubble for subsonic and supersonic trailing flow with variation in d for $\theta = 15^\circ$ at $t = 600 \mu s$

Figures 4.34 and 4.35 show the result at different values of θ . Changing the corner angle seems to have no noticeable effect of on the flow field. The only observable difference would be the change in the profile of the bubble from the 90° corner and the increased velocity gradients around the bubble which was discussed earlier for subsonic trailing flow.

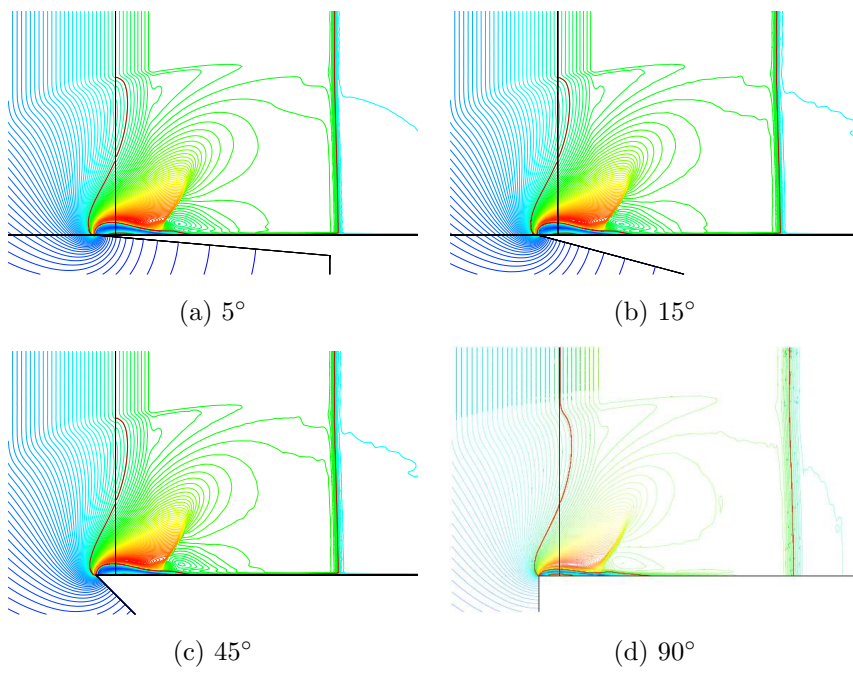


Figure 5.34: Mach number contour plot illustrating the separation bubble for subsonic and supersonic trailing flow with variation in θ for $d = 10$ mm at $t = 300 \mu\text{s}$

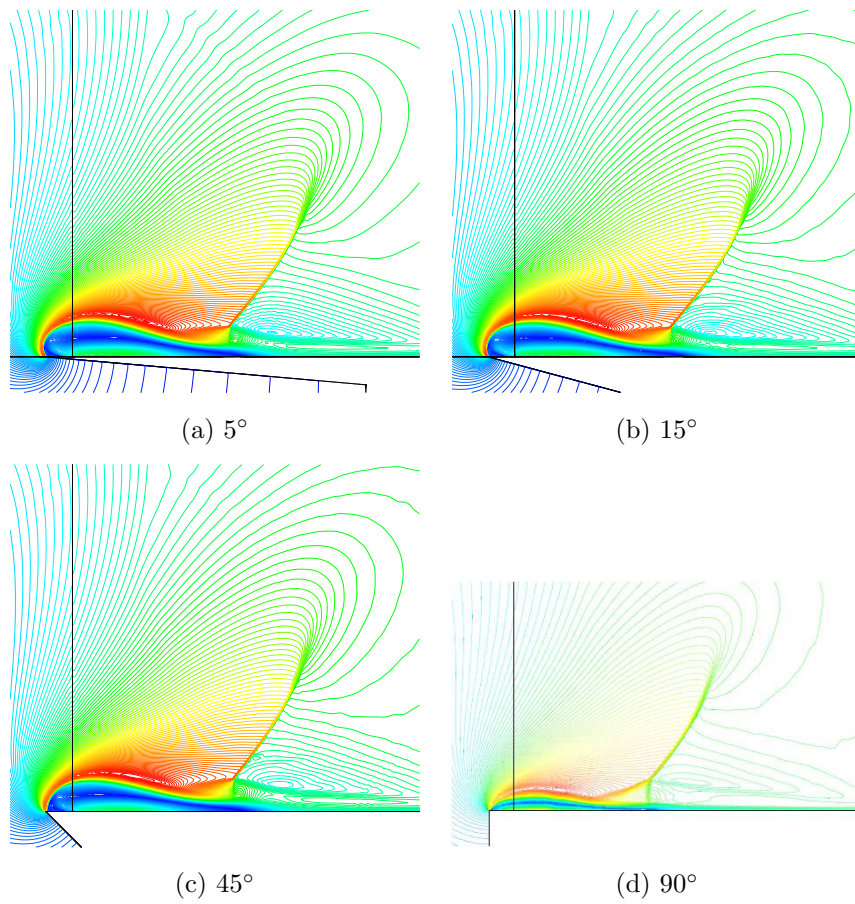


Figure 5.35: Mach number contour plot illustrating the separation bubble for subsonic and supersonic trailing flow with variation in θ for $d = 10$ mm at $t = 300 \mu\text{s}$

Part II

Large Eddy Simulation of expansion wave diffraction

Chapter 6 LES Computational Method

The LES computational analysis was based on the experimental study done by Mohamed in [4]. The domain was constructed to the dimensions of the experimental rig. Initial pressure diaphragm ratios were kept consistent to allow for comparison with the experimental as well as the RANS computational analysis.

6.1 The Computational Model

As discussed in 1.3 the resolution requirements to run a complete LES analysis are significantly high when compared to a RANS model. Consequently, hybrid RANS-LES techniques were employed. ELES served to reduce the number of mesh elements drastically. The embedded LES domain was created around the bottom wall of the driver and driven sections enclosing the separation bubble and wake region. The rest of the model formed the RANS domain. A schematic of the computational domain is shown in Figure 5.1.

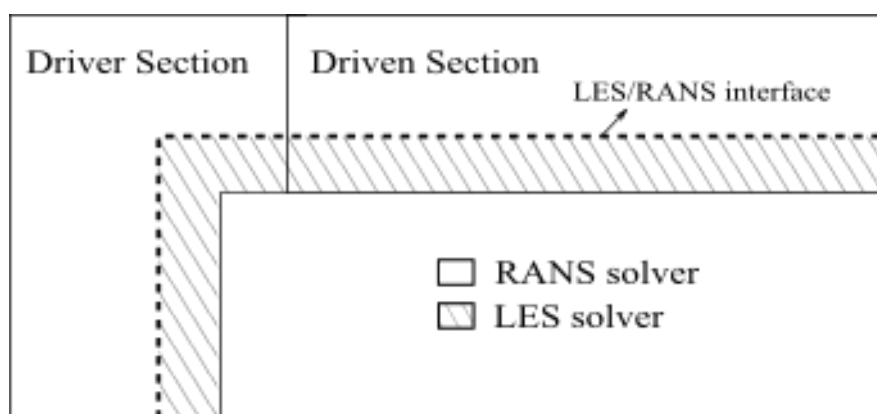


Figure 6.1: ELES Computational Domain

6.2 Mesh Development

A block meshing technique was used to allow smaller cell sizes in regions of interest which includes the separation bubble and wake region area. The illustration in Figure 5.2 demonstrates the mesh regions.

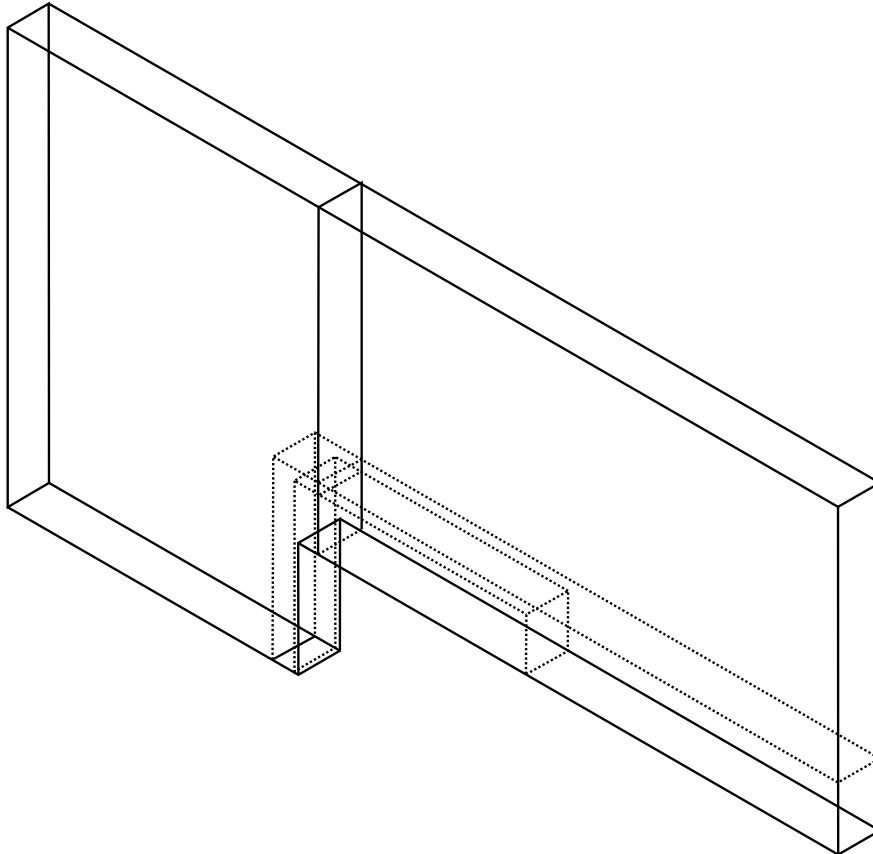


Figure 6.2: Mesh blocking in the LES region

A series of grids were generated until the mesh resolution produced satisfactory representation of the flow field. Three stages in the mesh development, labelled Mesh 1, Mesh 2 and Mesh 3 are described below. In the RANS portion of the mesh the grid resolution was kept constant at 0.5 mm x 0.5 mm x 1mm.

Mesh 1

The initial coarse mesh, summarised in Table 5.1, consisted of 12498220 elements. The minimum resolution was $\Delta y = 0.2$ mm, $\Delta x = 0.2$ mm and $\Delta z = 0.2$ mm.

Table 6.1: Mesh 1 Summary

Body	Elements
Driver RANS	125150
Driven RANS	137200
Driver LES	4954449
Driven LES	7540800

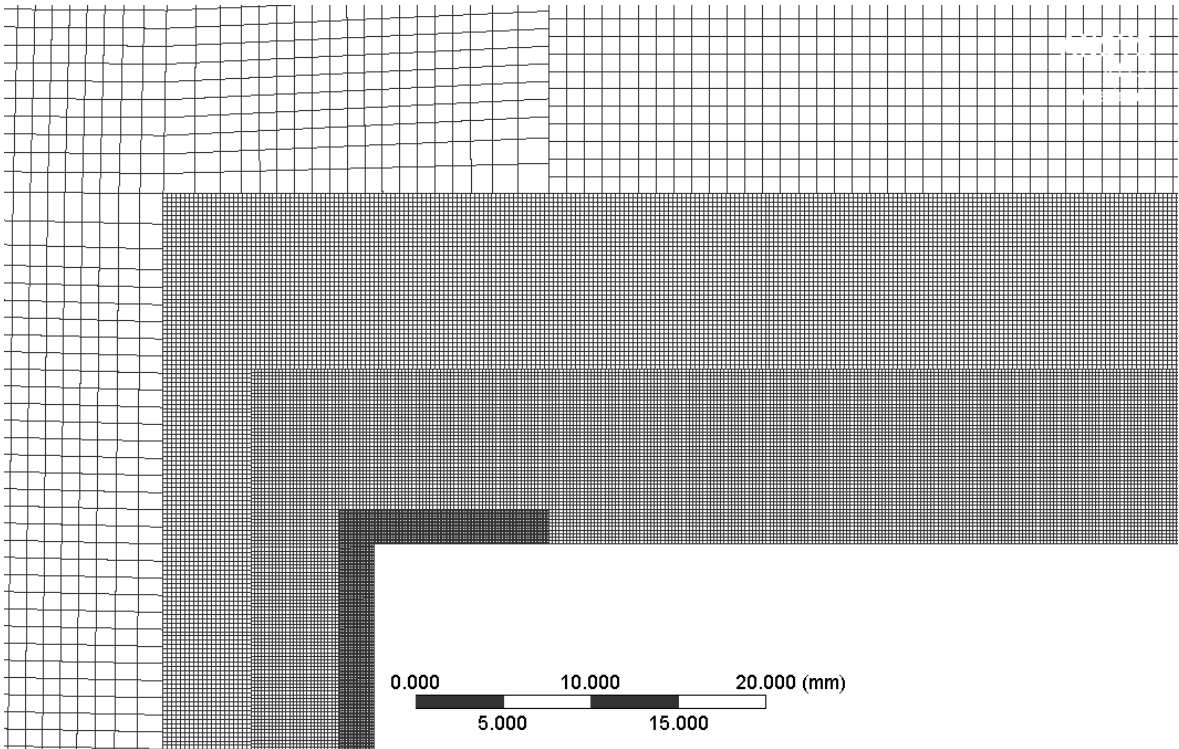


Figure 6.3: Illustration of Mesh 3 sizing

Mesh 2

The second mesh used totalled 47535950 elements. The minimum resolution was $\Delta y = 0.1$ mm, $\Delta x = 0.1$ mm and $\Delta z = 0.1$ mm.

Mesh 3

The final grid totalled 77803715 elements with a minimum resolution in the LES region of $\Delta y = 0.05$ mm, $\Delta x = 0.1$ mm and $\Delta z = 0.2$ mm.

Table 6.2: Mesh 2 Summary

Body	Elements
Driver RANS	123350
Driven RANS	113100
Driver LES	9589500
Driven LES	37710000

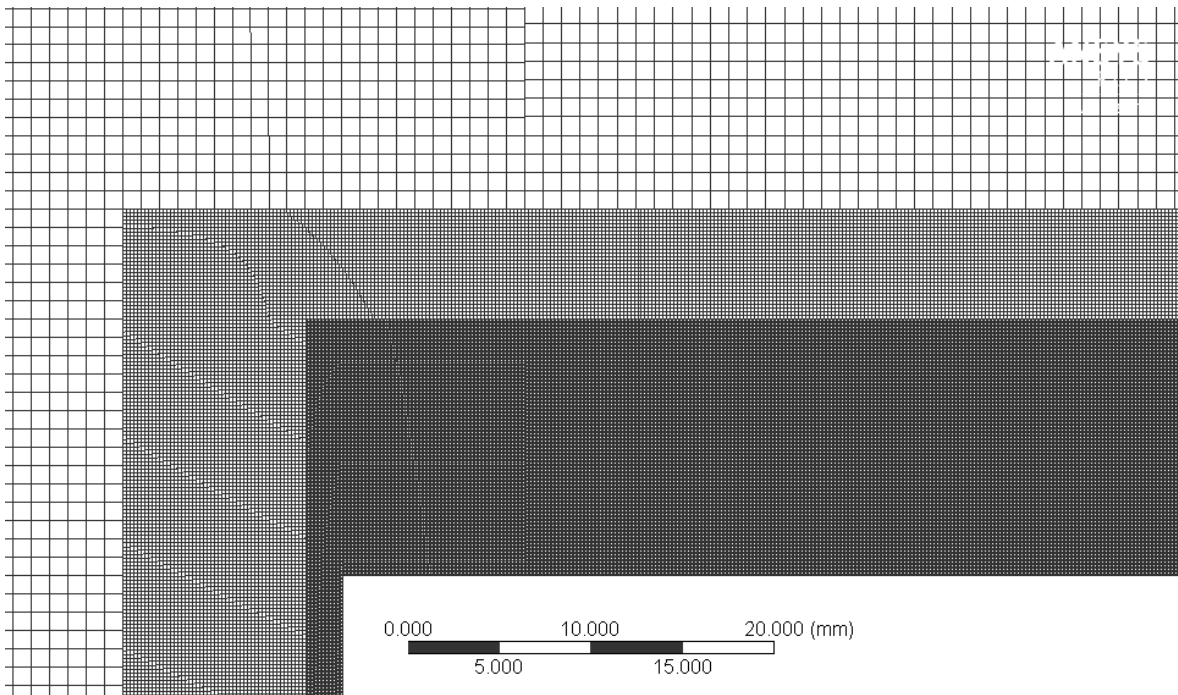


Figure 6.4: Illustration of Mesh 2 sizing

Table 6.3: Mesh 3 Summary

Body	Elements
Driver RANS	265100
Driven RANS	280240
Driver LES	11151375
Driven LES	66107000

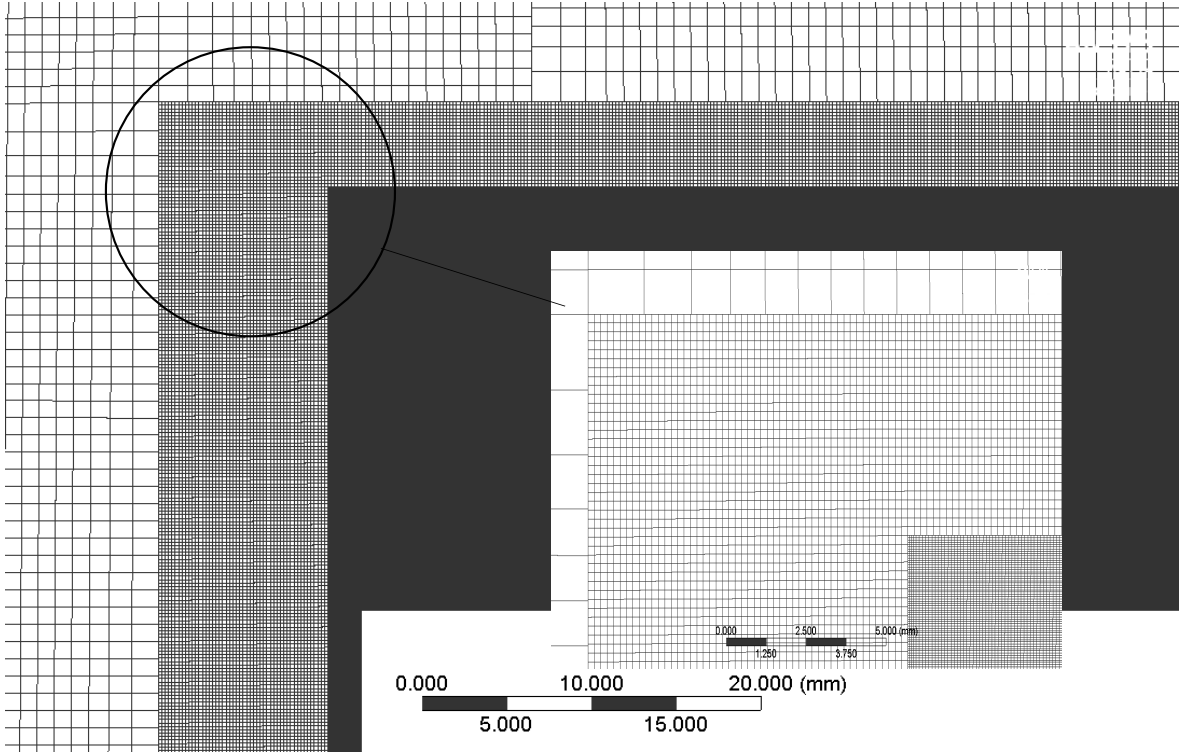


Figure 6.5: Illustration of Mesh 3 sizing

6.3 Subgrid Scale Modelling

Three of the SGS models (discussed in 1.7.2); the WALE, WMLES and WMLES-SO were used in a trial analysis to determine the best suited model for the problem. Mesh 1 was used for the SGS model study and as such may not provide well resolved results.

While the analysis conducted using these available models, it should be kept in mind that the results may not be a true indication of the problem due to limitations of the models. One would be concerned with the effect of an 'inverse error cascade' in which uncertainty in the smaller scales of motion would eventually result in errors at the larger, energy-containing, scales. Further concerns would be the problem of backscatter especially as when dealing with flow compressibility as in the current case.

WALE

As the WALE model attempts LES throughout the domain, including the near wall region, and a consistent mesh was used, the resolution within the boundary layer would be insufficient to resolve the turbulent scales. Due to uncertainties in these scales there is a higher possibility

of an inverse error cascade. An indication of the Kelvin-Helmholtz instability can be seen in the bubble which may confound backscatter energy transfer to the larger scales.

Figure 5.6 shows locations of unresolved turbulence along the wall. Hardly any indication of the wake region can be determined.

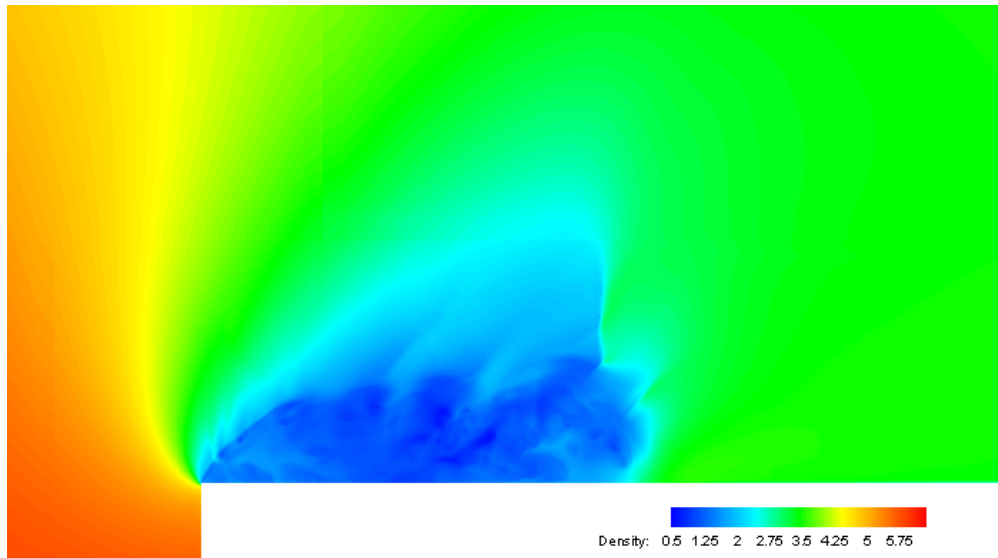


Figure 6.6: Near corner flow structure using the WALE SGS model

WMLES

While not sufficiently accurate, partially as a result of the low mesh resolution, the WMLES model showed a significantly improved results to the WALE model. This would result from the RANS modelling of the near wall turbulence. A slight indication of the wake region is seen to the rear of the bubble.

WMLES-SO

The turbulent structures in the separation bubble was notably damped in comparison to the the two previous models.

The WMLES SGS model was selected for further analysis at it provided the best results from the three models. It is expected the the accuracy of the results will increase with the use of a more refined mesh.

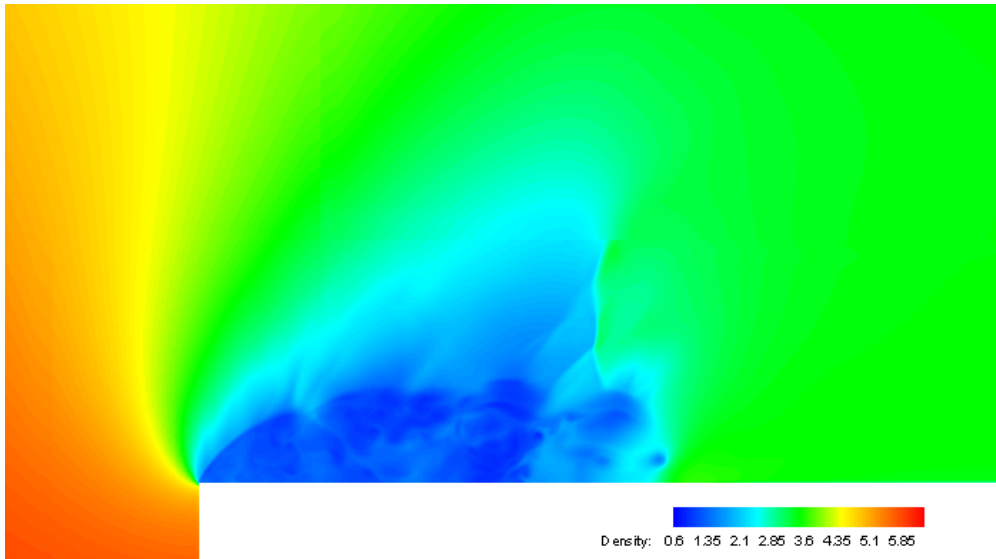


Figure 6.7: Near corner flow structure using the WMLES SGS model

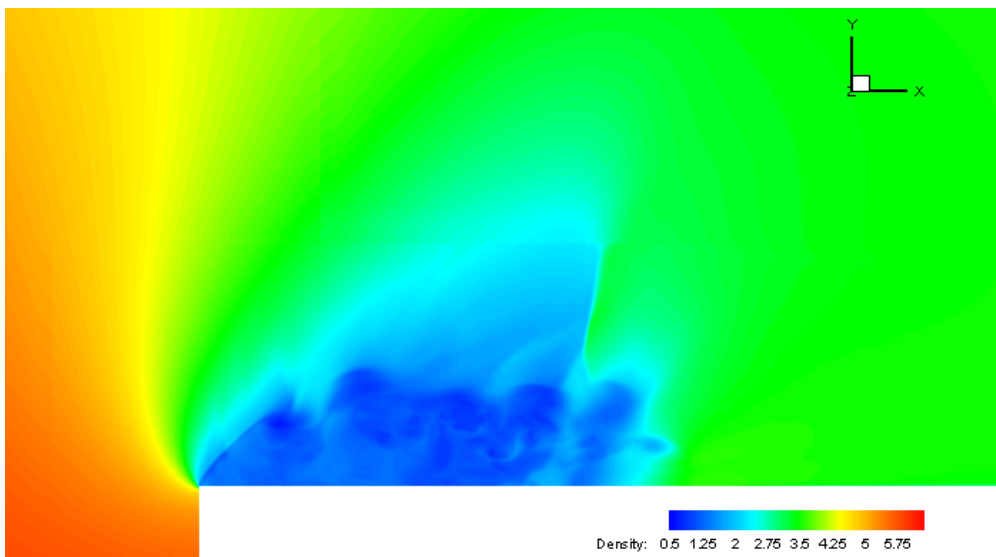


Figure 6.8: Near corner flow structure using the WMLES-SO SGS model

Chapter 7 Discussion

In this section the Large Eddy Simulation results are analysed and discussed. The data is compared with with the results from experimental tests as well as the RANS solutions. As the objective of the LES simulations was to resolve the flow features which were not resolved by RANS solvers only a few parameter sets were investigated. The first part of the chapter looks only at results for the 90° corner. The diaphragm distance was set at $d = 10$ mm to reduce the simulation time required. Initial diaphragm pressure ratio values were selected based on available experimental data and thus were limited to $P41 = 3.2$ and 7.7 . Towards the end of the chapter, LES solutions of the wedge case are briefly discussed.

7.1 The separation bubble

Figure 6.1 shows a comparison between the shadowgraph images and the LES density plots for $P41 = 3.3$ and 7.7 at a time delay of $400\mu\text{s}$. The density contours were plotted on the midplane of the domain which is at a depth of $z = 10$ mm. From these images the turbulent nature of the separation bubble, which was not resolved with the RANS solver is clearly evident in LES solution. The shape of the separation bubble for $P41 = 3.2$ in Figures 6.1a and 6.1b are found to be almost identical. This was not the case with the RANS solution where the separation bubble was more rounded near the diffraction edge. A slight indication of the wake region beginning to form is observed in Figure 6.1b however, turbulence in the region is still unresolved. This is due to the turbulent structures in the wake region being of a subgrid size and as result too small for the LES solver to resolve with the current grid size. In order to resolve the wake region a very fine grid would be required in that area. This would also require a reduction in the time step size increasing the simulation time significantly.

The profile of the separation bubble in the LES solution for $P41 = 7.7$ is less smooth and several breaks are found in the shear layer. In the image in Figure 6.1d a large discontinuity in the shear layer is seen towards the middle of the bubble. A close inspection of the shadowgraph image shows that instabilities in the shear layer are present. However, the structure

of the bubble through the depth cannot be analysed experimentally and the presence of the discontinuity cannot be confirmed.

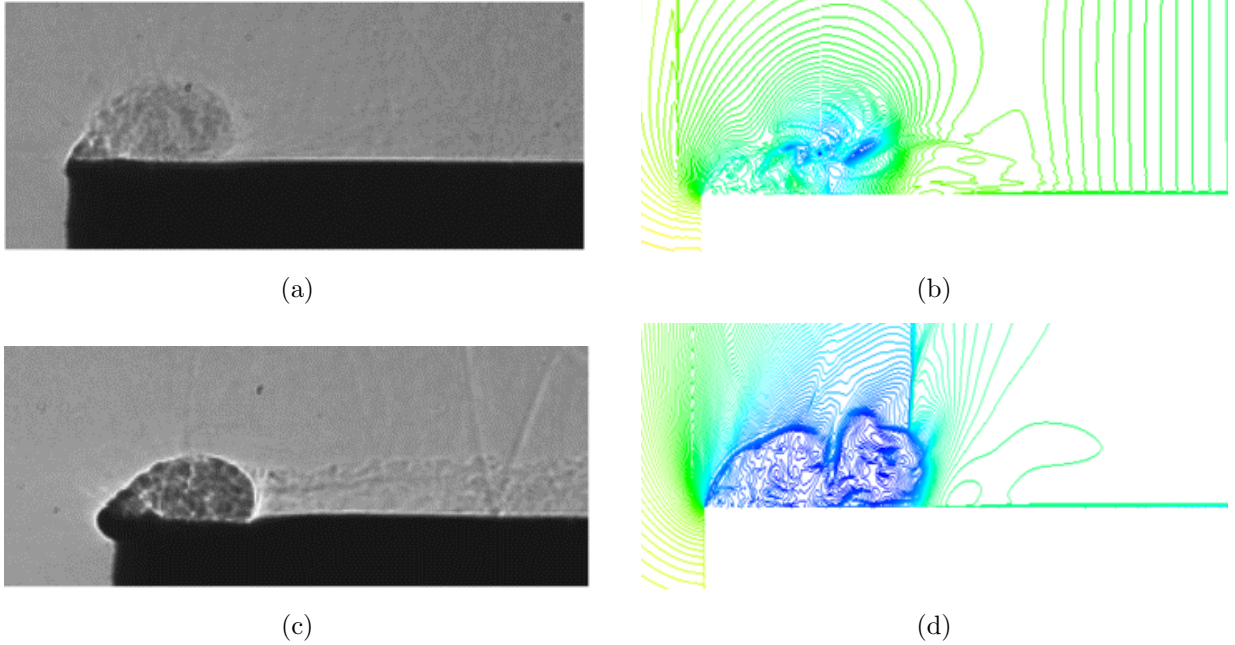


Figure 7.1: Comparison between shadowgraph imagery and LES density contour plots. (a), (b) $P41 = 3.2$ (c), (d) $P41 = 7.7$. $t = 400 \mu s$

Figures 6.3 to 6.4 show the structure of the separation bubble at different depths through the bubble for $P41 = 3.2$ and 7.7 at $t = 200, 400$ and $600 \mu s$. The planes selected were $z = 5$ mm, 10 mm and 15 mm. The internal structure and the profile of the bubble shows quite a significant variation through it's depth. The discontinuity in the shear layer at $z = 10$ mm for $PR = 7.7$ is not observed to be consistent throughout the depth.

The closer correlation between the results for $P41 = 3.2$ than $P41 = 7.7$ could result from the presence of the oblique shock and tiny shocklets which develop around the profile bubble at higher pressure ratios. The discussion in Section 1.6.2 indicates that the current SGS models are not advanced enough to accurately model energy transfer between the different turbulence modes. In this case a strong coupling between the vortical and acoustic modes would be expected. The presence of shocklets strongly affect the dilational field. Due to the large correlation between the pressure and dilational fields near shocklets a local enhancement in the transfer between internal energy and turbulent kinetic energy occurs [8].

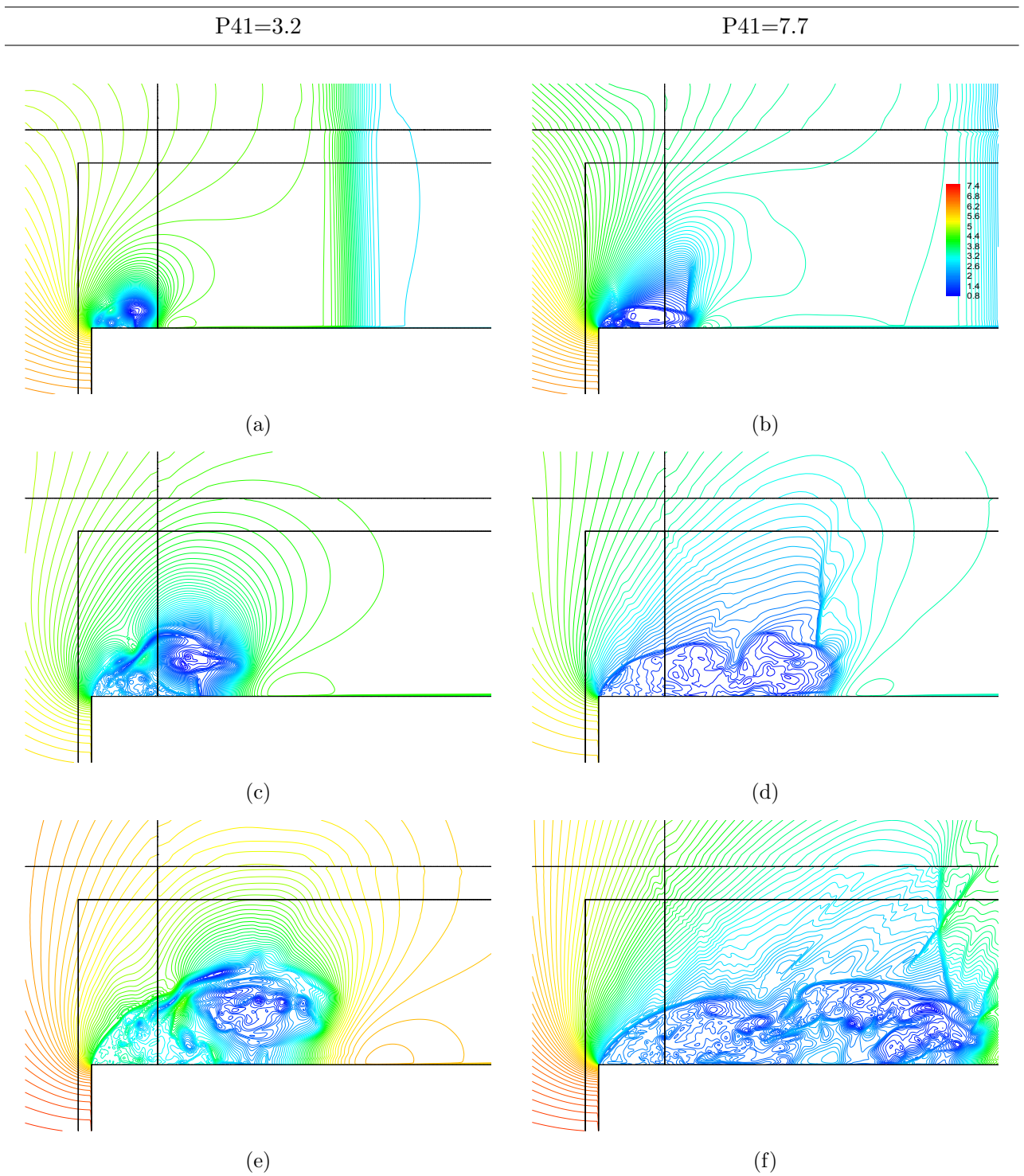


Figure 7.2: Density contour plots at $P41 = 3.2$ and $P41 = 7.7$ at $z = 10$ mm (a,b) = $200 \mu s$ (c,d) = $400 \mu s$ (e,f) = $600 \mu s$

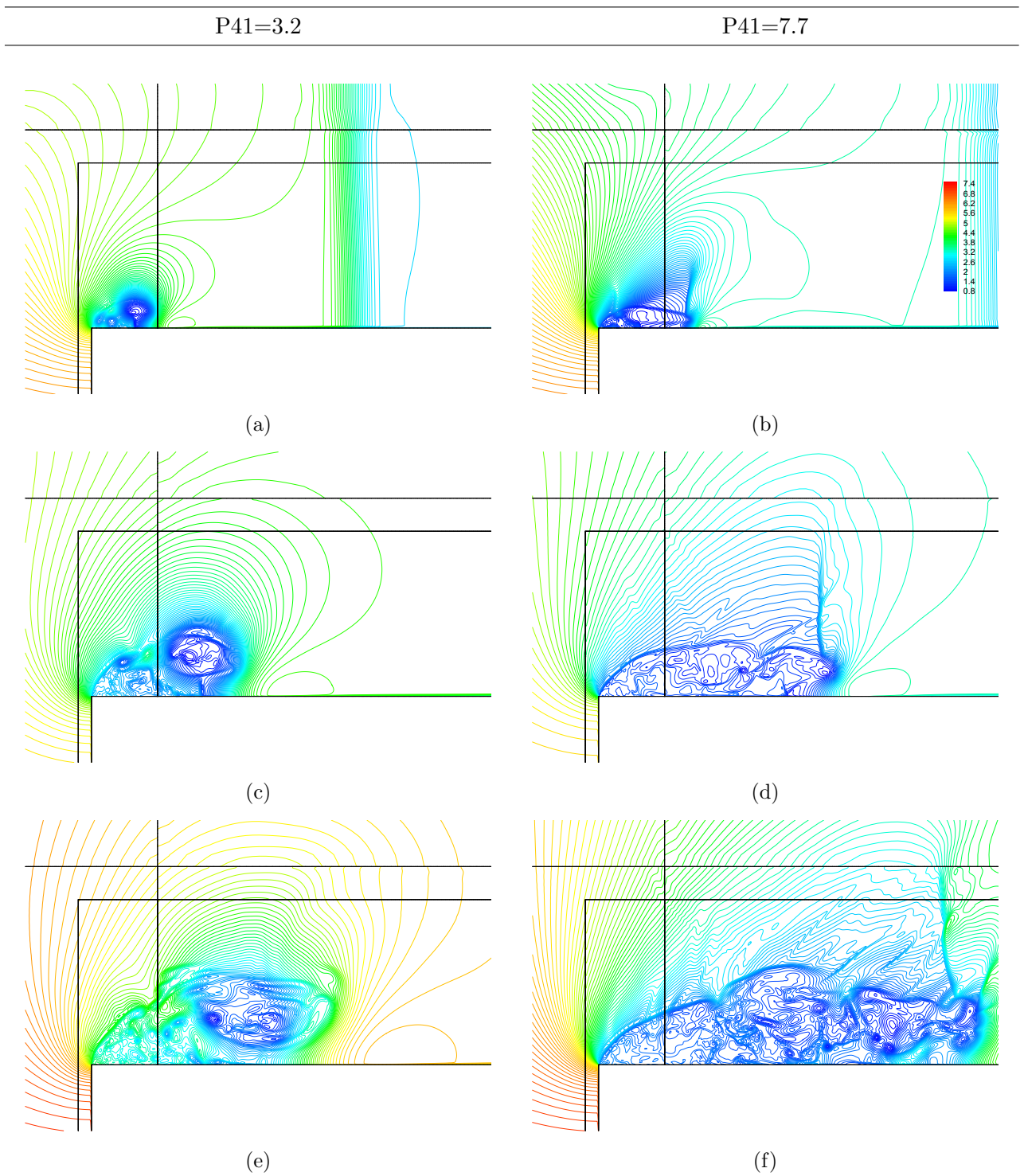


Figure 7.3: Density contour plots at PR = 3.2 and PR = 7.7 at $z = 5$ mm (a,b) = $200 \mu\text{s}$ (c,d) = $400 \mu\text{s}$ (e,f) = $600 \mu\text{s}$

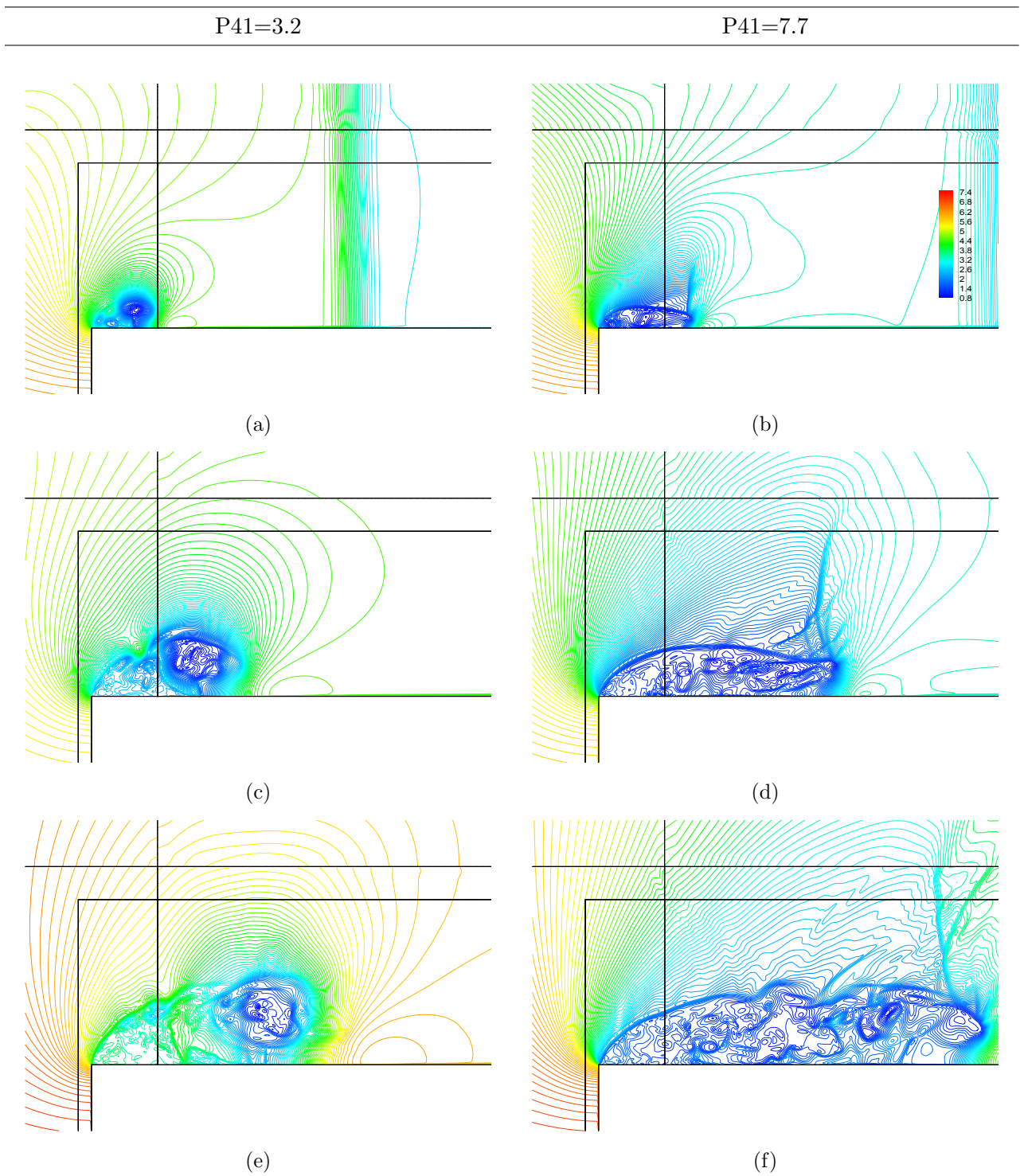


Figure 7.4: Density contour plots at $P41 = 3.2$ and $P41 = 7.7$ at $z = 15$ mm (a,b) = $200 \mu s$ (c,d) = $400 \mu s$ (e,f) = $600 \mu s$

7.2 Viscous vortices

Vector plots of the velocity magnitude on the midplane of the bubble are shown in Figure 6.5 for P41 values of 3.2 and 7.7. The near-corner region is shown in Figures 6.5c and 6.5d to illustrate the mini vortices that formulate close to the diffraction corner that were identified in the RANS analysis. Vector plots at depths 5, 10 and 15 mm are shown in Figures 6.7 to 6.8 comparing the vortex structure through the depth of the bubble. Due to the 3D nature of the bubble the primary vortex cannot be observed clearly on the planar images especially for $P41 = 7.7$. The circulatory flow in the bubble can be observed from 3D illustrations provided in Figures 6.9 and 6.10 of the streamtraces around the vortex core. At later times, for $P41 = 7.7$ vortex shedding is observed towards the rear of the bubble.

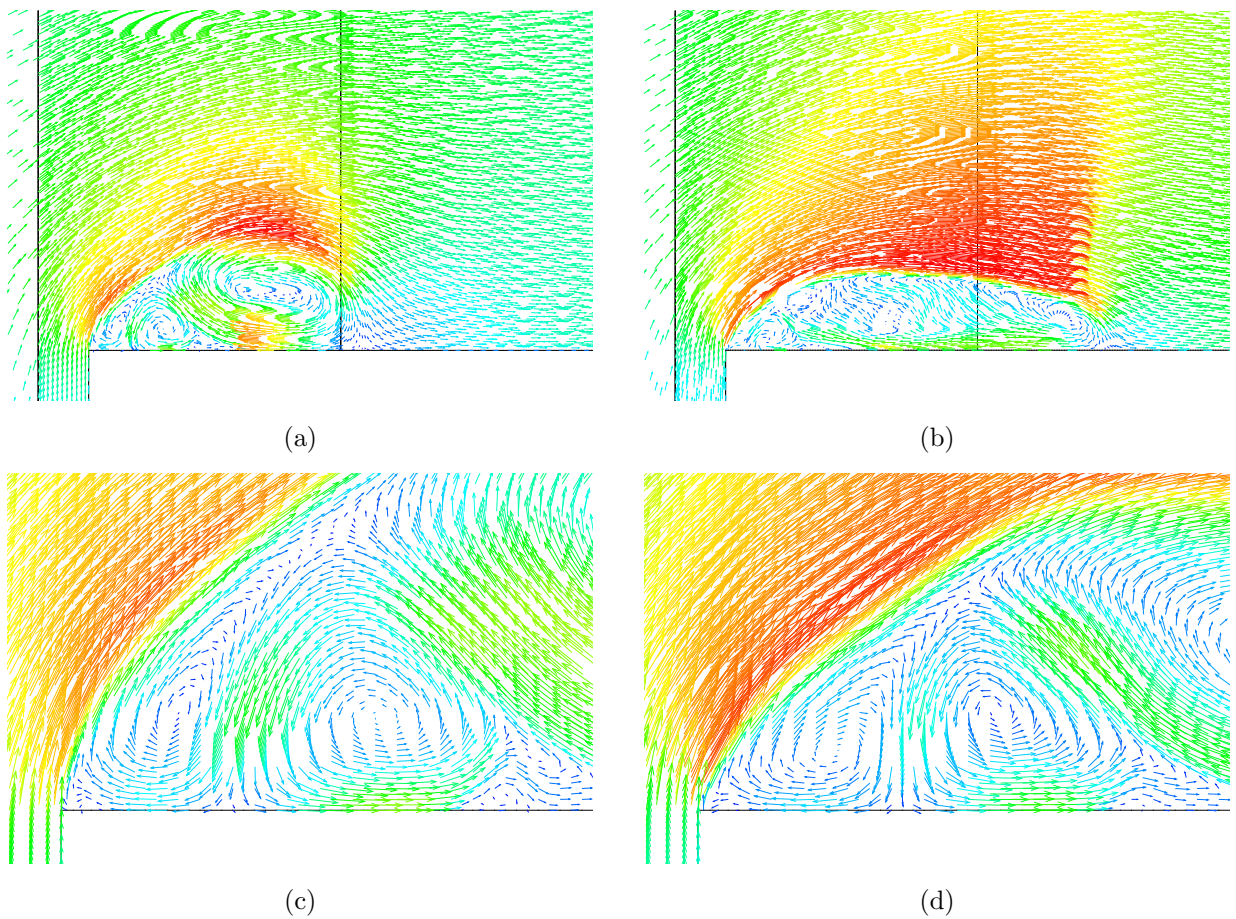


Figure 7.5: Velocity magnitude vector plots of the separation bubble and near corner region. (a, b) $P41 = 3.2$ (c, d) $P41 = 7.7$. $t = 200 \mu s$

P41=3.2

P41=7.7

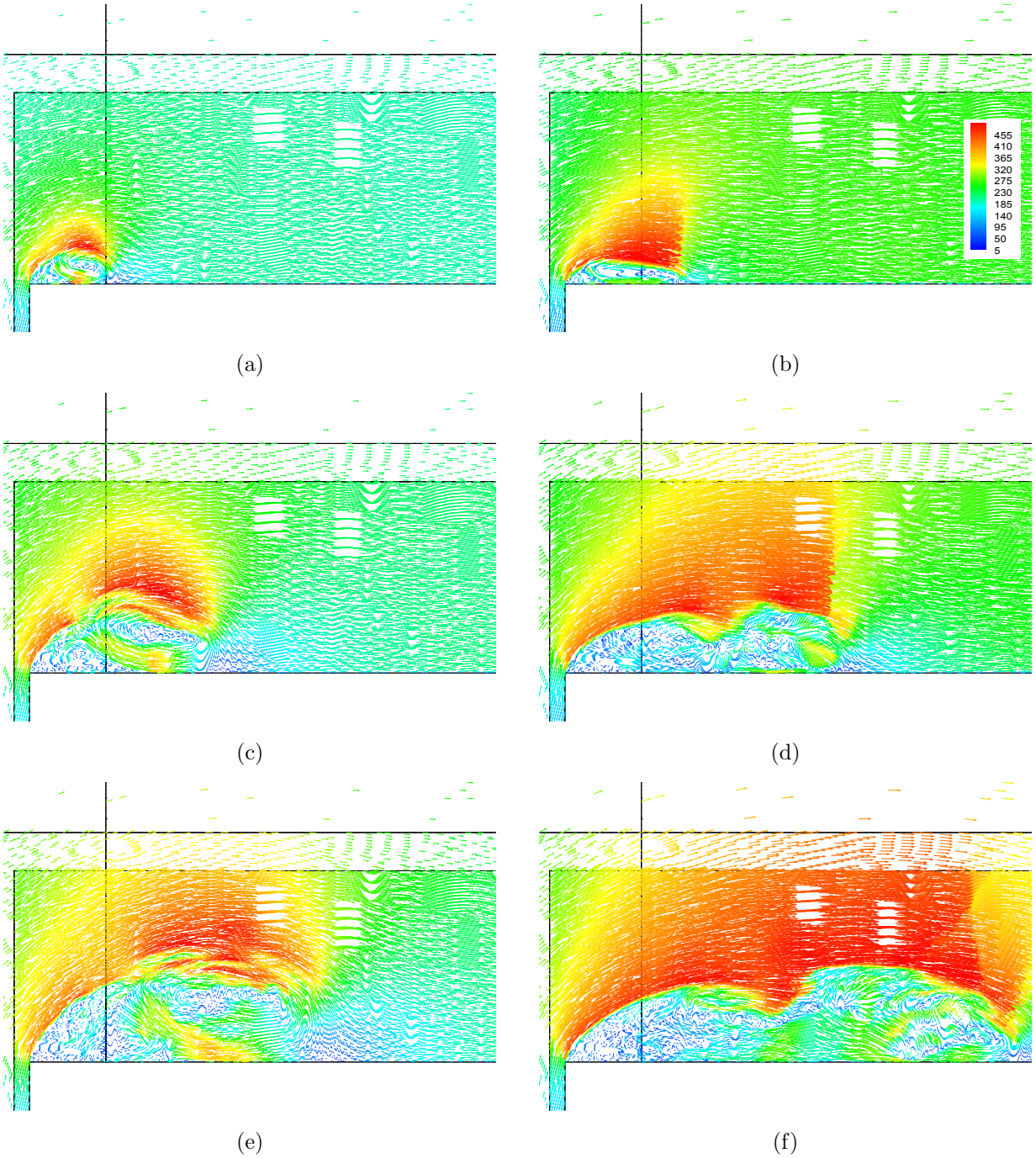


Figure 7.6: Velocity magnitude vector plots at PR = 3.2 and PR = 7.7 at $z = 10$ mm (a, b) = $200 \mu s$ (c, d) = $400 \mu s$ (e, f) = $600 \mu s$

P41=3.2

P41=7.7

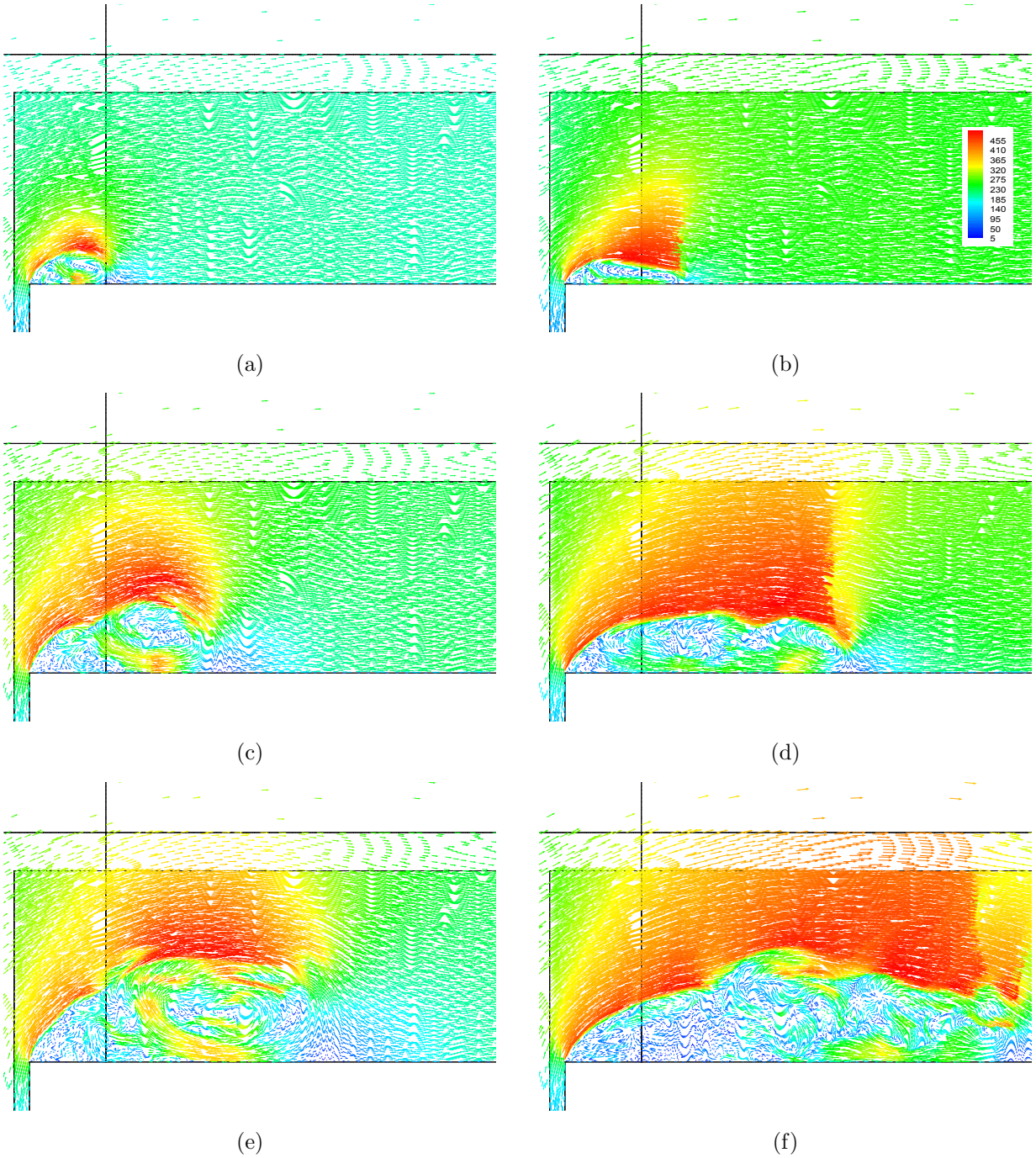


Figure 7.7: Velocity magnitude vector plots at $PR = 3.2$ and $PR = 7.7$ at $z = 10 \text{ mm}$ (a, b) $= 200 \mu s$ (c, d) $= 400 \mu s$ (e, f) $= 600 \mu s$

P41=3.2

P41=7.7

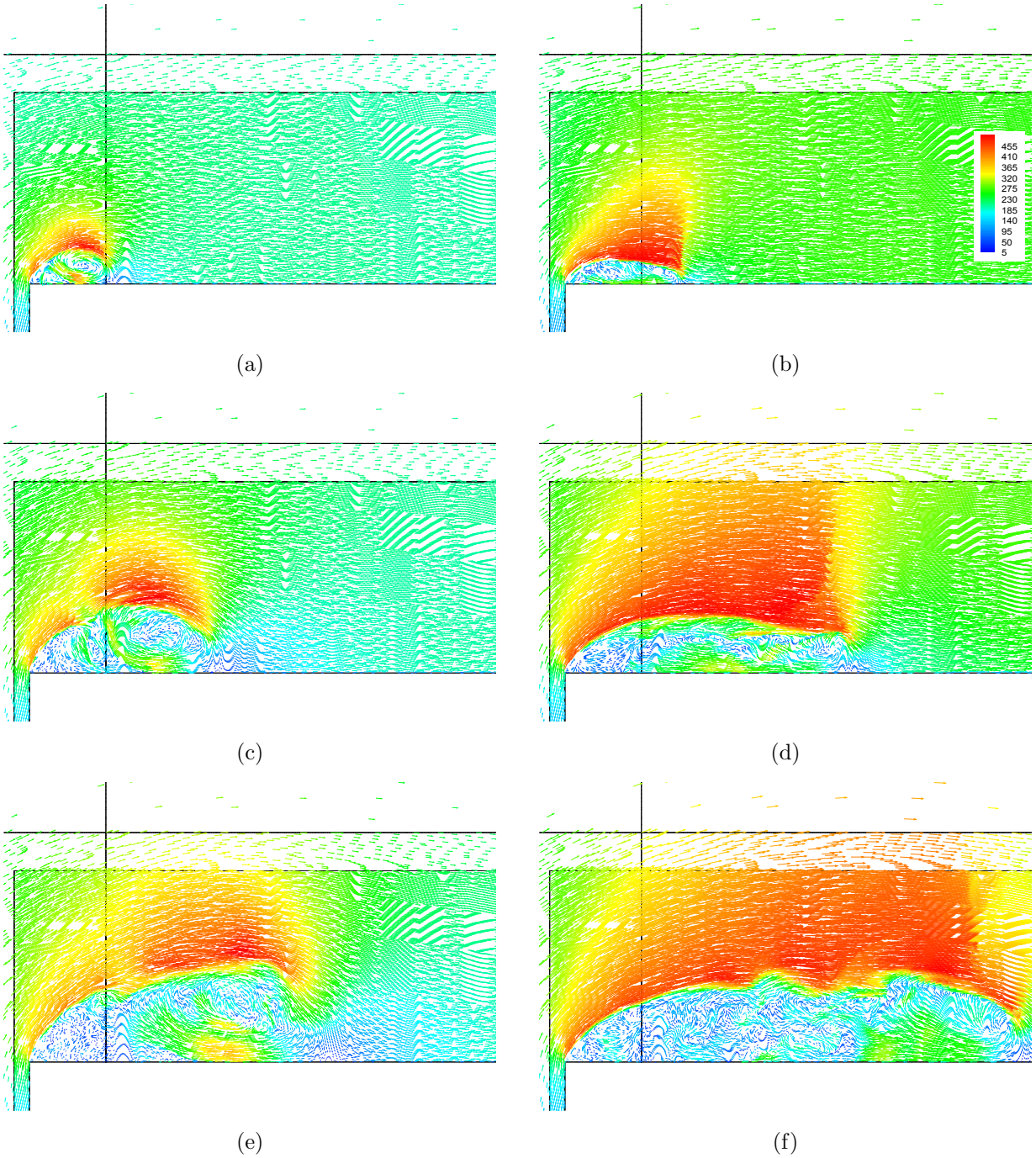


Figure 7.8: Velocity magnitude vector plots at PR = 3.2 and PR = 7.7 at $z = 15$ mm (a,b) = $200 \mu s$ (c,d) = $400 \mu s$ (e,f) = $600 \mu s$

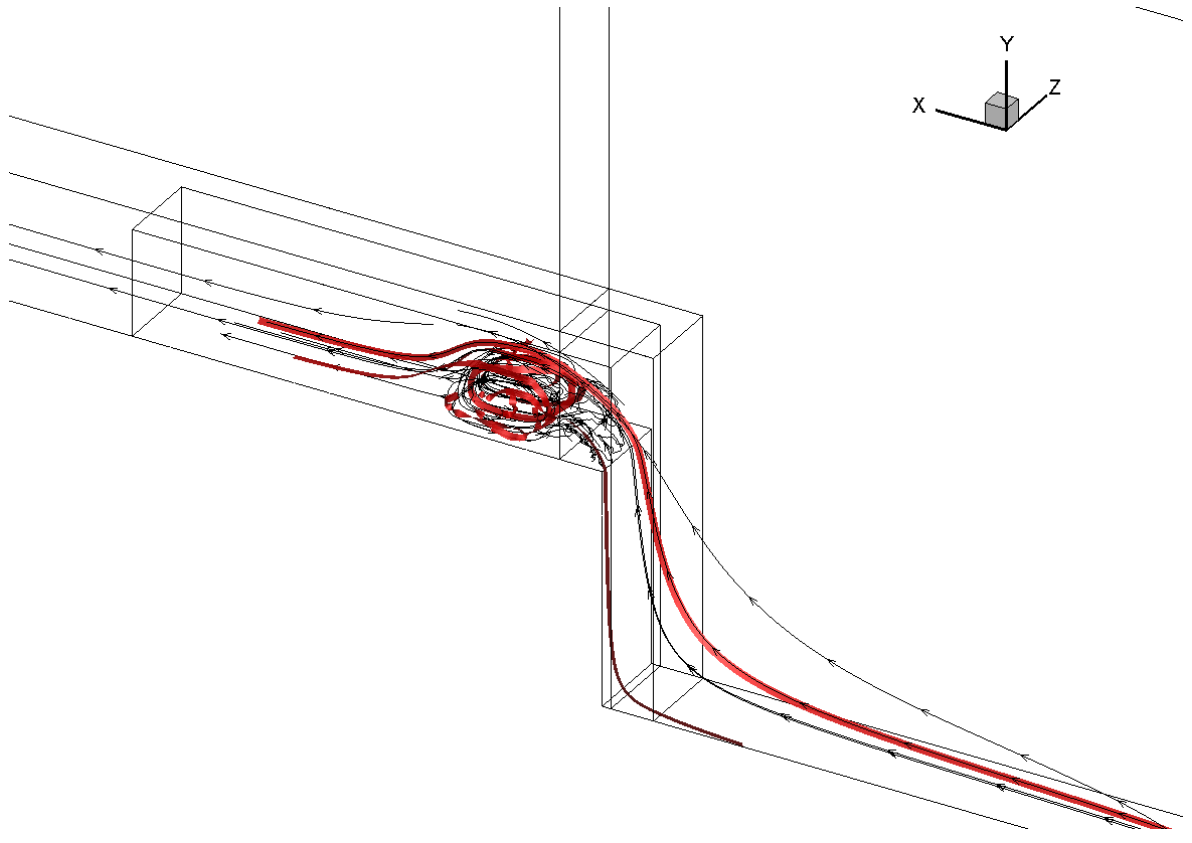


Figure 7.9: Vortex Core Steamtrace P41=3.2, $t = 600 \mu s$

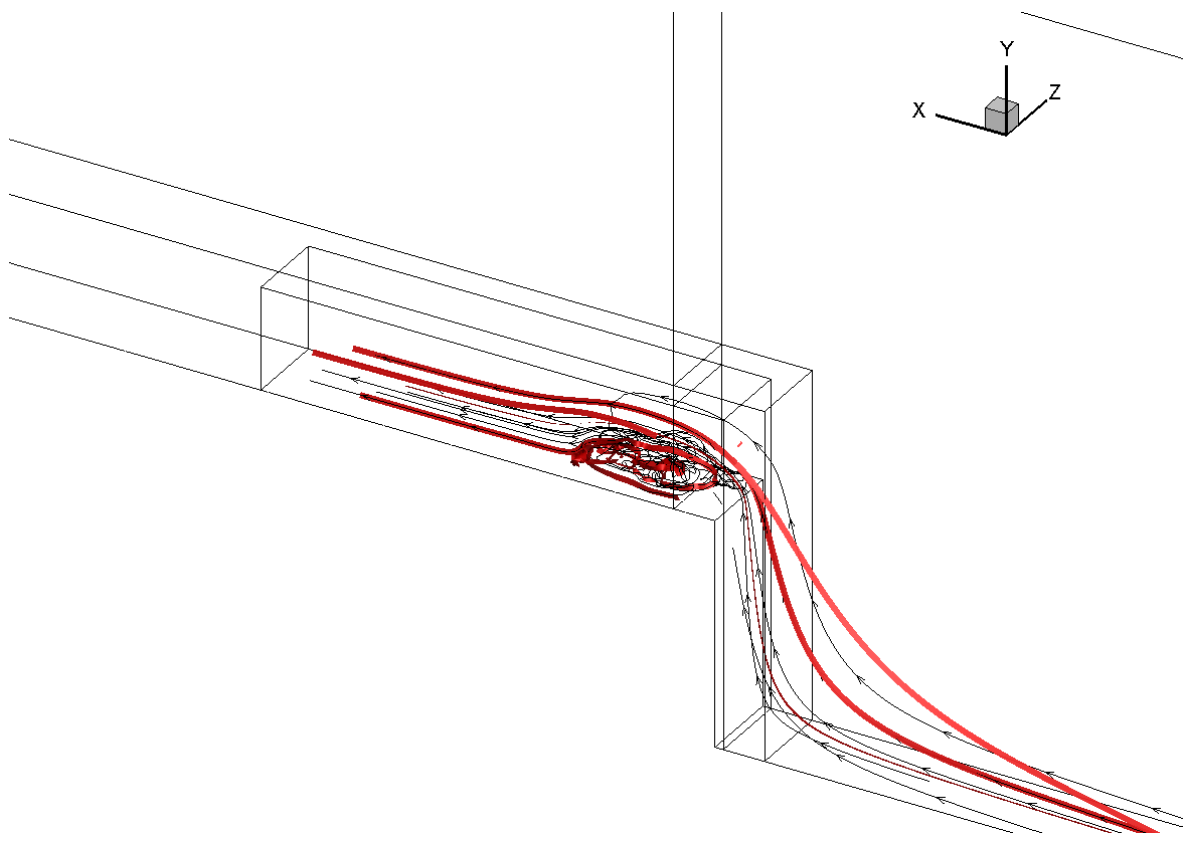


Figure 7.10: Vortex Core Steamtrace P41=7.7, $t = 600 \mu s$

The mean flow velocity through the separation bubble was considered for the RANS and LES cases. The results are shown in Figure 6.11 where x_s is the stagnation point and U_e is the velocity following the expansion wave. The RANS and LES results correlate fairly well validating the LES analysis. The RANS velocities are over estimated to a certain extent due unresolved turbulence as well as the large grid resolution used in the region of the bubble.

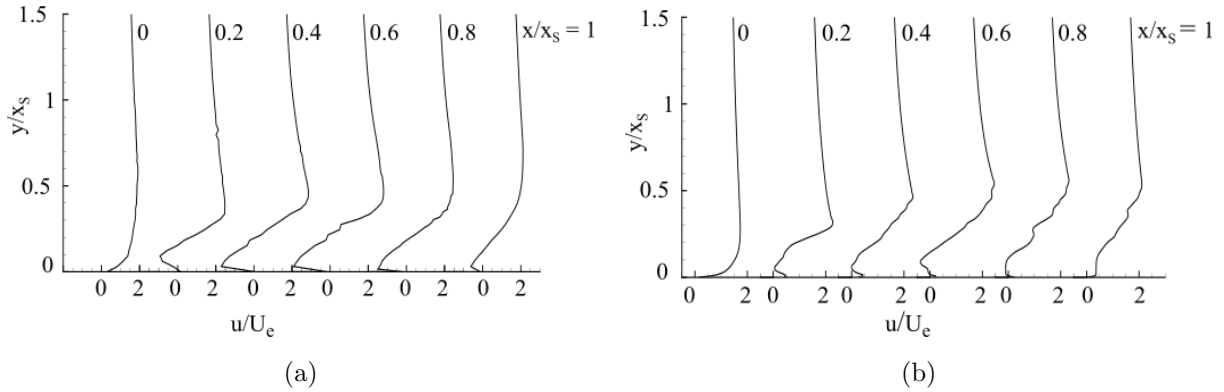


Figure 7.11: Mean velocity distribution through the separation bubble (a) RANS (b) LES

7.3 The Oblique Shock and Supersonic Region

The oblique shock and supersonic region are now examined through the depth of the bubble. Mach number plots illustrating the supersonic region (red Mach 1 trace) at different depths through the bubble are given in Figures 6.12 and 6.13. A major portion of the profile remains consistent through the depth of bubble. The bottom region of the profile varies largely with the depth due as it forms along a high turbulence region in the bubble. Several tiny regions of supersonic flow are seen to develop within the bubble.

The profile of the oblique shock is not consistent through the depth. From Figure 6.12b at 400 μs the oblique shock is seen to curve significantly at the centre line of the bubble while the shock profile is near normal closer to the walls. The plots in Figure 6.13 show that as time progress the ends of the shock also develop a curved profile.

Several shocklets are seen to develop around the periphery of the bubble. These were identified from the experimental results but were unresolved in the RANS solution. In the previous analysis it was suggested that the shocklets could be a result of rig dependant effects. This is seen not to be true as the they were resolved by the LES code. As the shocklets emanate from the bubble they are most probably turbulence induced 'eddy-shocklets'.

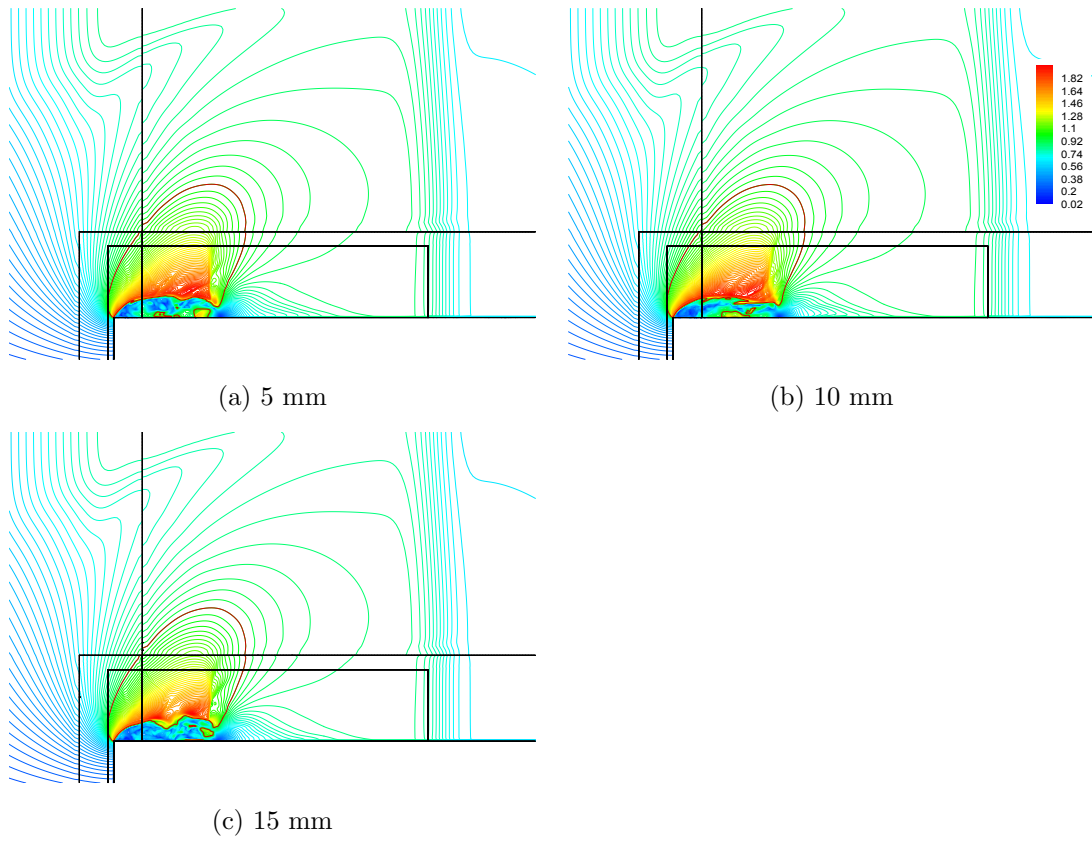


Figure 7.12: Mach number contour plot with sonic line trace (red). $P41 = 7.7$, $t = 400 \mu s$

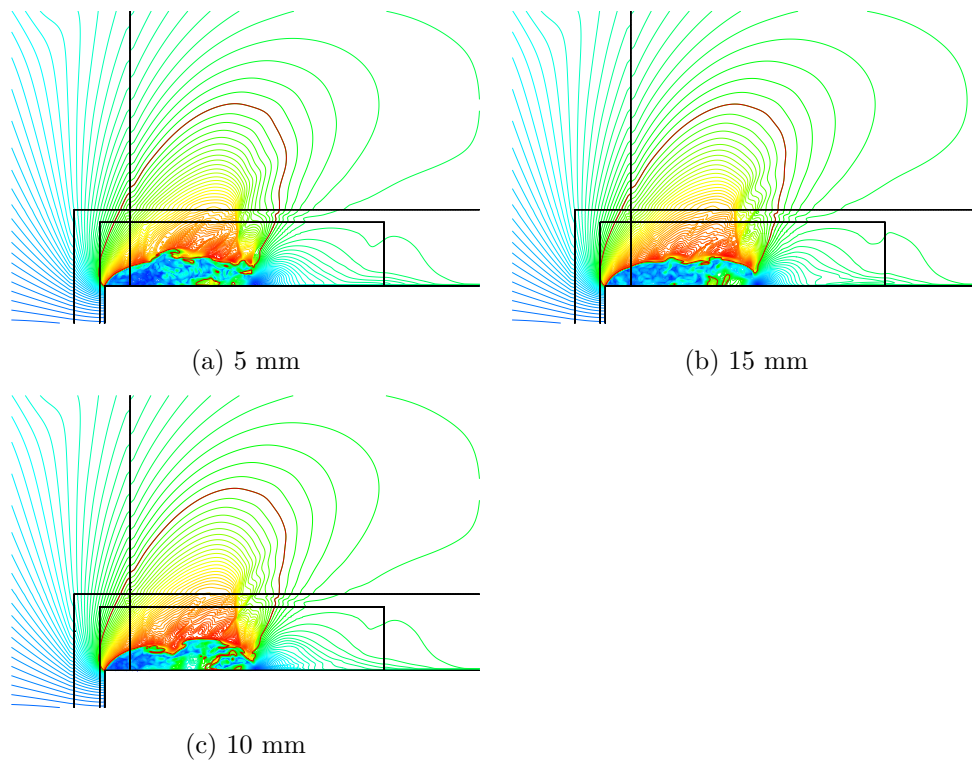


Figure 7.13: Mach number contour plot with sonic line trace (red). $P41 = 7.7$, $t = 600 \mu s$

7.4 LES Results for $\theta = 15^\circ$, $P41 = 3$

A comparison between the schlieren image and the RANS and LES solutions for the 15° is shown in Figure 6.14. The images show a good agreement with regards the separation bubble's shape and size. In the LES solution much of the turbulent vortical structures within the bubble was resolved.

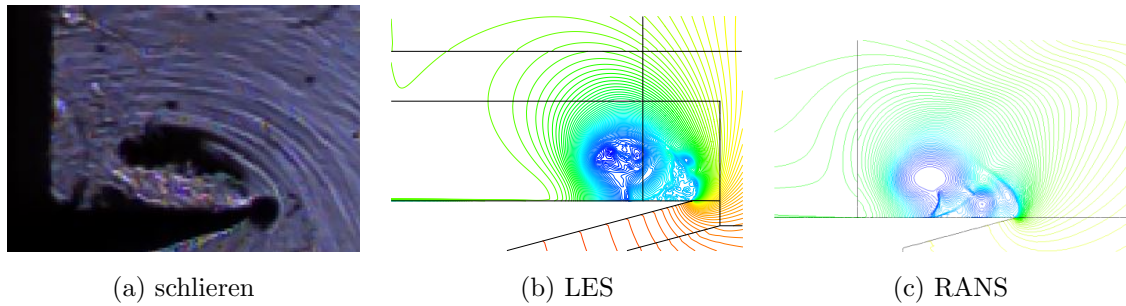


Figure 7.14: Comparison between schlieren image, RANS and LES results $\theta = 15^\circ$, $P41 = 3$

In schlieren images in Figure 6.15, taken using a horizontal knife edge, the shear layer is seen to be smooth and consistent around the profile of the bubble at $205 \mu\text{s}$. For $511 \mu\text{s}$ it is seen that as time progresses the shear layer would become unstable towards the top of the bubble and vortex shedding is evident.

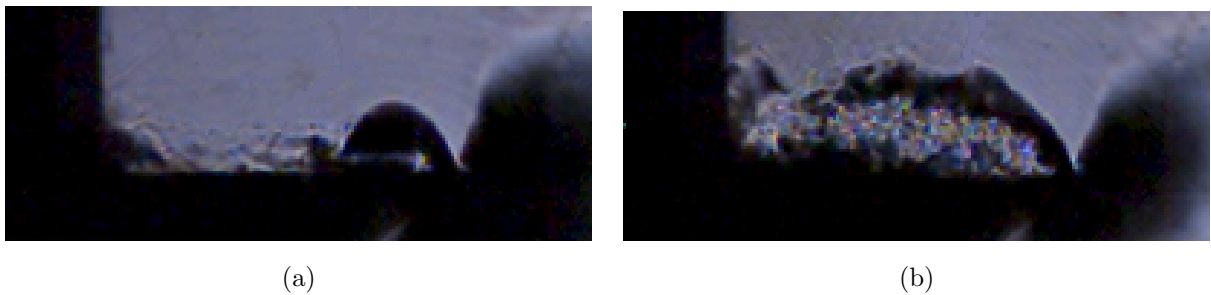


Figure 7.15: Horizontal knife-edge schlieren images emphasizing the shear layer and later shear layer instability

The schlieren and midplane density plots in Figure 6.16 show the structure of the separation bubble for $t = 200, 400$ and $600 \mu\text{s}$. As found previously the bubble has a much rounder profile than for the 90° case. At early times the shear layer is consistent until it reattaches to the wall. The shear layer is not very visible in the corresponding schlieren image as a vertical knife edge was used. At later times shear layer instability becomes apparent for both the experimental and numerical solution.

Velocity vector plots on the midplane are shown in Figure 6.17 illustrating the primary and secondary vortices in the bubble. The images for $t = 400 \mu\text{s}$ show a squaring of the bubble near the diffraction corner. However, this does not seem to be the case through the depth bubble. This would be seen from the plots on alternate planes provided in Appendix B.

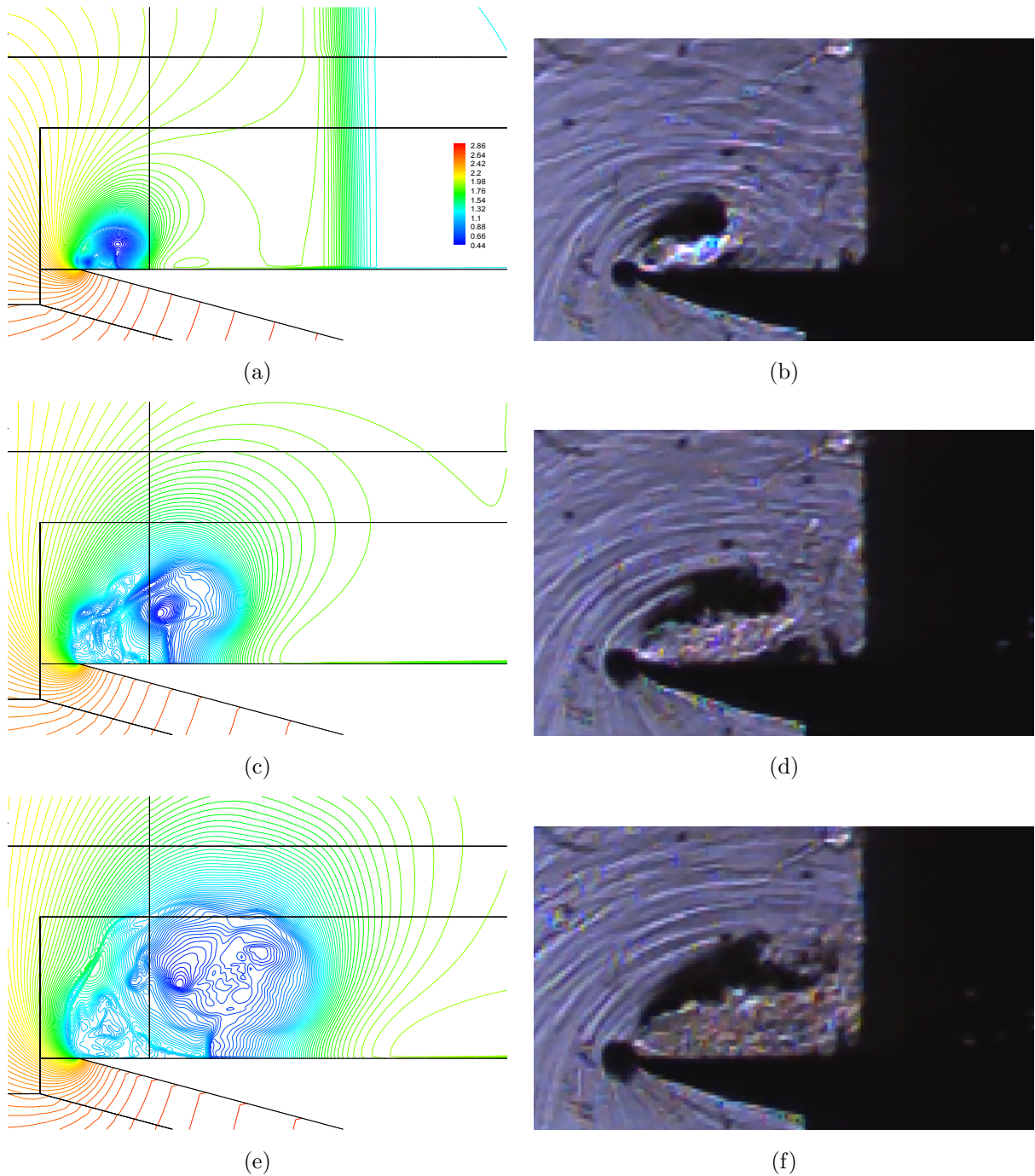
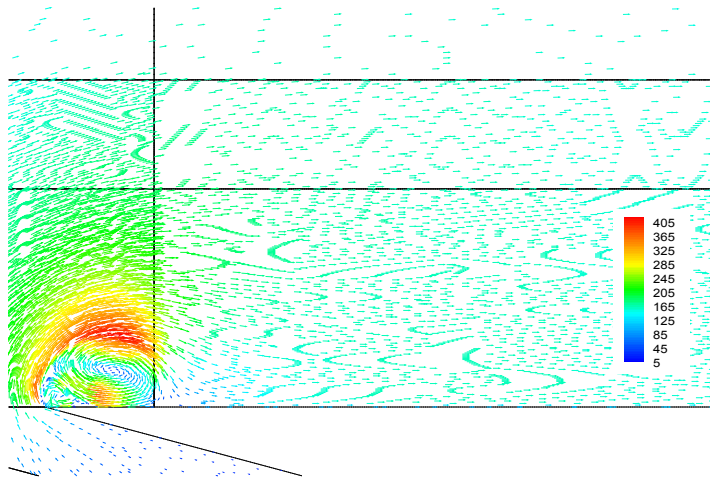
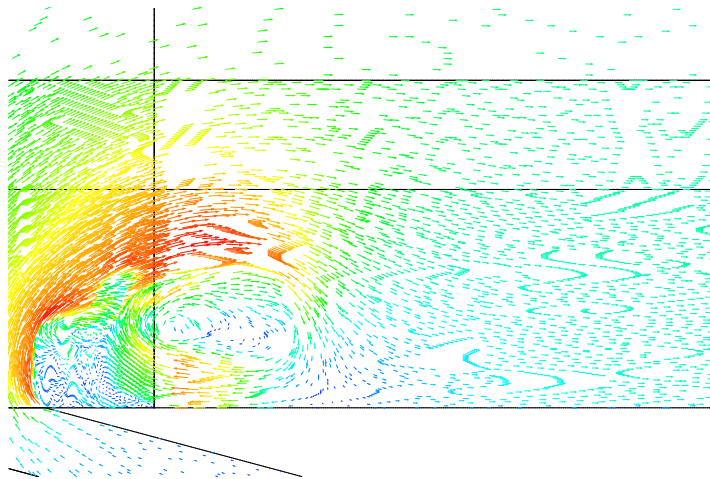


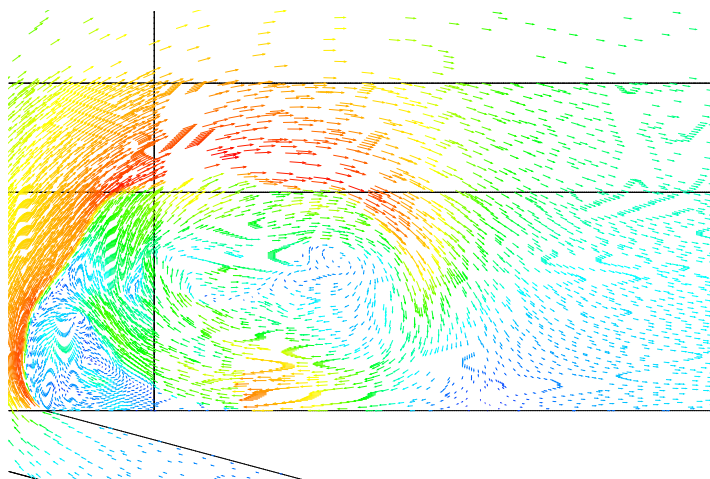
Figure 7.16: LES Density contour plots for $\theta = 15^\circ$, $P41 = 3$. (a, b) = $200 \mu\text{s}$, (c, d) = $400 \mu\text{s}$, (e, f) $600 \mu\text{s}$



(a) $t = 200 \mu s$



(b) $t = 400 \mu s$



(c) $t = 600 \mu s$

Figure 7.17: LES Velocity vector plots for $\theta = 15^\circ$, $P41 = 3$

Chapter 8 Conclusions

Results from the RANS wedge analysis

When the results from the wedge corner to the 90° solution was compared, no major differences in the flow field were identified. However the following observations were made:

- The shear layer was observed to reattach to the horizontal wall for all corner angles investigated. These included $\theta = 90^\circ, 45^\circ, 15^\circ$ and 5° .
- The effects of varying P41 and d that had been observed with the 90° corner was found to be true for the wedge cases. Reducing the diaphragm distance from the corner would quicken the development and growth of the separation bubble. At lower d values the oblique shock was also noted to develop earlier. Increasing the value of P41 would result in a more elliptic bubble shape. The oblique shock was seen to develop towards to rear end of the bubble at high P41.
- The bubble tended to be notably larger for the smaller corner angles than with the 90° case.
- A significant difference was noted in the profile of the bubble where for smaller angles a much rounder profile was noted and steeper inclinations would result in a more oblong bubble shape. This would be attributed to the inclination angle of the flow along the vertical wall.
- Increased acceleration of the flow around the bubble induced by the bubble's curvature resulted in the oblique shock developing at an earlier stage in the wedge cases than with the 90° corner.
- The recompression shock which was found only at $P41 = 3$ and $d = 10$ mm for $\theta = 90^\circ$ had developed for larger values of d (40 mm and 70 mm) in the wedge cases. This could be a result of the increased flow acceleration in the bubble at the smaller angles.

Results from the LES analysis

- A good correlation between the LES solution, the RANS solution and the experimental results was found. The mean velocity distribution through the bubble from the LES results agreed well with the RANS solution.
- The primary motivation behind the use of LES for this study was to resolve the turbulent vortical structures within the separation bubble that were identified experimentally. In the LES solution the structure of the bubble was seen to be highly turbulent as observed experimentally.
- Shear layer instability and vortex shedding was observed to occur at higher P41 values from the experimental investigation. This was observed for $P41 = 7.7$ at later times in the LES solution.
- The profile of the separation bubble and the shear layer was shown to be not as smooth as detected by the RANS solver. The shear layer was observed to become unstable and break at several locations along the profile of the bubble.
- The wake region was largely unresolved. The mesh resolution required to resolve the wake is extremely small and was considered infeasible for the current study.
- The structure within the bubble showed a notable variation through the depth. The primary vortex at higher pressure ratios could not be identified clearly from a 2D plot. However, the circulatory flow within the bubble was identified from 3D streamtraces.
- In 3D model allowed the the oblique shock profile to be analysed at different depths. It was observed that the profile was not consistent through the depth. The curvature of the shock was higher at the centre of the model than at the walls.
- Shocklets around the periphery of the bubble that were identified in the experimental analysis was resolved by the LES code. The shocklets are believed to be turbulence induced and not a result of rig-dependant effects as concluded previously.

Chapter 9 Recommendations

Recommendations for further experimental work

- In this work the diffraction corner angles tested were $< 45^\circ$. A further analysis could consider wedge angles ranging between 90° and 45° .
- The distance of the diffraction corner from the diaphragm could be increased so the wake region is not obscured by the aluminium diaphragm used.

Recommendations for further computational work

- As with the experimental work a larger number of wedge angles could be tested.
- With a increased computational resources, the LES model could be refined further to attempt to resolve the wake region.
- Much work is needed in the area of LES subgrid scale models for compressible turbulent flow.

References

- [1] I. Mahomed and B. W. Skews. ‘Expansion wave diffraction over a 90 degree corner’. In: *Journal of Fluid Mechanics* 757 (2014), pp. 649–664. ISSN: 1469-7645. DOI: [10.1017/jfm.2014.491](https://doi.org/10.1017/jfm.2014.491).
- [2] B. W. Skews. ‘The perturbed region behind a diffracting shock wave’. In: *Journal of Fluid Mechanics* 29 (04 1967), pp. 705–719. ISSN: 1469-7645. DOI: [10.1017/S0022112067001132](https://doi.org/10.1017/S0022112067001132).
- [3] L. N. Howard and D. L. Matthews. ‘On the Vortices Produced in Shock Diffraction’. In: *Journal of Applied Physics* 27.3 (1956), pp. 223–231. DOI: <http://dx.doi.org/10.1063/1.1722349>.
- [4] I. Mahomed. ‘Two-dimensional expansion wave diffraction around a 90 degree convex corner’. MA thesis. School of mechanical, industrial and aeronautical engineering, University of the Witwatersrand, 2013.
- [5] D. K. Walters et al. ‘Investigation of a Dynamic Hybrid RANS/LES Modelling Methodology for Finite-Volume CFD Simulations’. In: *Flow, Turbulence and Combustion* 91.3 (2013), pp. 643–667. ISSN: 1573-1987. DOI: [10.1007/s10494-013-9481-9](https://doi.org/10.1007/s10494-013-9481-9).
- [6] O. Petrache, S. Hickel and N. Adams. ‘Large eddy simulations of turbulent enhancement due to forced shock motion in shock-boundary layer interaction’. In: *AIAA paper* 2216 (2011).
- [7] P. R. Spalart. ‘Strategies for turbulence modelling and simulations’. In: *International Journal of Heat and Fluid Flow* 21.3 (2000), pp. 252–263.
- [8] E. Garnier, N. Adams and P. Sagaut. *Large Eddy Simulation for Compressible Flows*. Springer Science & Business Media, 2009.
- [9] *ANSYS, Release 16.2, Help System. Fluent Theory Guide*. Version 16.2. ANSYS, Inc.
- [10] J. H. Ferziger and M. Peric. *Computational Methods for Fluid Dynamics*. 3rd ed. Springer Science & Business Media, 2002.

Appendix A Engineering Drawings

Engineering drawings are provided for the main components of the driver section of the shock tube and parts of the driven section that were replaced are provided. These are followed by detailed drawings of wedge test pieces. The following images include:

- Figure A.9 - The Driver Back Plate
- Figure A.2 - The Driver Bottom Plate
- Figure A.3 - The Driver Top Plate
- Figure A.4 - The Driver Side Plate (Right)
- Figure A.5 - The Driver Window Frame
- Figure A.6 - The Driver Window
- Figure A.7 - Driver assembly drawing
- Figure A.8 - Driver exploded assembly
- Figure A.9 - Driven Back Plate
- Figure A.10 - Full shock tube assembly drawing
- Figure A.11 - Test Piece: 15° , $d = 35$ mm
- Figure A.12 - Test Piece: 15° , $d = 55$ mm
- Figure A.13 - Test Piece: 45° , $d = 35$ mm
- Figure A.14 - Test Piece: 45° , $d = 55$ mm

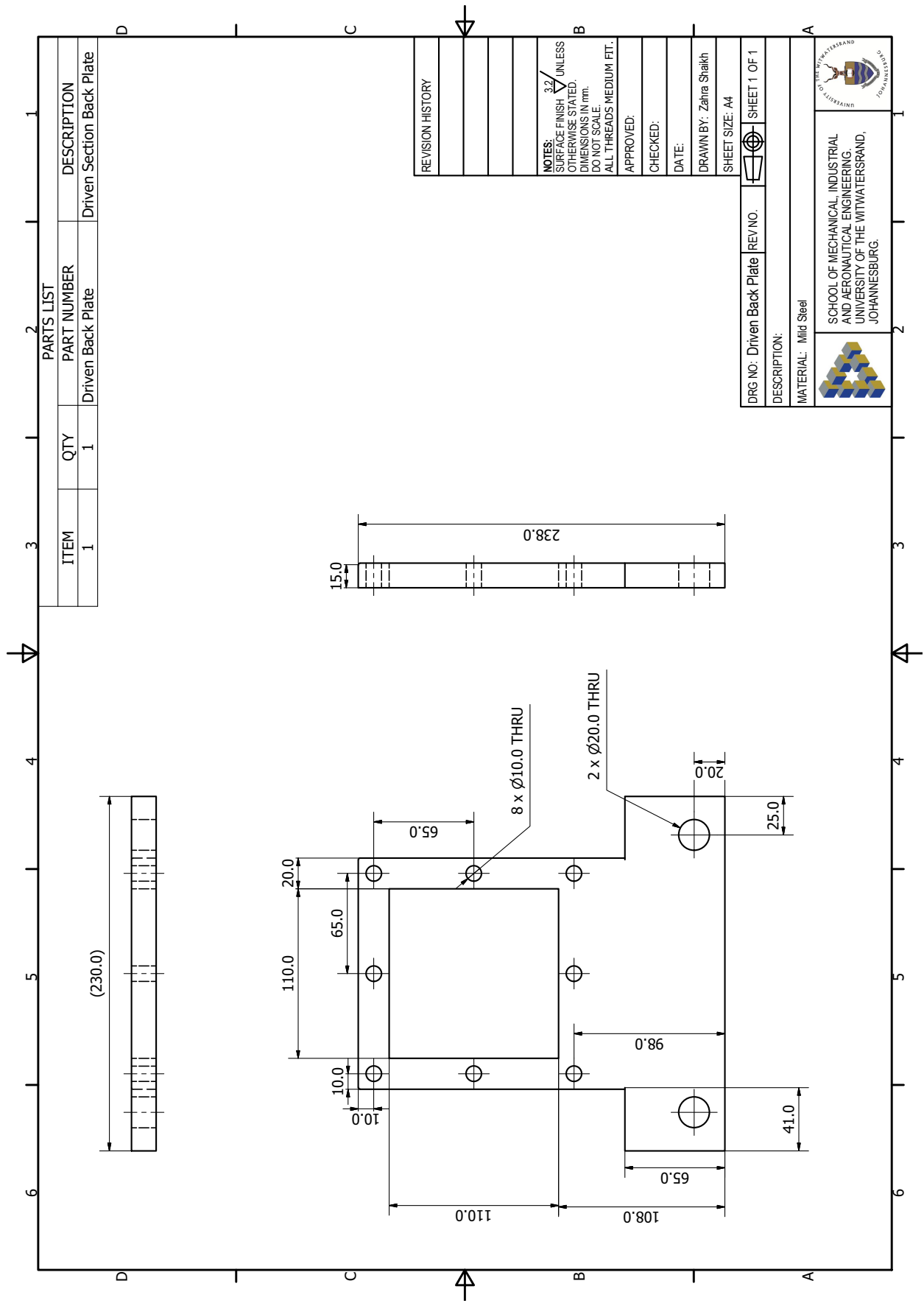


Figure A.1: Driver Back Plate

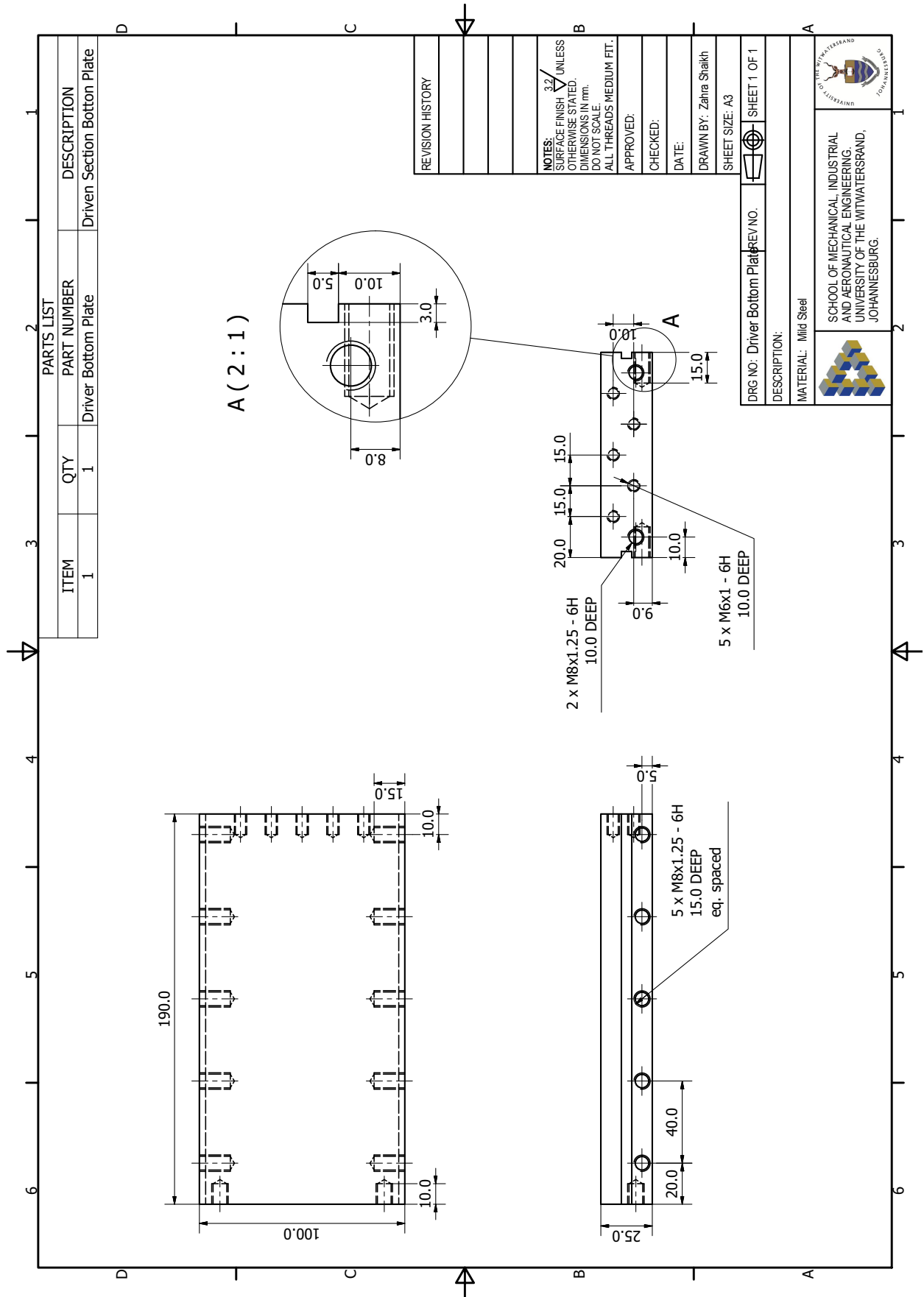


Figure A.2: Driver Bottom Plate

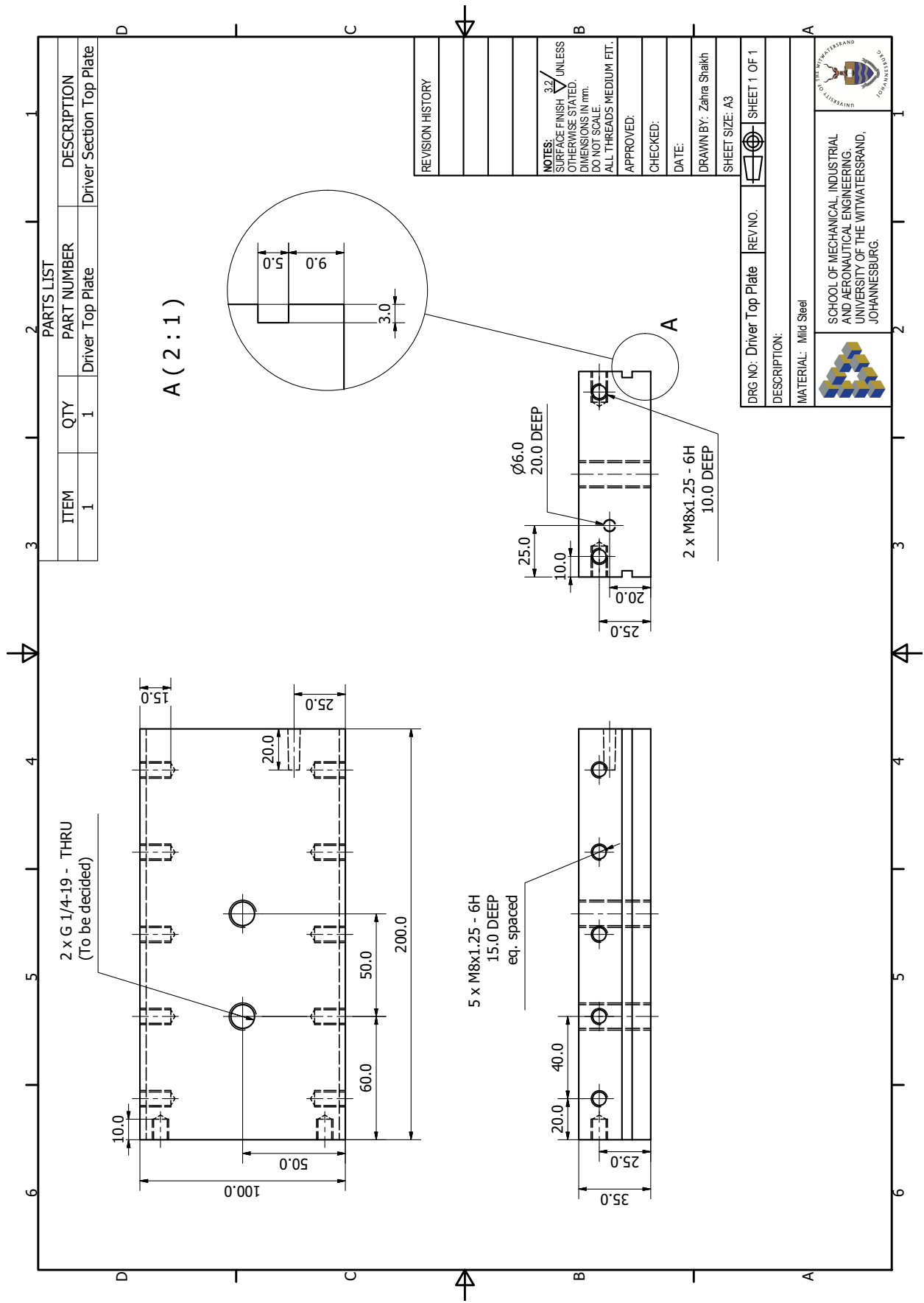


Figure A.3: Driver Top Plate

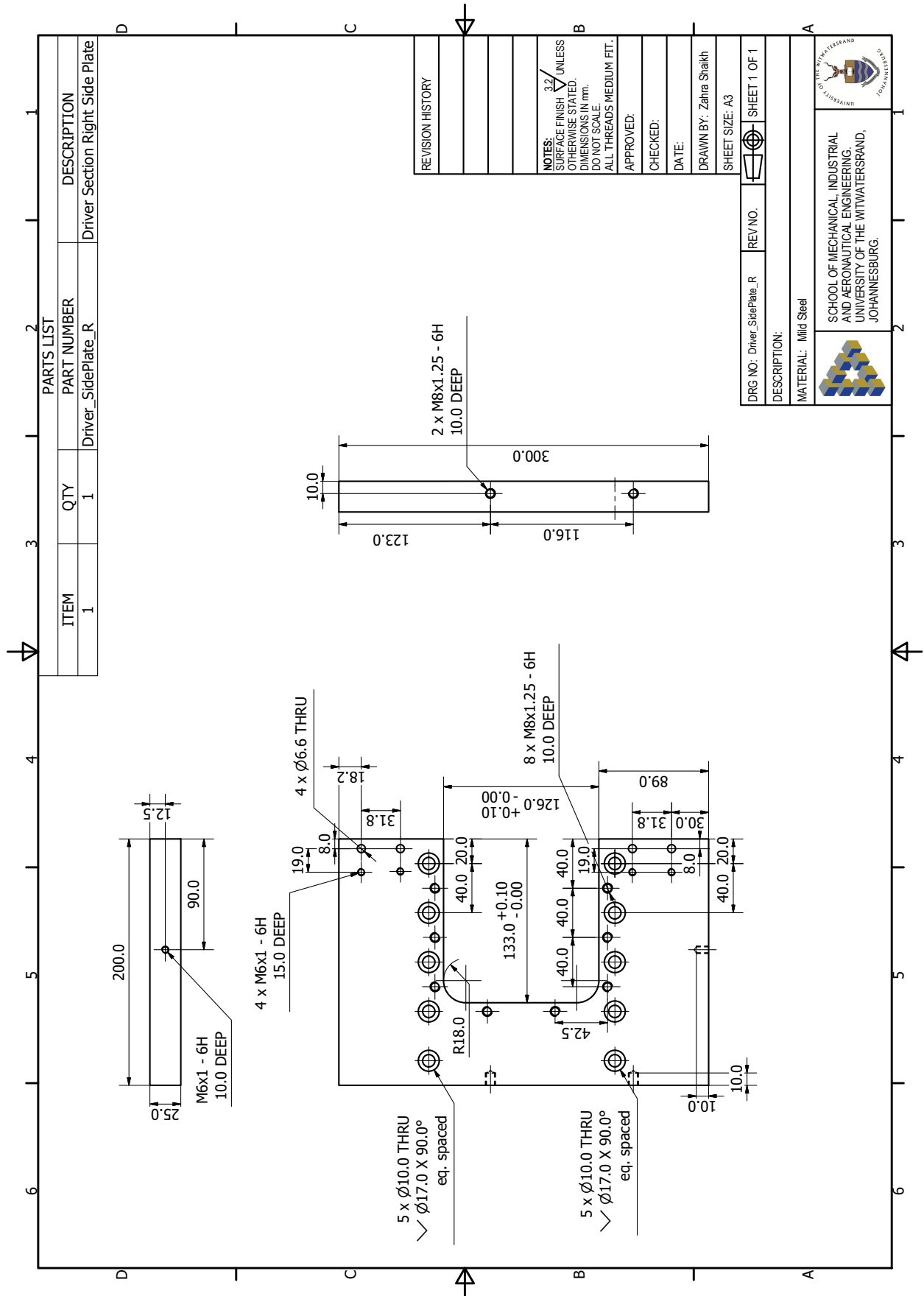


Figure A.4: Driver Side Plate (Right). Identical dimensions for left side

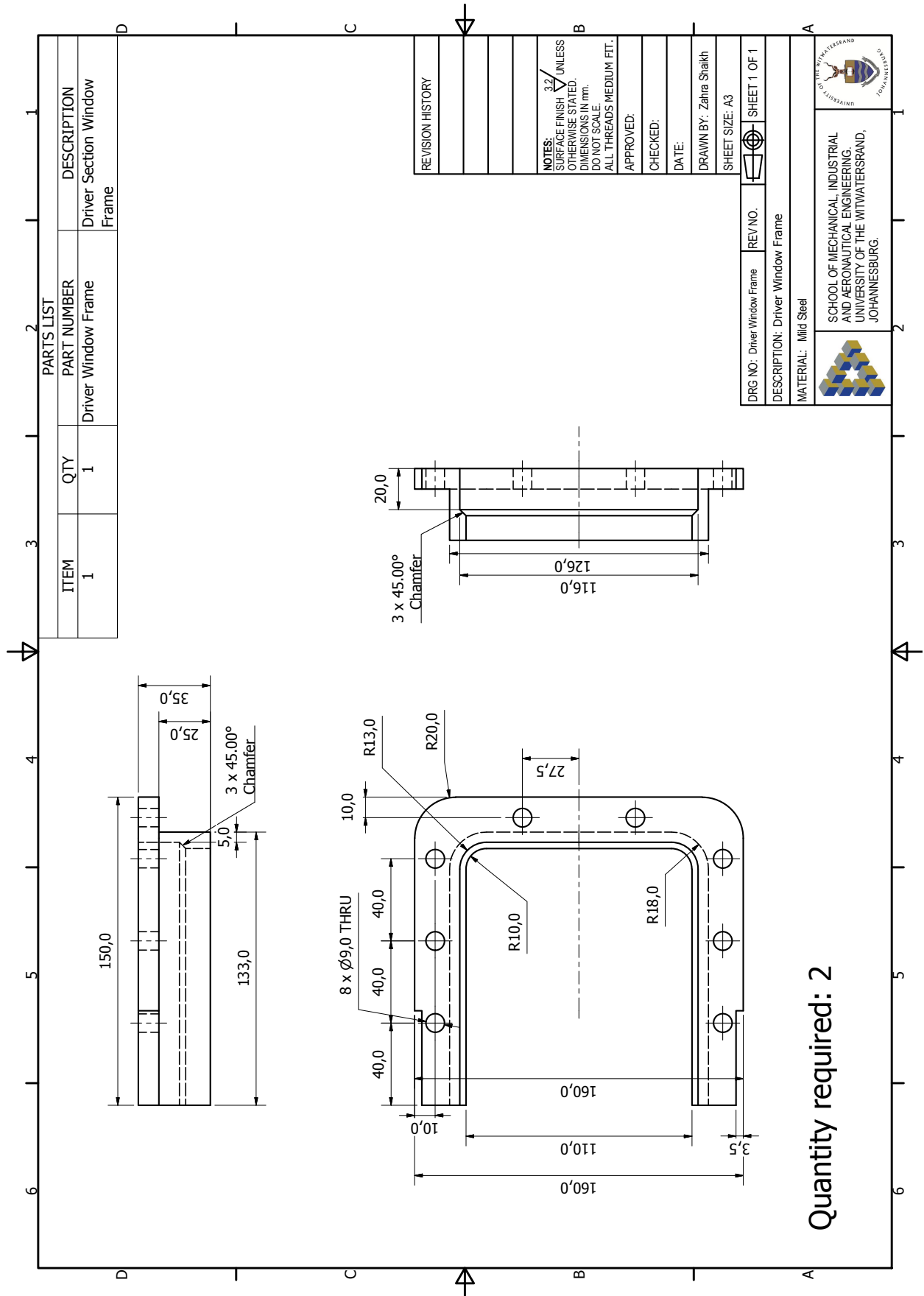


Figure A.5: Driver Window Frame

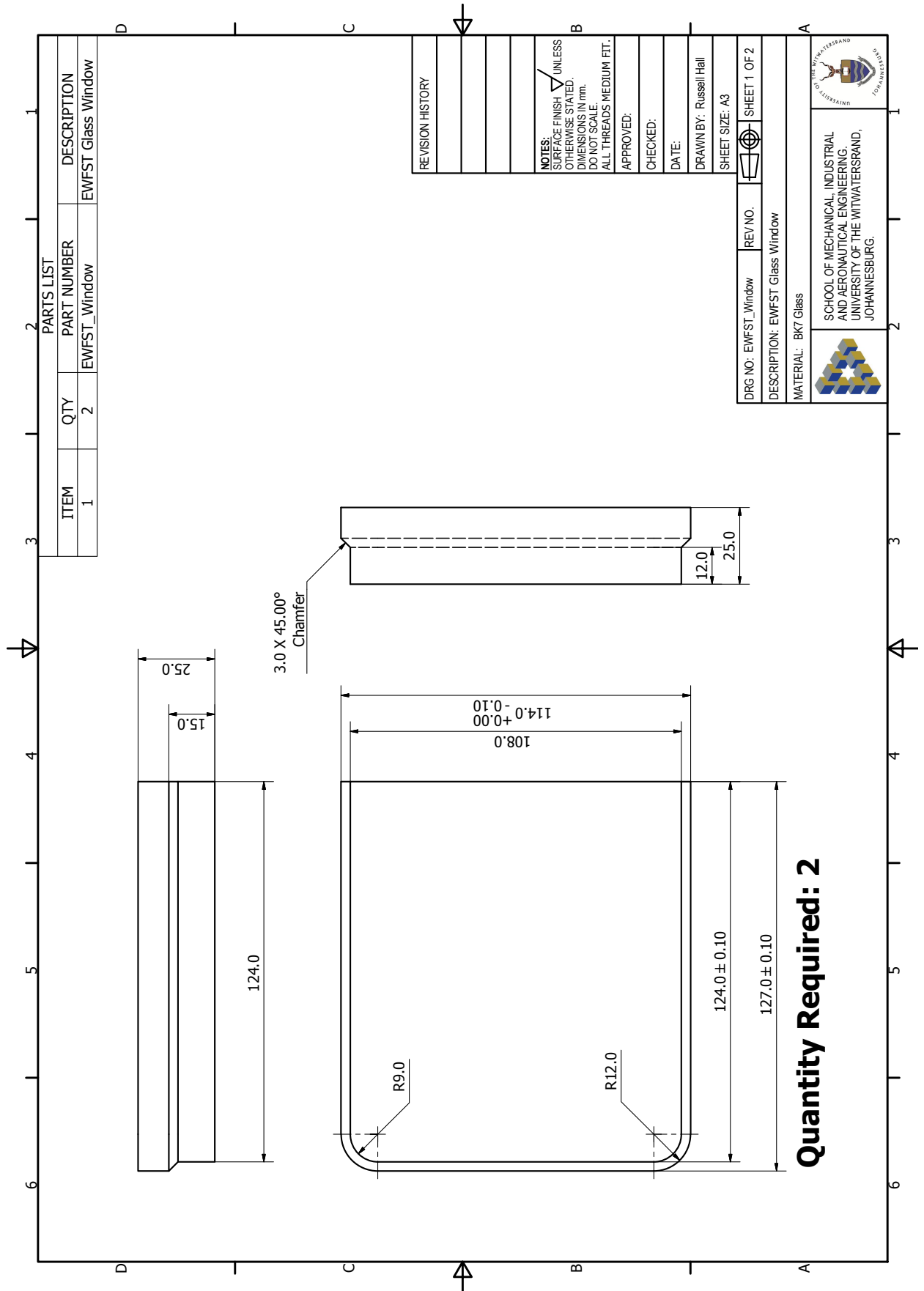


Figure A.6: Driver Window

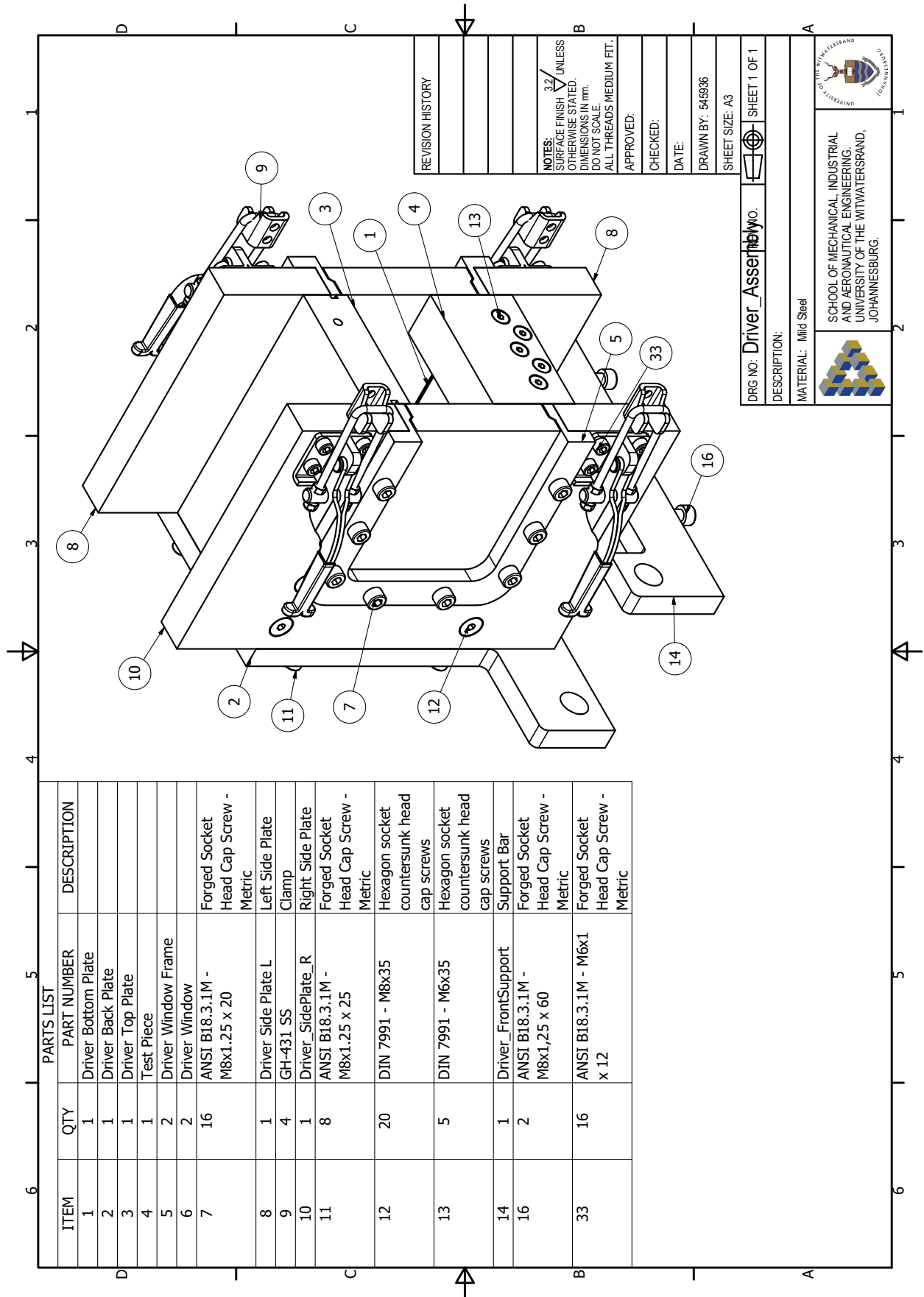


Figure A.7: Driver Section Assembly

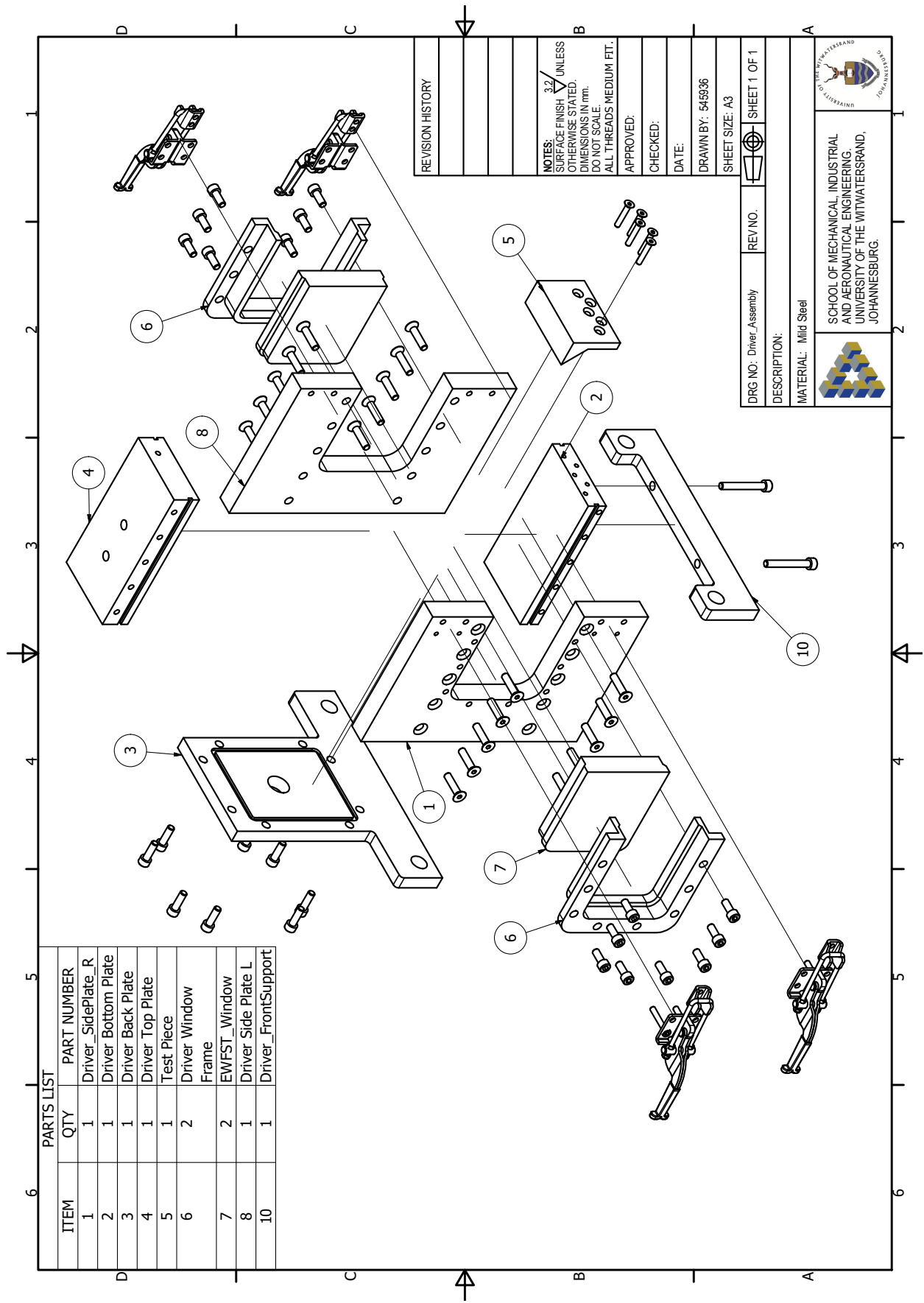


Figure A.8: Driver Section Exploded Assembly

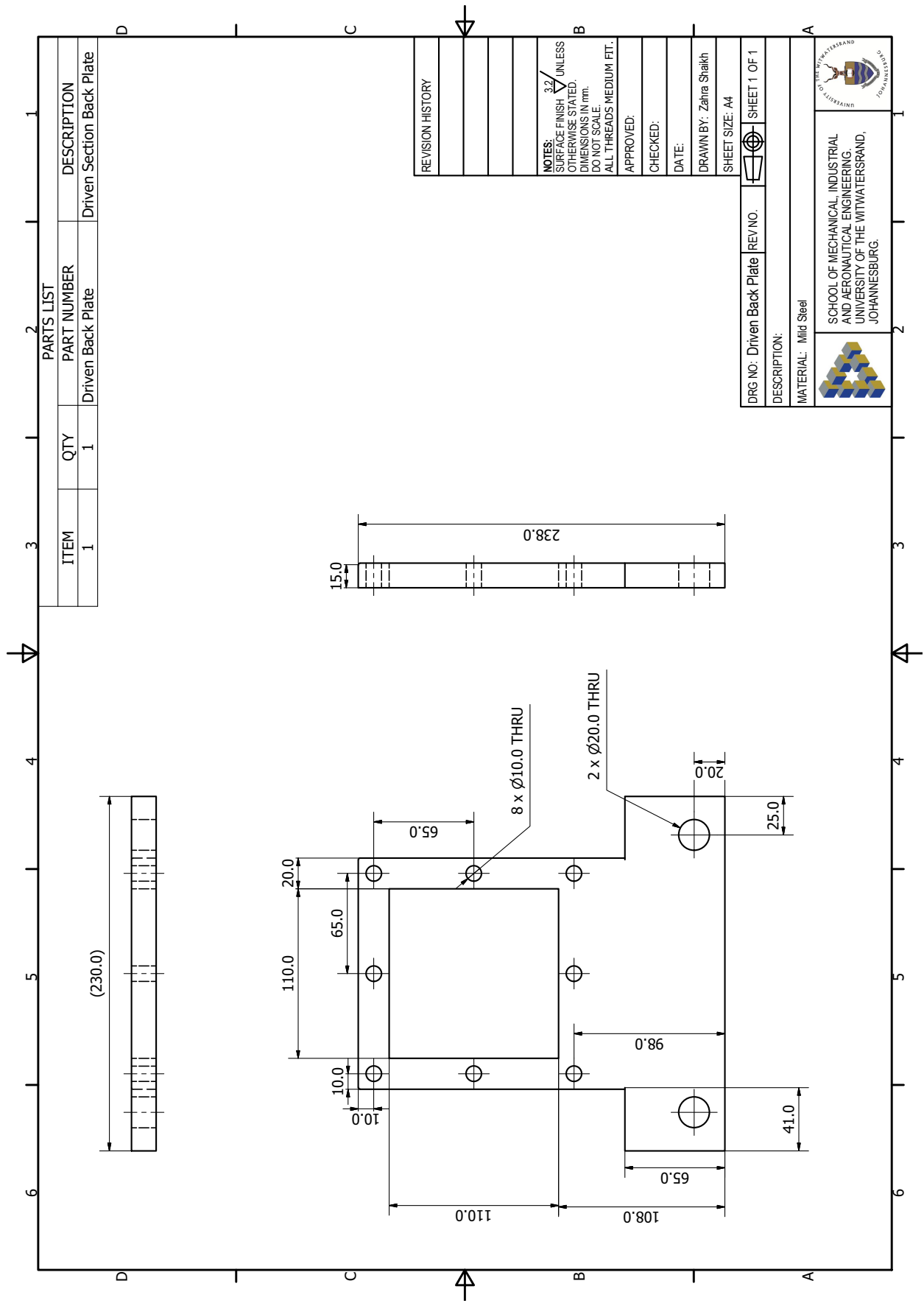
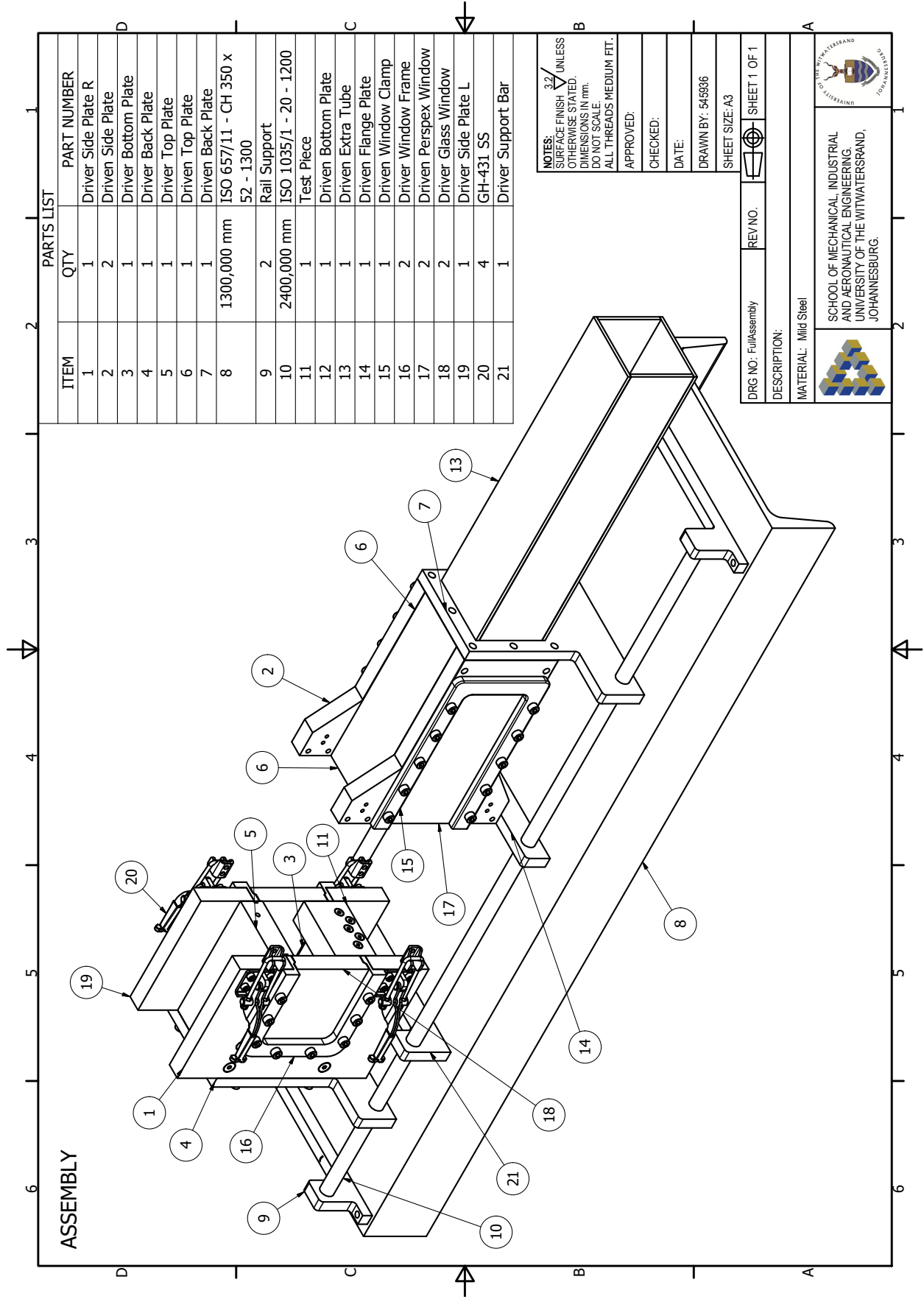


Figure A.9: Driven Back Plate



PARTS LIST		
ITEM	QTY	PART NUMBER
1	1	Driver Side Plate R
2	2	Driven Side Plate
3	1	Driver Bottom Plate
4	1	Driver Back Plate
5	1	Driver Top Plate
6	1	Driven Top Plate
7	1	Driven Back Plate
8	1300,000 mm	ISO 657/11 - CH 350 x 52 - 1300
9	2	Rail Support
10	2400,000 mm	ISO 1035/1 - 20 - 1200
11	1	Test Piece
12	1	Driven Bottom Plate
13	1	Driven Extra Tube
14	1	Driven Flange Plate
15	1	Driven Window Clamp
16	2	Driver Window Frame
17	2	Driven Perspex Window
18	2	Driver Glass Window
19	1	Driver Side Plate L
20	4	GH-431 SS
21	1	Driver Support Bar

NOTES:
 SURFACE FINISH $\frac{3.2}{\sqrt{R}}$ UNLESS OTHERWISE STATED.
 DIMENSIONS IN mm.
 DO NOT SCALE.
 ALL THREADS MEDIUM FIT.

APPROVED:
 CHECKED:
 DATE:
 DRAWN BY: 545936
 SHEET SIZE: A3

DRG NO: FullAssembly REV. NO. SHEET 1 OF 1

DESCRIPTION:

MATERIAL: Mild Steel

SCHOOL OF MECHANICAL INDUSTRIAL AND AERONAUTICAL ENGINEERING
 UNIVERSITY OF THE WITWATERSRAND,
 JOHANNESBURG.

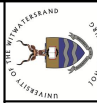


Figure A.10: Shock Tube Assembly

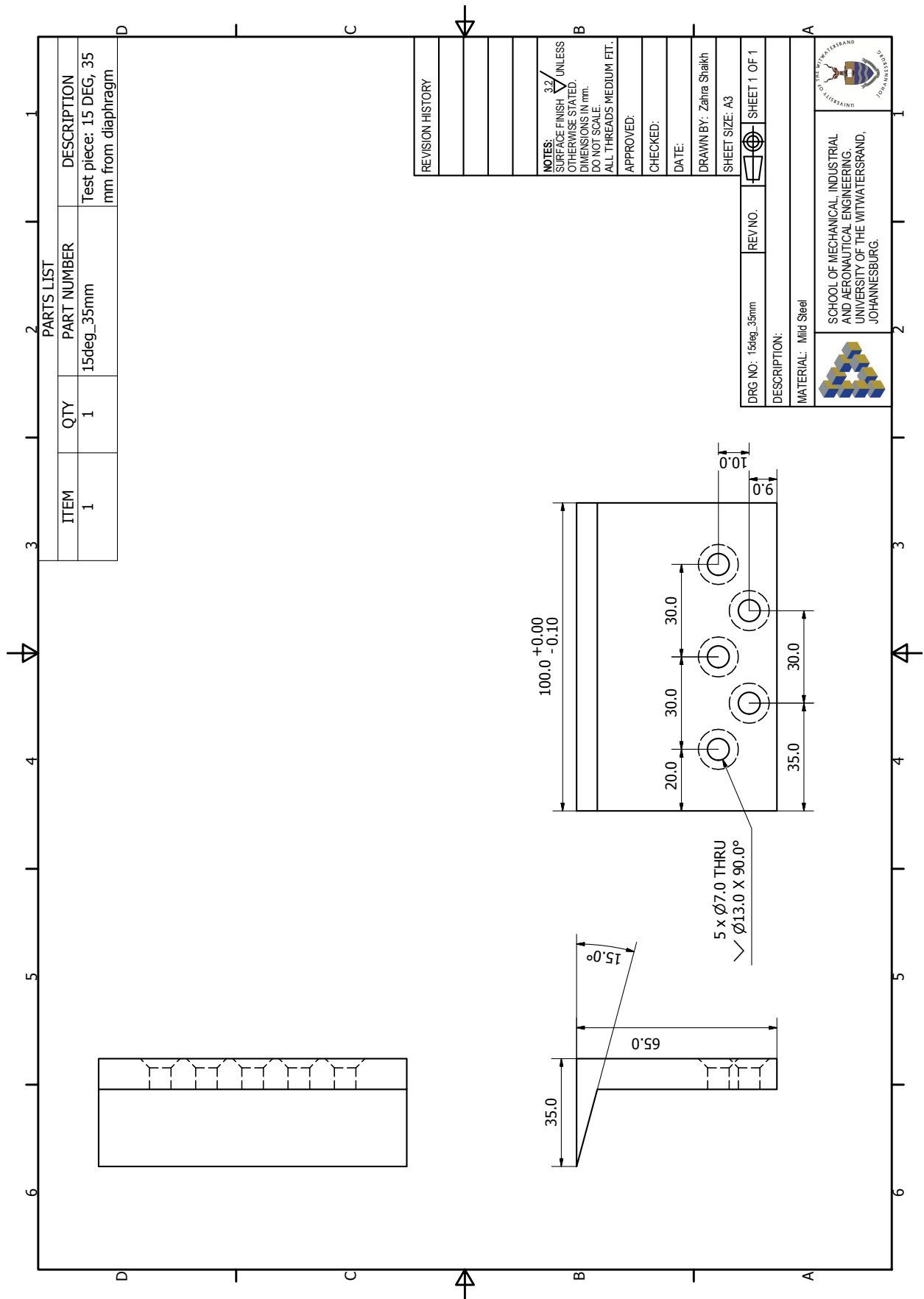


Figure A.11: Test Piece: 15°, $d = 35$ mm

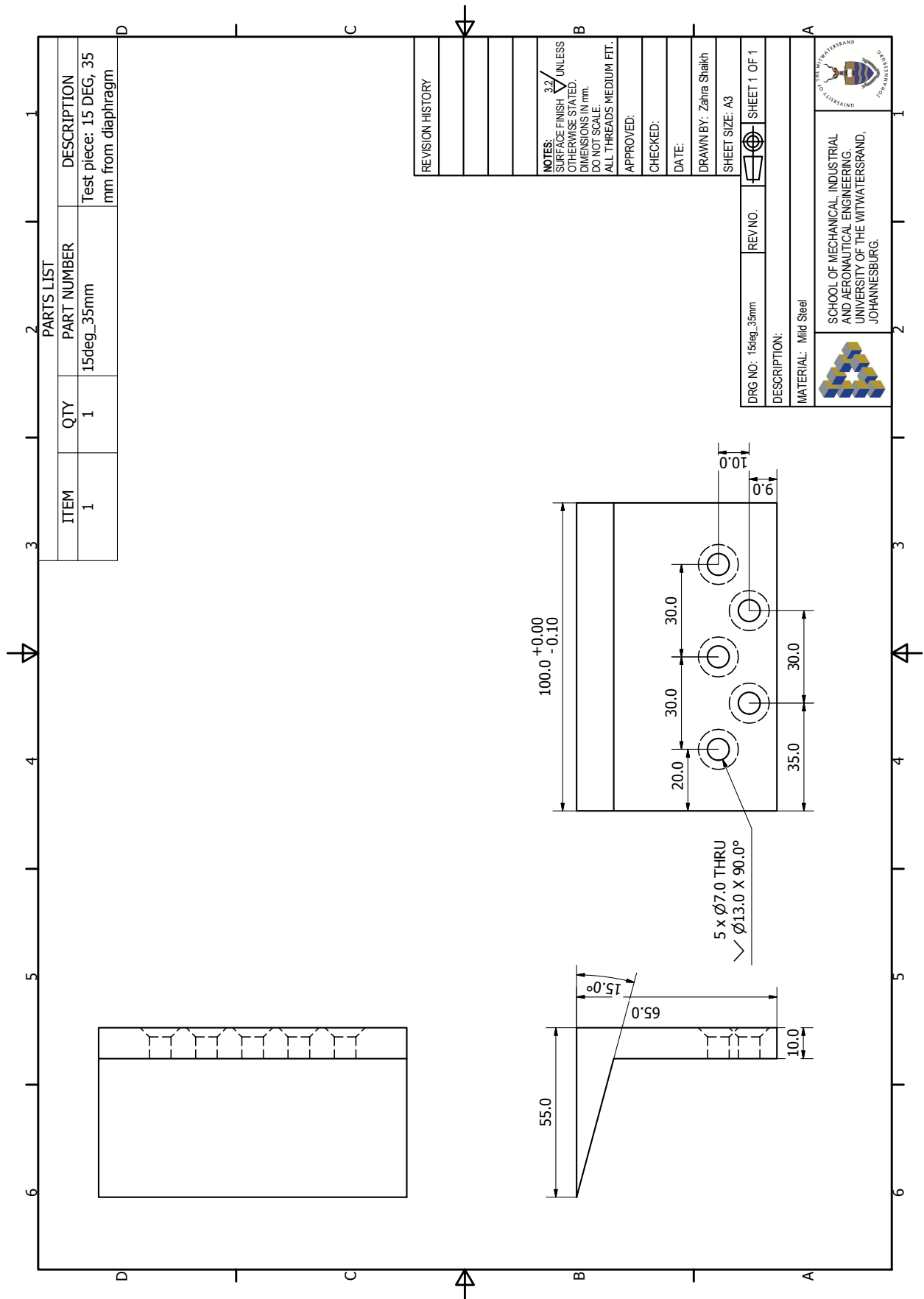


Figure A.12: Test Piece: 15°, $d = 55$ mm

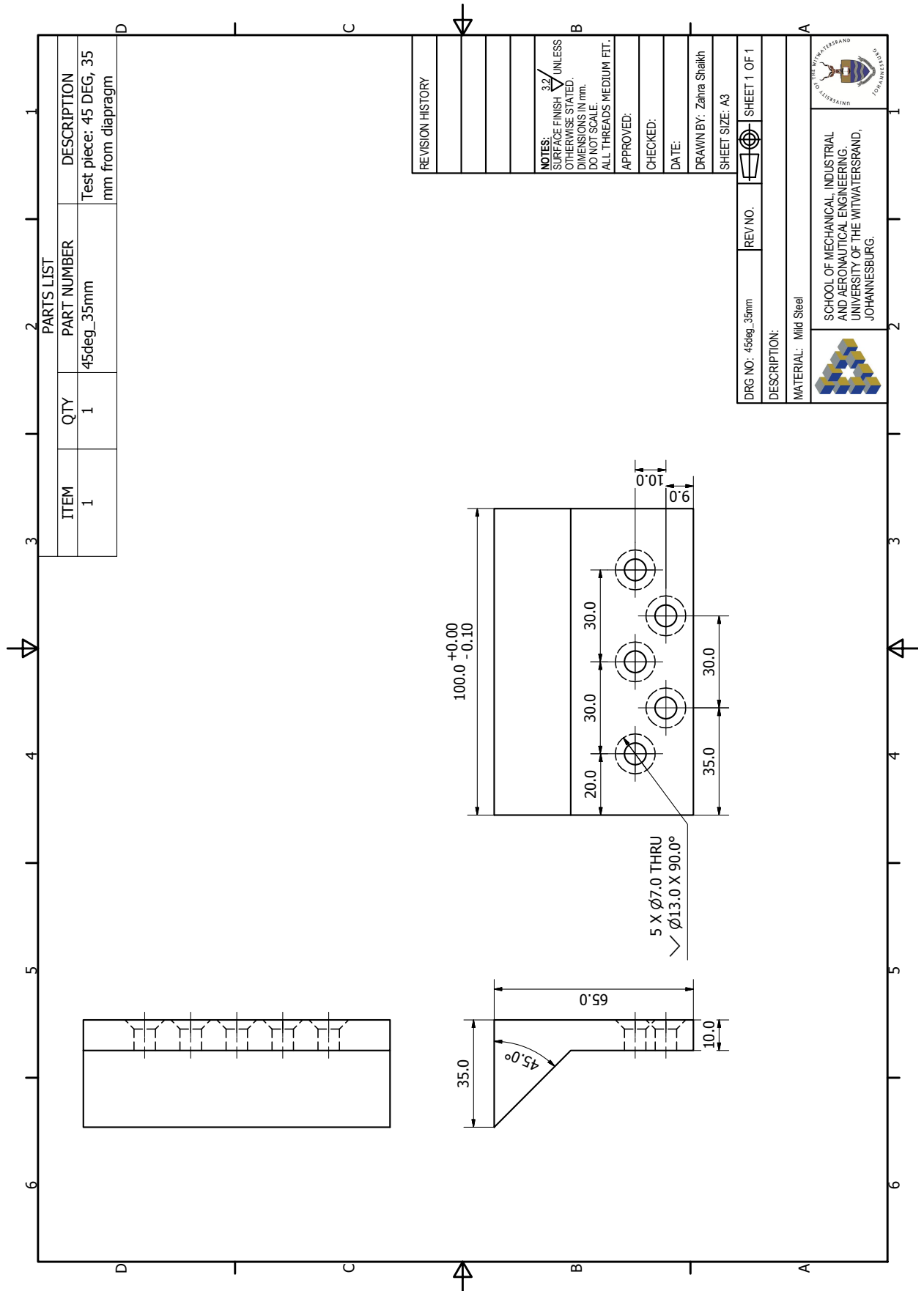


Figure A.13: Test Piece: 45°, d = 35 mm

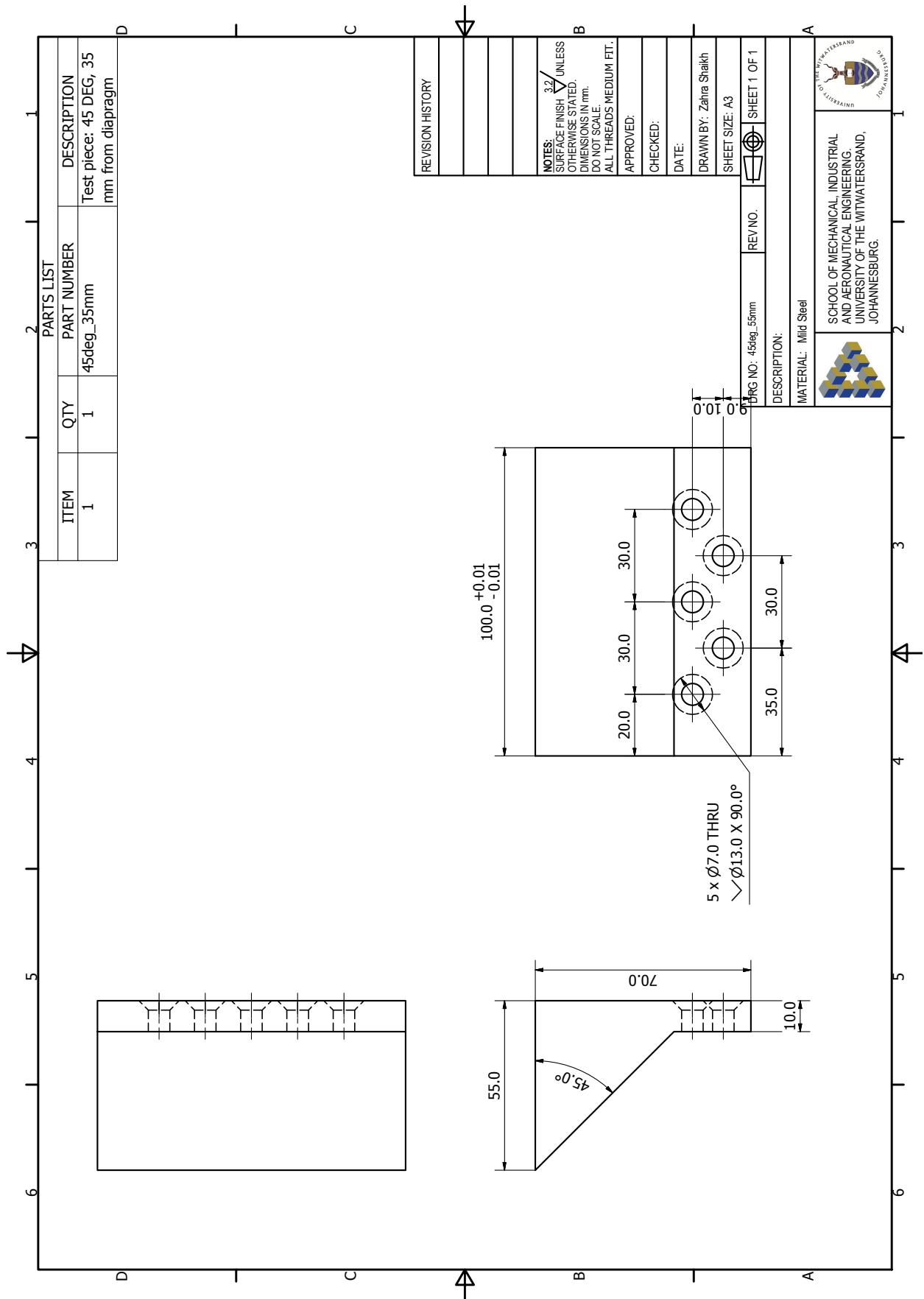
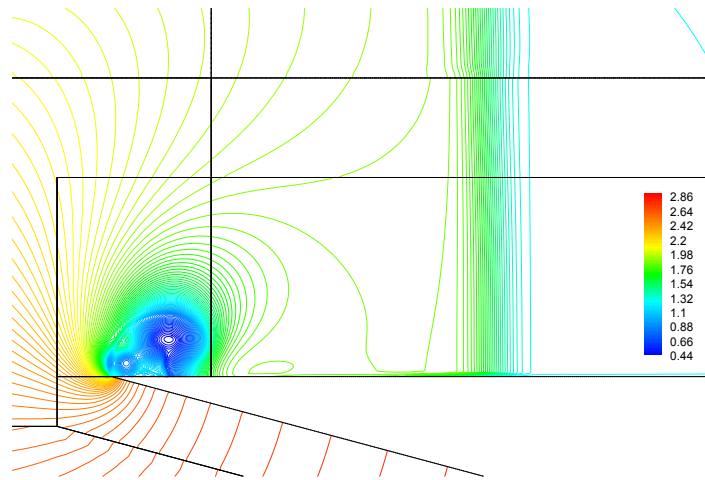


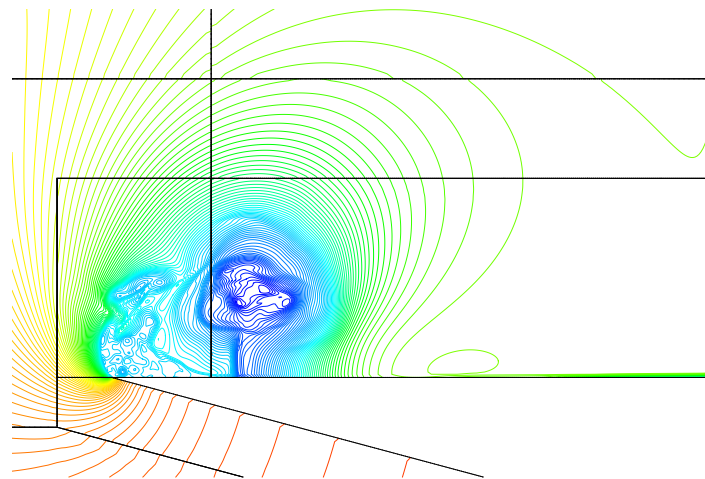
Figure A.14: Test Piece: 45° , $d = 55$ mm

Appendix B Additional ELES Results for 15° , $d = 10$ mm

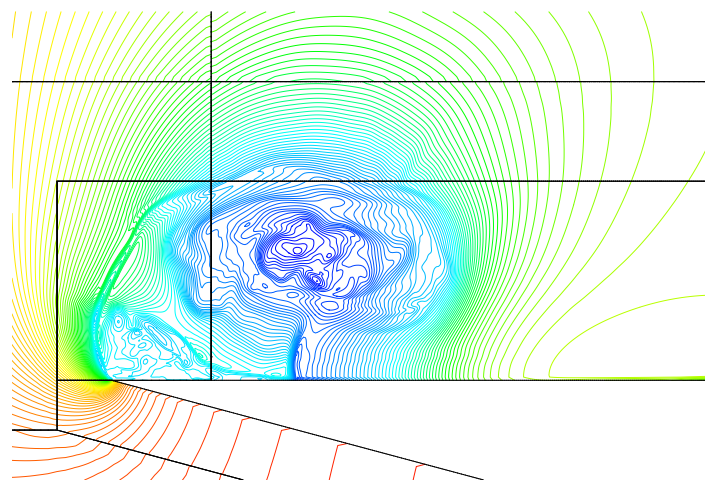
Contour plots of density and vector plots of velocity magnitude for the $z = 5$ mm and $z = 15$ mm from the LES solution for 15° wedge are provided in the following pages.



(a) $t = 200 \mu s$

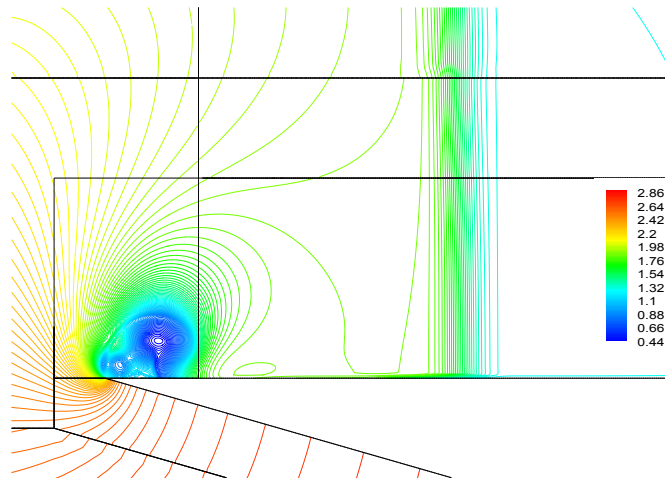


(b) $t = 400 \mu s$

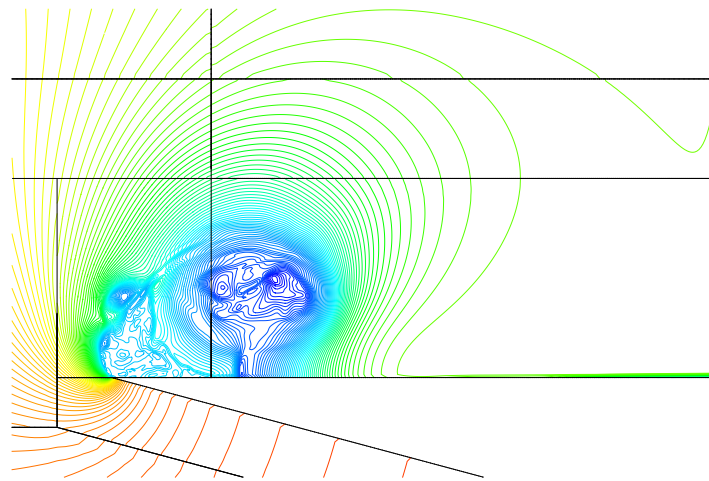


(c) $t = 600 \mu s$

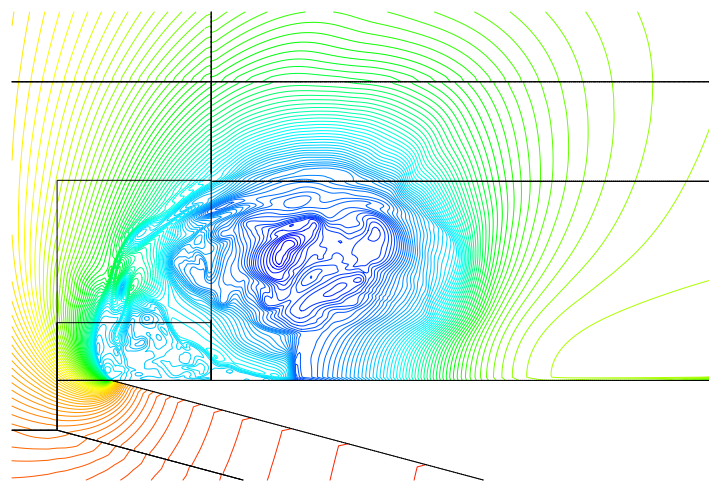
Figure B.1: LES Density contour plots for $\theta = 15^\circ$, $P41 = 3$ at $z = 5 \text{ mm}$



(a) $t = 200 \mu s$

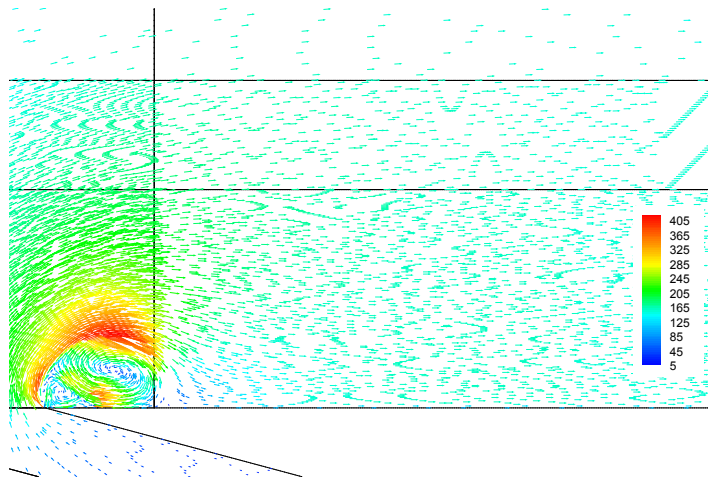


(b) $t = 400 \mu s$

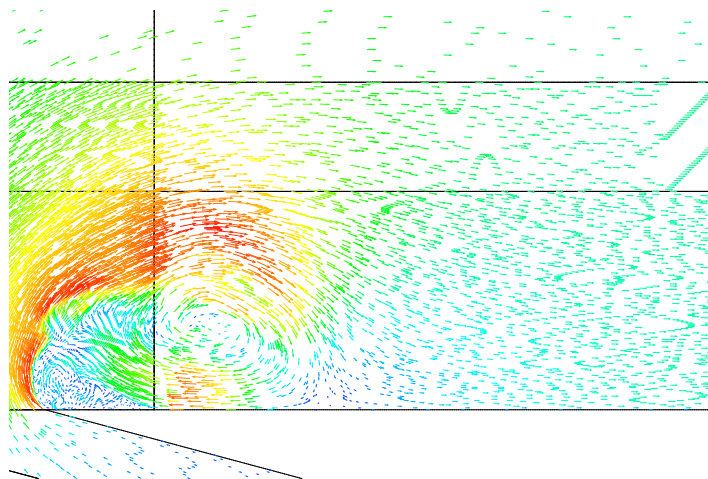


(c) $t = 600 \mu s$

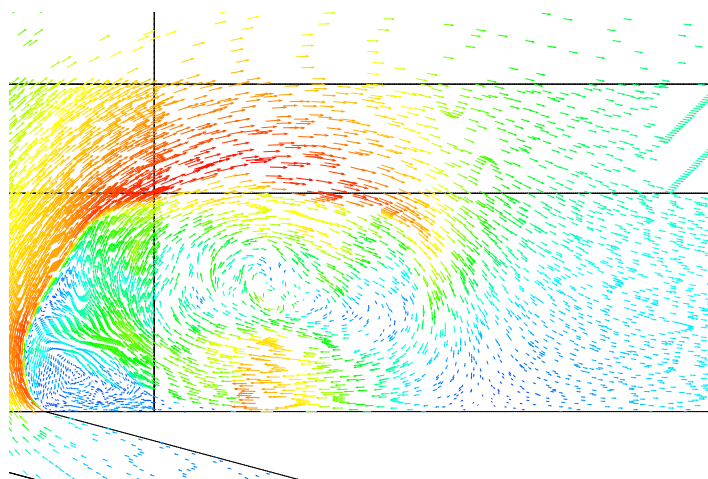
Figure B.2: LES Density contour plots for $\theta = 15^\circ$, $P41 = 3$ at $z = 15$



(a) $t = 200 \mu s$

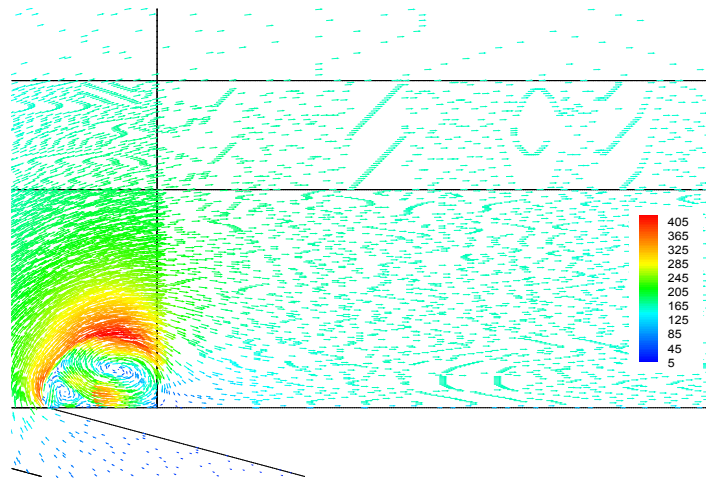


(b) $t = 400 \mu s$

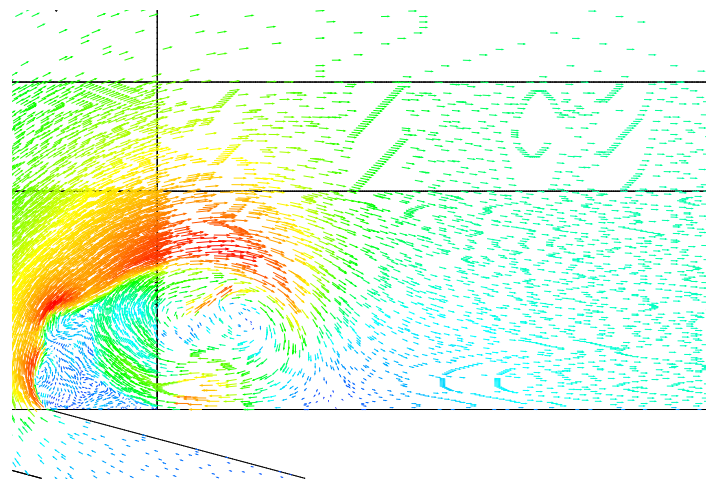


(c) $t = 600 \mu s$

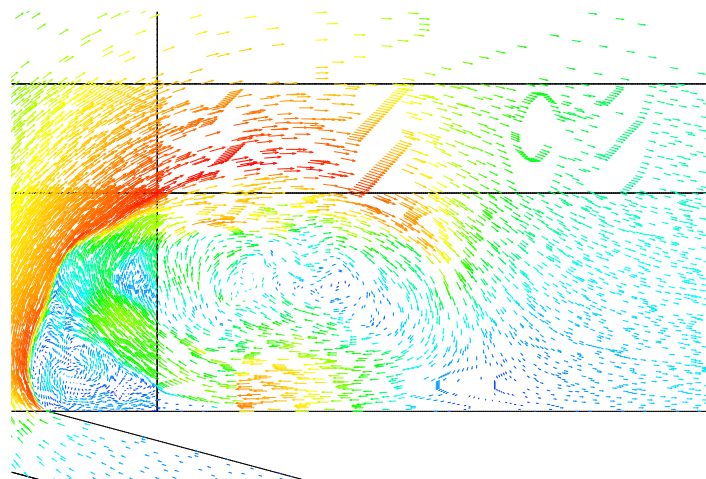
Figure B.3: LES Velocity vector plots for $\theta = 15^\circ$, $P41 = 3$ at $z = 5$



(a) $t = 200 \mu s$



(b) $t = 400 \mu s$



(c) $t = 600 \mu s$

Figure B.4: LES Velocity vector plots for $\theta = 15^\circ$, $P41 = 3$ at $z = 15$

Appendix C Digital Appendix

An attached CD was provided with the following contents:

C.1

- Experimental schlieren videos

C.2

- Engineering drawings for the shock tube